NUMERICAL AND EXPERIMENTAL INVESTIGATION OF A MULTI-PASS HEAT-PIPE-BASED HEAT EXCHANGER

A thesis submitted for the degree of Doctor of Philosophy

By

HASSAN MROUE

Department of Mechanical, Aerospace and Civil Engineering (MACE)

College of Engineering, Design and Physical Sciences

Brunel University London,
Uxbridge, UB8 3PH, UK

2018

Abstract

Theoretical, numerical and experimental investigations have been successfully carried out to characterise the thermal performance of an air-to-water multi-pass heat exchanger equipped with thermosyphon technology. Air and water are the heat source and the heat sink on the evaporator and condenser, respectively. Evaporator and condenser are connected by six thermosyphons, through which thermal energy is transferred.

The investigation was performed for two multi-pass configurations at various inlet conditions: a range of air inlet temperatures (100, 150, 200 and 250°C) and mass flow rates (0.05, 0.08, 0.11 and 0.14 kg/s). The water inlet conditions were kept constant (a temperature of 15°C and a mass flow rate of 0.08 kg/s)

The theoretical model was built by applying the thermal resistance analogy with the aid of convection, boiling and condensation correlations found in the literature. It was found that the thermal resistances in the first pass act in parallel mode along the ones in the second pass. Similarly, in the case of three passes. Also, the external convective thermal resistance were found to be the major contributor to the overall thermal resistance in the entire heat exchanger.

ANSYS Fluent was the numerical tool used to investigate the shell-side convective heat transfer for two multi-pass configurations. The CFD model has been experimentally validated. The two-phase change processes inside the thermosyphons were not modelled during the simulation. Instead, the thermosyphons were treated as solid rods with a constant thermal conductivity, which was calculated. The overall rate of heat transfer was obtained by both CFD and a theoretical model, and the results lay within 15% of the experimental data. The numerical predictions demonstrated that the $K-\varepsilon$ Realizable turbulence model with scalable wall function is a reliable tool for predicting heat transfer and fluid flow in such types of heat exchangers.

This investigation will add a great knowledge to the academia in terms of both experimentation and modelling in the area of multi-pass thermosyphons-based heat exchangers. Also, it provides the industries with a cost effect design tool for future modelling of similar heat exchanger systems.

Acknowledgments

In this section, I want to acknowledge various people that provided me with different kind of support throughout my PhD journey here at Brunel and at Econotherm (UK) Ltd.

Firstly, I want to thank my parents who supported my decision as a first step to pursue a PhD degree. My dad, without him I wouldn't be able to finance this degree and nothing can describe my mom's unconditional love.

Secondly, I would like to express my special thanks to my second supervisor, Prof. Luiz Wrobel, who gave me the chance to meet my principal supervisor Dr. Hussam Jouhara, who offered me the golden opportunity to work on this great project. Their invaluable support and constantly wise advice have made me learn so much of their professional expertise which I'm always thankful for. I want to also thank their patience and encouragement while pushing me farther than I thought I could go.

To the Econotherm (UK) Ltd. staff, I want to thank CEO Mark Boocock for allowing me to carry out the experimental work of the multi-pass in his company in Bridgend, Wales. Also, allowing the staff and technicians to help me building the experimental rig as it was time and cost consuming. Staff and technicians include Peter Blackwell, Viorel and Stefan Munteanu, Toth Tibor (R.I.P.), Michael Jones and finally Quentin Vercoutre, who was a placement student but a great help when conducting the single thermosyphon tests with various working fluids. A special thanks goes to Dr. Joao Ramos for his extensive support during my stay at Econotherm (UK) Ltd. as he provided me with all the necessary training during the experimental validation.

Finally, to the CSEF team at Brunel University. I want to express my gratitude to Prof. Savvas Tassou, Dr. Walid Youssef, Theodora Nannou, Bertrand Delpech, Dr. Kostantinos Tsamos, Maureen Senatore and recently Matteo Marchionni and Ioannis Katsaros, meeting such great people have contributed morally throughout my stay in the centre. Finally, I want to thank Guillaume Menart for his help while conducting the single thermosyphon test in the CSEF lab.

List of Publications

Journal papers:

Title: Experimental and numerical investigation of an air-to-water heat pipe-based heat exchanger

Authors: H. Mroue, J.B. Ramos, L.C. Wrobel, H. Jouhara

Journal: Applied Thermal Engineering, Vol. 78, 339-350, 2015

Status: Published

Title: Performance evaluation of a multi-pass air-to-water thermosyphon-based heat exchanger

Authors: H. Mroue, J.B. Ramos, L.C. Wrobel, H. Jouhara

Journal: Energy, Vol. 139, 1243-1260, 2017

Status: Published

Conference papers:

Title: Experimental investigation of a multi-pass heat-pipe based heat exchanger

Authors: H. Mroue, L.C. Wrobel, H. Jouhara

Conference: Sustainable Energy & Environmental Protection (SEEP)

Year: 2014

Location: Dubai, United Arab Emirates

Title: Numerical investigation of the convective heat transfer in a helical finned condenser

Authors: H. Mroue, T. Garczarczyk, L.C. Wrobel, H. Jouhara

Conference: Sustainable Energy & Environmental Protection (SEEP)

Year: 2015

Location: Glasgow, Scotland, United Kingdom

Table of Content

List of Figures

List of Tables

Nomenclature

Acronyms

BPHX	Brazed-Plate Heat Exchanger
CFD	Computational Fluid Dynamics
CHT	Computational Heat transfer
DD-HX	Disk and Doughnut baffles Heat Exchanger
DNS	Direct Numerical Simulations
EU	European Union
FB-STHX	Flower Baffles Shell-and-Tube Heat Exchanger
FPHX	Frame-and-Plate Heat Exchanger
GHG	Greenhouse Gas
NFB	Nucleate Film Boiling
NFC	Nucleate Film Condensation
NHT	Numerical Heat Transfer
NPB	Nucleate Pool Boiling
NTU	Number of Transfer Units
HP	Heat pipe
HPHX	Heat Pipe based Heat Exchanger
HTC	Heat Transfer Coefficient
HVAC	Heating, Ventilation and Air Conditioning
HX	Heat Exchanger
$K-\varepsilon$	K-epsilon Turbulence Model
LES	Large Eddy Simulation
PHX	Plate Heat Exchanger
RANS	Reynolds Averaged Navier-Stokes
STHX	Shell-and-Tube Heat Exchanger
SG-STHX	Segmental baffles Shell-and-Tube Heat Exchanger
TFU	Through-Flow Unit
TPCT	Two-Phase Closed Thermosyphon
TPHX	Thermosyphon based Heat Exchanger
TS	Thermosyphon
UDF	User Defined Function

1TS	Single Thermosyphon
6TSs	Six Thermosyphons

Symbols

A	Heat transfer area	$\mathrm{m^2}$
A_c	Thermosyphon condenser heat transfer surface area	$\mathrm{m^2}$
c_p	Specific heat at constant pressure	$\mathrm{J/kg.K}$
C_{sf}	Surface-fluid combination coefficient	
d	Tube diameter	m
D_h	Hydraulic diameter	m
g	Gravitational acceleration	$\mathrm{m/s^2}$
h	Heat transfer coefficient	$\mathrm{W/m^2.K}$
h_{fg}	Latent heat of vaporisation	$\mathrm{J/kg}$
k	Thermal conductivity	$\mathrm{W/m.K}$
K	Turbulent kinetic energy	$\mathrm{m^2/s^2}$
L_e	Effective length	m
L_t	Tube length	m
$\dot{m}$	Mass flow rate	$\mathrm{kg/s}$
M	Molar mass of water	$\mathrm{g/mol}$
N	Number of tubes	
N_p	Number of pipes/tubes	
Nu	Nusselt number	
P_{atm}	Atmospheric pressure	Pa
P_{cr}	Critical pressure	Pa
Pr	Prandtl number	
P_r	Pressure ratio	
P_{wetted}	Wetted perimeter	m
q	Heat transfer rate	W
$\dot{q}$	Heat flux	$\mathrm{w/m^2}$
r_{in}	Inner radius	m
r_{out}	Outer radius	m
R	Thermal resistance	$\mathrm{K/W}$

Re	Reynolds number	
S	Flow cross-section area	m^2
S_k	Flow cross-section area (including tubes)	m^2
T	Temperature	$°\mathrm{C}$ or K
u	Velocity	$\mathrm{m/s}$
$\sum x$	Sum of the clear distances between tubes	m
y	Normal distance from the wall	m
y^+	Dimensionless y	
∂	Partial derivative	

Greek Letters

Δ	Difference	
ε	Turbulent dissipation rate	$\mathrm{m}^2/\mathrm{s}^3$
μ	Dynamic viscosity	$\mathrm{kg/m.s}$
ρ	Density	$\mathrm{kg/m}^3$
σ	Surface tension	$\mathrm{N/m}$
$\sum$	Sum	
τ	Shear stress	Pa

Subscripts

a	Annular
c	Condenser
cr	Critical
e	Evaporator
f	Fluid/bulk
g	Gas/vapour
h	Convection
i	Inner
k	Conduction
o	Ring opening
s	Surface/wall
t	Total
w	Wall/surface

Chapter 1. INTRODUCTION

1.1. Research motivation

Why heat exchangers

It is generally accepted that throughout history, especially after the industrial revolution, humans have had a negative impact on the environment. A clear increase in the earth's average temperature has been observed for some years and the world's leading climate scientists believe that this rise in temperature is directly related to mankind's activities [1], such as the burning of fossil fuels, deforestation and livestock farming. Those activities produce gases which act in a similar way to the glass in a greenhouse, permitting short-wavelength solar radiation to be incident on the earth's surface but absorbing long-wavelength infra-red radiation from the earth, thereby increasing global temperatures. Gases produced by human activities include, in particular, carbon dioxide, methane, nitrous oxide and fluorinated gases. Carbon dioxide is the major greenhouse gas (GHG) which contributes 64% of man-made global warming and its concentration in the atmosphere is currently 40% higher than when industrialisation began [2]. Other GHGs contribute less to global warming: 17% for methane and 6% for nitrous oxide, although they are more efficient at absorbing infra-red radiation than carbon dioxide.

Average global temperatures have been observed to have risen by about 0.85°C in the past 150 years (50% of the rise in the past 20 years) and they are subject to still further increases. If they exceed 2°C there is a risk of dangerous changes in human and natural systems [2] and actions have been taken by the United Nations Framework Convention on Climate Change (UNFCCC). The objective was to level off GHG emissions in this decade and to reduce them by 50% compared to 1990 levels by 2050. In order to achieve a reduction in GHGs, the European Union (EU) has imposed some policies including the increased use of renewable energy sources and a continual improvement in the energy efficiency of a wide range of systems [3]. EU leaders have also set several targets to be met by 2020. These targets were proposed in 2007 and agreed in 2009, including a 20% reduction in GHG emissions, 20% of energy to come from renewables and a 20% improvement in energy efficiency [4].

Companies involved in building services and process industries have therefore been forced to design more sustainable and energy efficient systems [5–7] to meet the EU targets. Exhaust gases generated from such activities release both GHGs and waste heat to the atmosphere and they are a significant contributor to global warming. Waste heat could be recovered and/or recycled through heat exchanger (HX) systems to be reused within the industrial processes, which would save energy and decrease the power consumption coming from fossil fuels, hence reducing GHG emissions.

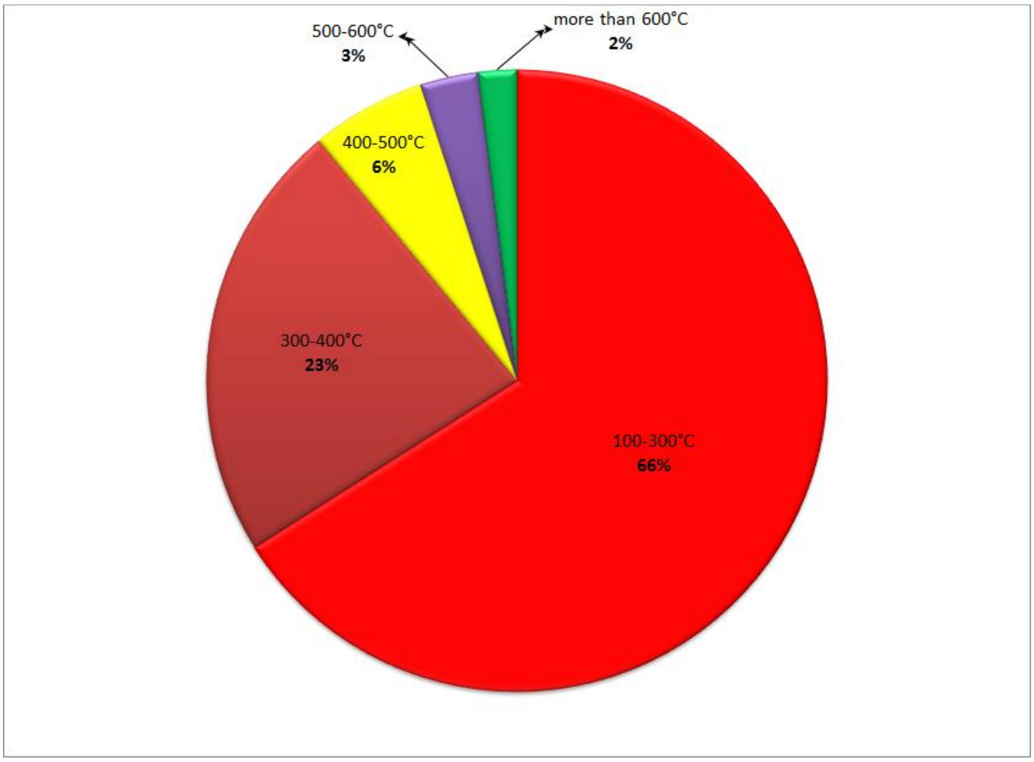

Figure 1.1 – Waste heat energy for different temperature range.

Heat exchangers (HX), as the name indicates, are systems that absorb heat from unwanted sources and transfer it to a place where it will be beneficially applied. According to Figure 1.1, Haddad et al. [8] claimed that 66% of the waste heat is generated from systems that operate at medium temperature range (100-300°C) where the heat exchanger studied in this project lies within. Consequently, it is important to improve the thermal performance of such systems. Heat exchangers come in different shapes and sizes depending on the type of application.

Conventional HX consists of a shell and a tube side where two fluids at different temperatures exist and exchange heat. A new technology has recently received the attention of many researchers where it integrates the use of heat pipes instead of conventional tubes within the heat exchanger [6].

Why multi-pass?

The 'Through Flow Unit' (TFU) shown in Figure 1.2, is a name that was given by Jouhara [9] to a Disk-and-Doughnut heat pipe-based heat exchanger (DD-HX) system. The design is a break-through in terms of integrating the thermosyphon technology within the Disk-and-Doughnut heat exchanger. This increases the heat transfer coefficient of the system and adds more flexibility to the system during installation (Figure 1.2 and 1.3). Therefore, understanding the fluid flow and heat transfer inside it, is important for future designs of similar multi-pass thermosyphon-based heat exchanger systems.

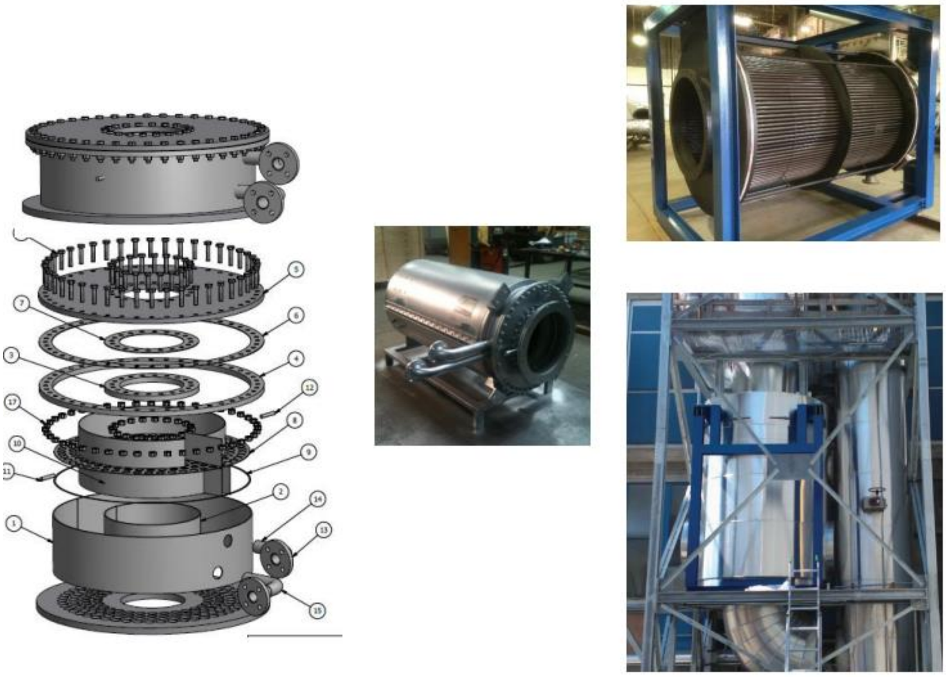

Figure 1.2 – The through flow unit designed by Jouhara [9,10]***.***

Figure 1.3 – Through flow unit in series with the duct [10].

Looking at Figure 1.4, a comparison is shown between two thermosyphon-based-heat exchangers, a cross-flow and a multi-pass configuration. For the same exhaust inlet mass flow rate and area, the multi-pass offers the following advantages:

- A higher Reynolds number than the cross-flow configuration, which results in a higher Nusselt number, hence a higher convective heat transfer coefficient
- In the case of the cross-flow configuration, the first row of heat pipes is exposed to the high temperature exhaust inlet; this creates a very high temperature zone, shown in Figure 1.4. The hot spot could lead to a failure of the entire HX system. However, employing a multi-pass configuration would result in normalising the working temperature in all the pipes (Figure 1.4)
- Normalising of the thermosyphon working temperature will allow a much higher exhaust temperature to enter the HX system

Although the mutli-pass offer many advantages over the cross flow configuration, the pressure drop must be always taken into account as it is a major limitation of this system.

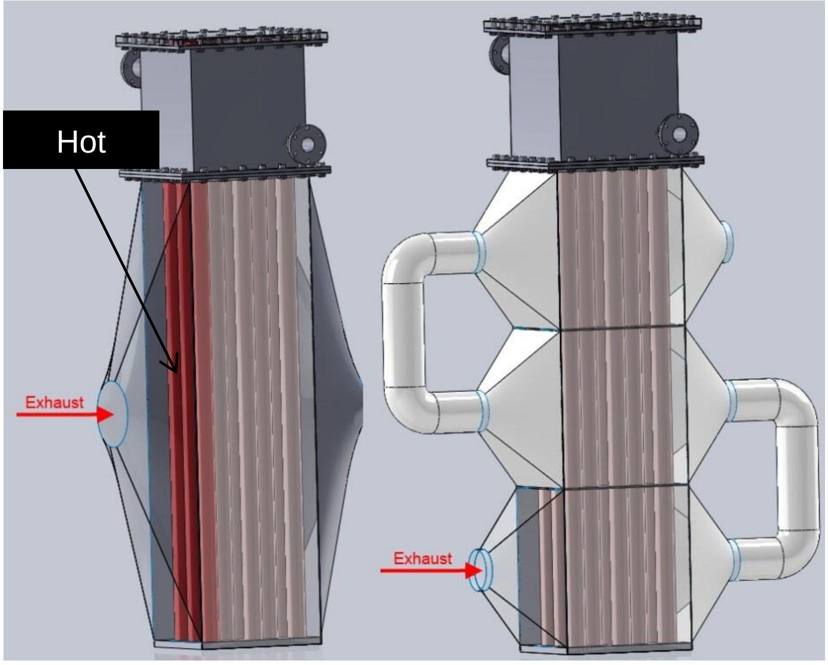

Figure 1.4 – Comparison between a cross-flow and a multi-pass configuration.

1.2. Aims

- To carry out a detailed analysis of the fluid flow and heat transfer behaviour of an air-to-water mutli-pass heat exchanger system integrated with thermosyphon technology
- To create a fully validated numerical model to investigate the effect of different multi-pass configurations and inlet conditions on the thermal performance of the system

1.3. Objectives

In order to achieve the aims, the below tasks were to follow:

- Identifying all the different heat transfer modes that exist on the shell side and inside the thermosyphons in both evaporator and condenser
- Carrying an experimental tests of a single thermosyphon to understand its thermal behaviour for various heating inputs and working fluids
- Investigating various pool boiling correlations to choose the best suitable one to be used within the theoretical model
- Theoretical prediction of the thermal performance for the entire system based on heat transfer correlations adopted from the literature

- Calculating the thermal conductivity for each inlet condition to replace both evaporation and condensation regimes inside the thermosyphons
- Developing a numerical model using ANSYS Fluent to study the effect of multiple shell passes configurations for various inlet conditions
- Building a test rig to validate the numerical model at all inlet conditions
- Conducting an uncertainty analysis to gain confidence of the experimental data

1.4. Thesis structure

The thesis is divided into 5 chapters. It starts with an introduction to explain the scope of the project (chapters 1 and 2). Subsequently, chapter 3 discusses all the methodologies that have been attempted in the project including theoretical, numerical and experimental investigations. Finally, chapter 5 discusses all the results, providing conclusions and recommendations for future work.

Chapter 1: The first chapter highlights the reason behind the importance of characterising such types of multi-pass heat exchanger systems equipped with thermosyphon technology. A brief description detailing the need of such projects based on their positive environmental impact, starting from the global warming issue that has imposed strict legislations on companies to produce more efficient systems. Consequently, outlining the aims and objectives of this project.

Chapter 2: This chapter presents the state of the art of multi-pass systems that have been previously investigated. More specifically, a literature review is presented on numerical (using ANSYS Fluent package) and theoretical modelling of shell and tube heat exchangers where the heat exchanger portrayed in this project lies under the same classification, with the novelty that the thermosyphon technology is integrated instead of conventional tubes.

Chapter 3: All the methodologies followed in this project were combined in this chapter and explained in details. Such methodologies include theoretical (thermal resistance analogy) numerical (using ANSYS Fluent) and experimental (single thermosyphon and multi-pass).

Chapter 4: All the results are summarised in this chapter: theoretical, numerical and experimental. Initially, the chapter begins by analysing the results that were generated from the single thermosyphon tests to gain a good understanding of this technology as it is integrated within the multi-pass system. Afterwards, a validation test and discussions of the results are presented.

Chapter 5: After the discussion of all the results, this chapter provides a summary and draws conclusions for all the work that has been conducted in this project. Finally, a list of recommendations is proposed for future related work.

Chapter 2. LITERATURE REVIEW

Heat exchangers are devices that have the duty to transfer heat between two or more fluids. In most heat exchangers, the two fluids are separated by a heat transfer surface where the two fluids do not mix. Those heat exchangers are referred to as direct heat transfer type, or simply recuperators, where the heat transfer takes place by conduction through the separating wall. Heat exchangers are widely used in various industrial sectors, including petro-chemicals, refrigeration, air conditioning, waste heat recovery and so on.

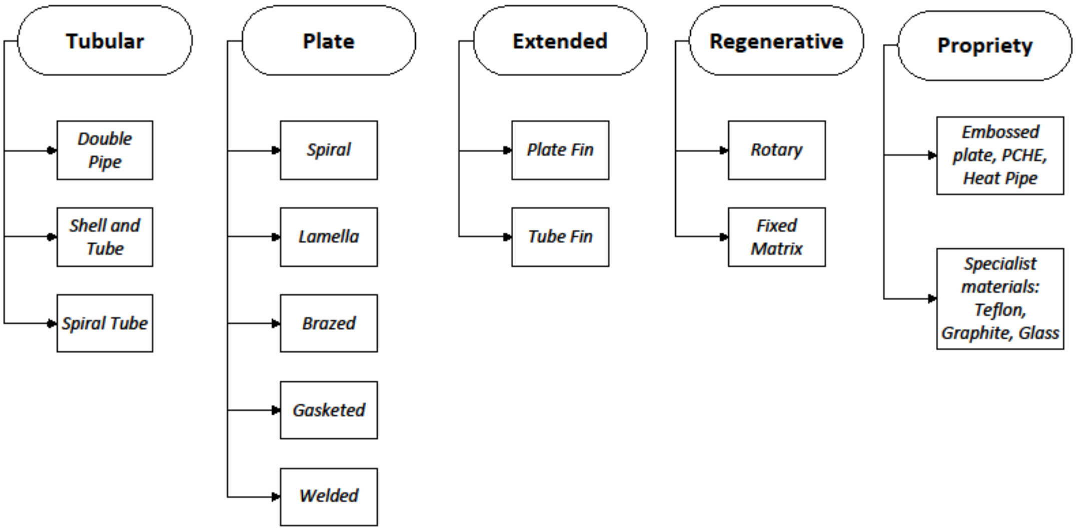

Figure 2.1 – Brief classifications of heat exchangers.

The simplest type of heat exchangers used in industries is the double pipe (DPHX). Due to their cheap design and maintenance, the use of such types is ideal for small industries. When higher efficiency and smaller size systems became more important, modern industries replaced the double pipe heat exchangers with more efficient systems such as shell-and-tube and plate heat exchangers. There are various types of heat exchangers (Figure 2.1), however, choosing the most appropriate one for an industrial process is a difficult task. In fact, selecting the wrong type of heat exchanger for a specific application could lead to several issues, including under-optimal performance, operability and equipment failure [11].

Figure 2.1 shows a classification by construction of various types of heat exchangers, where the common types of heat exchangers are either tubular and plate. Heat exchangers can be classified in various type based on principle of operation, structure and phases of fluid involved:

Transfer process:

According to the transfer process, heat exchangers can be divided into direct and indirect-contact type. In an indirect type, the two fluids between which the thermal energy is transferred are separated by a conductive material. This type is also known as surface heat exchanger, and can be further classified into direct-transfer type, fluidized-bed and storage type heat exchangers. Within the direct-transfer type, the fluid nature can be either single or multi-phase flow. On the other hand, the direct-contact type consists of two immiscible fluids, gas-liquid or liquid-vapour exchangers that are brought into direct contact, where no separating surface exists between them. Common applications include evaporative cooling and rectification. Due to the absence of the heat transfer surface, the direct-contact type offers several advantages over the indirect-contact type. (1) A higher heat transfer rate is achieved due to the direct contact between the fluids, (2) the fouling problem is generally inexistent and (3) the construction of the system is relatively cheap.

Number of fluids

In most heat exchangers, the transfer of heat occurs between two fluids, such in heating, cooling, heat recovery and heat rejection. In few heat exchangers, mainly in cryogenic applications and some chemical processes (purification, liquefaction etc.), three fluids are used. In some chemical processes, a total of 12 fluid streams have been used.

Surface compactness

Compactness is defined by the ratio of the heat transfer surface area to the volume of the heat exchanger. Compared to shell-and-tube heat exchanger, compact heat exchangers offer many advantages such as, reduction in weight, cost, space and energy requirements.

2.1. Plate heat exchangers (PHXs)

Plate heat exchangers are considered as compact in structure, as well as cheaper compared to shell-and-tube HXs. It consists of metal rectangular plates arranged in a parallel configuration, and held together by gaskets which are located at the corners of each plate. As shown in Figure 2.2, both cold and hot fluids are directed and sealed through the gaskets in between. The heat transfer takes places across the plates.

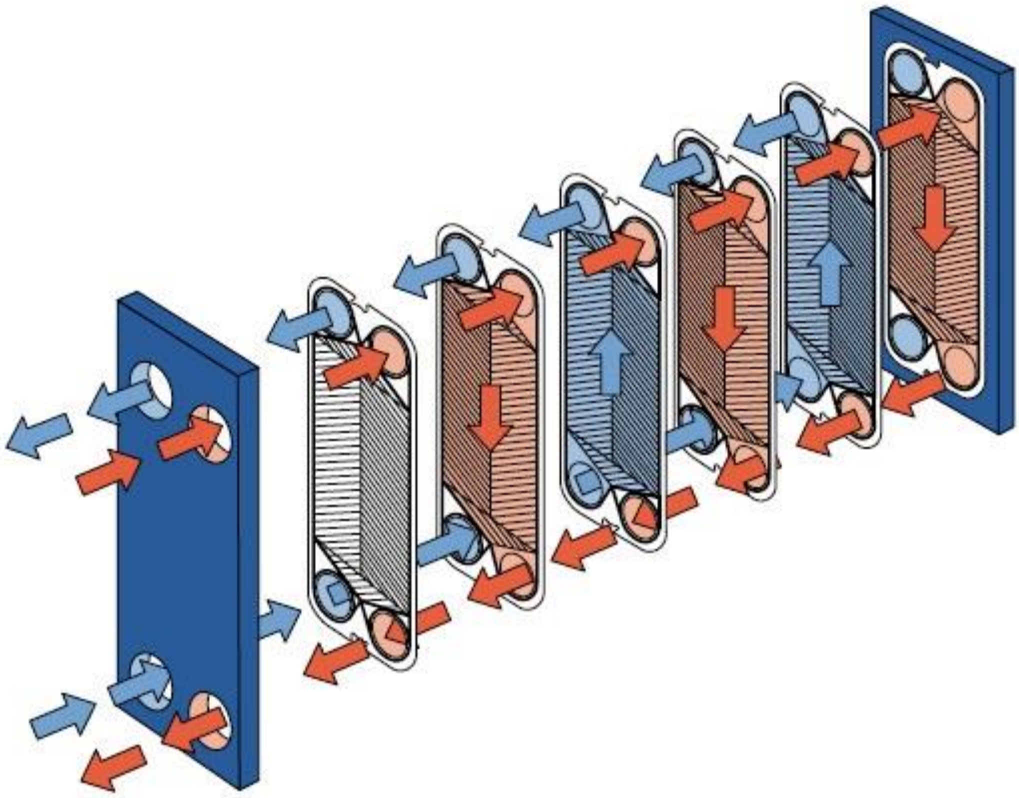

Figure 2.2 – Schematic of a plate heat exchanger.

In general, heat transfer enhancement can be achieved by adding extended surfaces (i.e fins) or modifying the surface geometry, which is the case for the PHX. The plates are modified by introducing corrugations to interrupt the plate surface to induce turbulence and hence increasing the rate of heat transfer. Introducing interrupted surfaces (i.e corrugations) will not only cause higher heat transfer, but helps the heat exchanger to produce a self-cleaning nature. This would eventually reduce the fouling effect. Chevron design is the most common surface pattern used for plate surface (Figure 2.3).

Figure 2.3 – Chevron design pattern (PHX).

Plate heat exchangers designs are continuously developing in order enhance the overall performance by improving the reliability and maintainability of the system. Different category designs include frame-and-plate (FPHX), brazed-plate (BPHX) and shell-plate [12]. Due to the high pressure, FPHXs were only suitable for low pressure applications (below 1.6 MPa). Such applications involve gas-to-gas heat transfer. The material used for the gaskets (limits the maximum pressure and operating temperature to 2.5 MPa and 150°C, respectively [13]. With the introduction of BPHX, the plates were able to withstand higher pressure. This has increased their applications as evaporators, condensers, HVAC and refrigeration systems [12].

Except for the shell-and-tube heat exchanger type, which will be described in the next section, less popular heat exchangers exist. This includes plate-fin and spiral-plate heat exchangers.

2.2. Shell-and-tube heat exchangers (STHXs)

2.2.1. Experimental and theoretical approaches

Shell-and-tube is a type of heat exchanger (HX) that is widely used in various industrial areas including petroleum refining, processing, chemical engineering and power plants. It consists of two fluids flowing at different temperatures, one fluid flowing in tubes and the other flowing in a shell side around the tubes, with the only heat transfer being at the tube surface. Two heat transfer mechanisms exist inside the system, including two convection mechanisms inside and outside the tubes, and conduction through the tube wall thickness. However, thermal radiation may be of significance for high-temperature applications [14]. The flow of the two fluids can be classified into three patterns: parallel, counter flow or cross flow.

In a parallel flow shell-and-tube heat exchanger, the two fluids in the tube and shell side enter the HX from the same side with a large temperature difference (Figure 2.4). The temperature difference reduces gradually with the heat transfer in the direction towards the fluid exit.

The counter flow STHX is another type of HX where each fluid enters the HX from opposite sides. This flow pattern is the most efficient type in the heat transfer industries due to the maximised temperature difference between the two fluids throughout the length of the tubes; therefore, a higher heat transfer rate is achieved per unit area [15].

A third type of flow pattern is the cross flow STHX, where the two fluids enter the HX in perpendicular directions. This type of HX is usually found in applications where one fluid changes its state (two-phase flow).

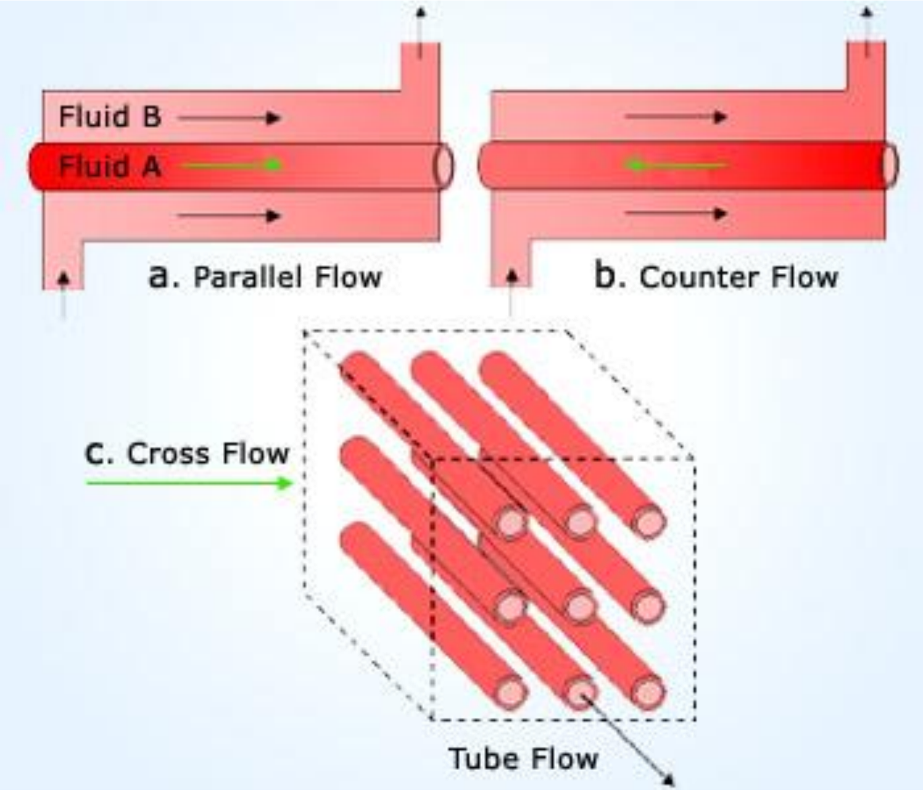

Figure 2.4 – Parallel (a), Counter flow (b) and Cross flow pattern (c) [16]***.***

A variety of HXs are used in industries including shell-and-tube, fin-plate and fin-and-tube HXs. According to Master et al [17], more than 30-40% of HXs available in heat transfer processes are shell-and-tube HXs. The reason is due to their ease of maintenance, robust construction geometry and availability of possible improvements and upgrades [18].

The design and size of a heat exchanger involve many complex processes [19] which contribute to the final design. Important factors include the amount of heat transfer, pressure drop, manufacturing, operating and maintenance costs. Depending on the application, the overall cost could be important while in other cases the size and weight are the most significant factors.

When designing the shell side of a STHX, there are two common methods that have been widely used by designers, namely Bell-Delaware [20] and the Kern method [21,22].

The Bell-Delaware method provides a very detailed analysis of the shell side of a heat exchanger. It also provides an accurate estimation of the shell side heat transfer coefficient and pressure drop for common shell side heat exchangers.

This method applies correction factors to the calculated heat transfer coefficient to account for the following elements [23]:

- Leakages that exist between the baffles and the tubes, also between the baffles and the shell
- By-passes between the tube bundle and the shell
- Effect of adverse temperature gradient on the heat transfer for low Re (less than 100), the validity is however considered doubtful

To obtain general performance parameters (rating), the Bell-Delaware method can predict the possible weaknesses in the design; however, it cannot identify where the weaknesses are.

The Kern method is only suitable for preliminary shell-side sizing. The method is based on experimental work for commercial heat exchangers. It offers the following advantages:

- Provides reasonably satisfactory prediction of the HTC for standard designs
- Simple to apply
- Accurate enough for preliminary designs

As this method does not take into account the leakages and bypasses streams that exist within the heat exchanger, it draws advantages with providing less satisfactory prediction of the pressure drop [22].

In recent years, researchers have been developing the design of the STHX to improve its overall performance by enhancing the heat transfer while maintaining a reasonable pressure drop. One way to enhance the heat transfer in the shell side of the STHX is by inserting baffles, which have many advantages in the performance improvement.

The main reason for installing baffles in the STHX is to change the flow direction by creating effective multiple fluid passes and circulation around the tubes, hence providing an effective use of the heat transfer area. Introducing baffles have led to a significant improvement in the thermal performance of STHXs, by increasing the turbulence or local mixing that is due to flow separation occurring at the baffle edge in case of segmental baffles; however, it increases the so-called “dead zones”. Another advantage of the baffles is to support the tube bundles in a way as to prevent vibration, which can be caused by the high pressure drop. The pressure drop due to baffles is much larger than that due to the tube bundle. The presence of the tube bundle has a positive overall effect as it smoothens out the velocity distribution as well as reducing the recirculation regions.

Baffle cut and spacing are very sensitive to the flow direction and heat transfer characteristics, providing researchers the opportunity to look for ways to optimise the performance of STHXs by investigating various baffle geometries and spacing. The optimisation will compromise between the reduction in the pressure drop and the increase in the heat transfer. Such geometries include segmental, continuous and non-continuous helical and Disk-and-Doughnut baffle type. Figure 2.5 shows a segmental baffle type where the effects of the baffle cut and spacing on the main stream are illustrated schematically. Figure 2.5 (a) and (b) represents the schematic of the flow stream when increasing the baffle cut. It can be clearly seen that an increase in the baffle cut would reduce the sudden change in the velocity gradient (reduced pressure drop), however an increase in the circulation zones occur where the heat transfer corresponding to that cannot be used effectively. Looking at Figure 2.4 (c) and (d) where having a small baffle spacing (c) would allow the flow stream passing the cut window to be reflected by the next baffle. This results in a sudden change in the velocity gradient (higher pressure induced) and again unwanted recirculation zones to be formed. Hence, the ideal configuration (e) will have a compromise between a smooth flow stream and the least recirculation zones behind baffles.

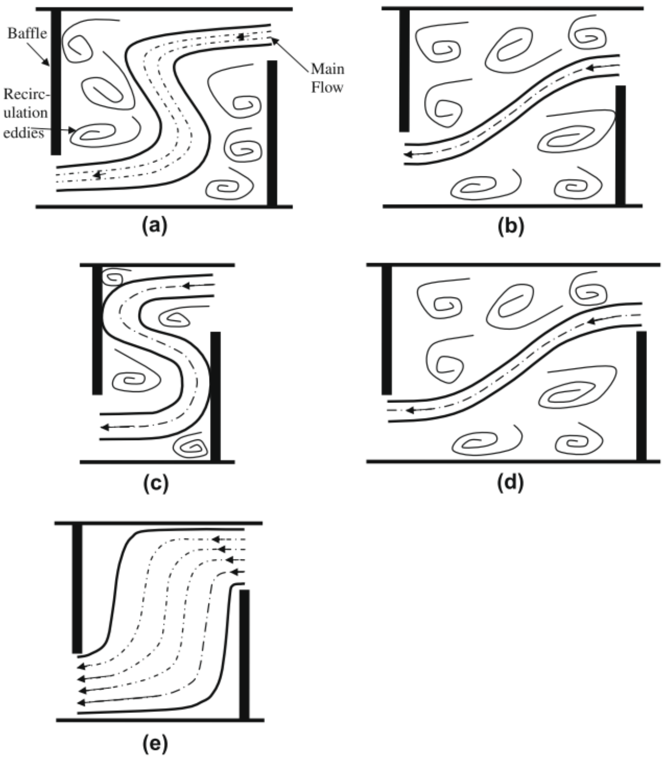

Figure 2.5 – Segmental baffle type: (a) small baffle cut, (b) large baffle cut, (c) small baffle spacing, (d) large baffle spacing, (e) ideal baffle cut and baffle spacing [24].

The segmental baffle type (Figure 2.6) is the most commonly used configuration and its importance comes from forcing the fluid on the shell side to flow in a multiple (zigzag manner) passage across the tube bundle. This keeps the fluid longer in contact with the tubes and therefore enhances the thermal performance of the HX, but it induces a large pressure drop caused by the contraction and expansion of the fluid due to the change of the area. The change of area causes a sudden change in the velocity gradient, creating a large pressure drop across the heat exchanger. Therefore, larger power consumption will be needed to push the fluid inside the shell side. This large pressure drop also induces vibration, which can cause a high risk of tube bundle failure.

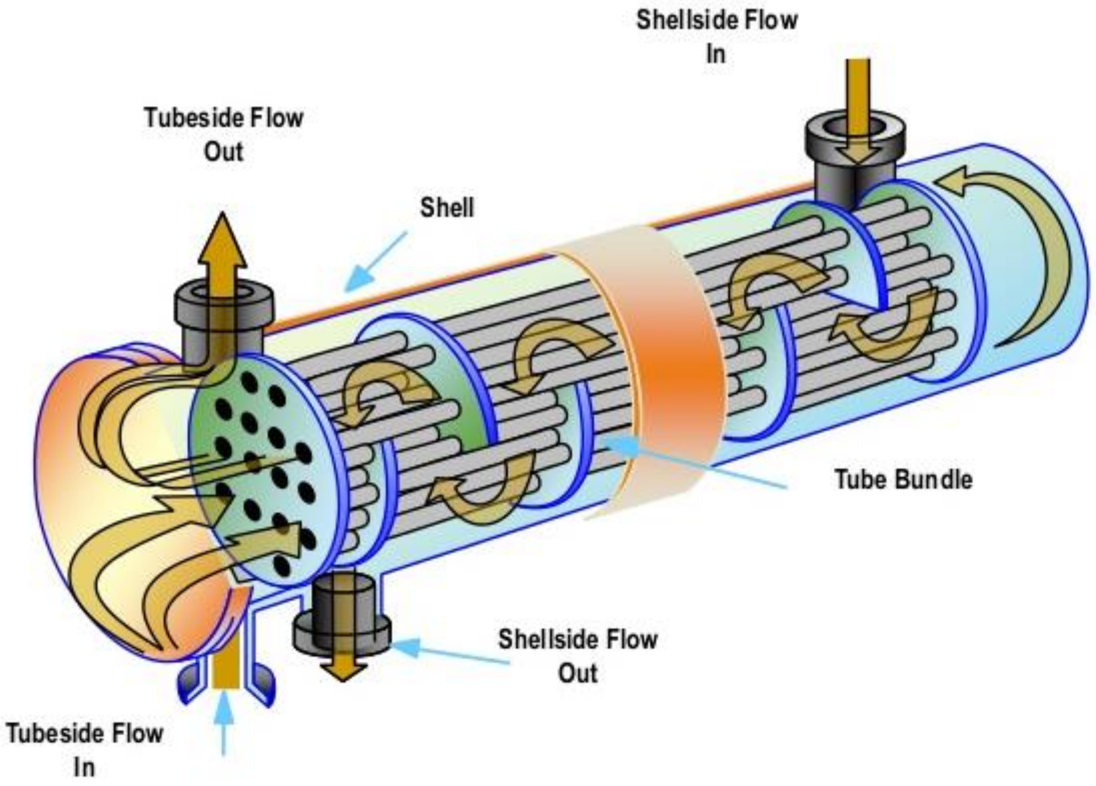

Figure 2.6 – Segmental baffle in a STHX [25].

A possible alternative baffle configuration that has been used over the years is the helical shaped baffle. It has a major advantage over the conventional segmental baffle in that it eliminates the dead zones by maintaining a helical flow throughout the HX. The helical flow reduces the sudden change in the flow direction, as well as maintaining a uniform area between the baffle cut and shell surface in the case of segmental baffles [26]. This advantage results in a reduction in the pressure drop, as well as lowering the risk of tube vibration.

The dead zones or stagnation regions presented in the STHXs that were mentioned earlier are located behind the baffles (Figure 2.5), in the corners between baffles and shell wall where the velocity of the fluid is very small, which gives a high potential of the particles inside the fluid to deposit on the outer tube wall surface. This phenomenon is termed as fouling which is mainly caused by the uneven velocity profile created by the presence of baffles in addition to back-flows and eddies generation [17]. The change in the baffle geometry, i.e. helical or Disk-and-Doughnut, has shown a reduction of the fouling effect and an increase in the overall performance [27].

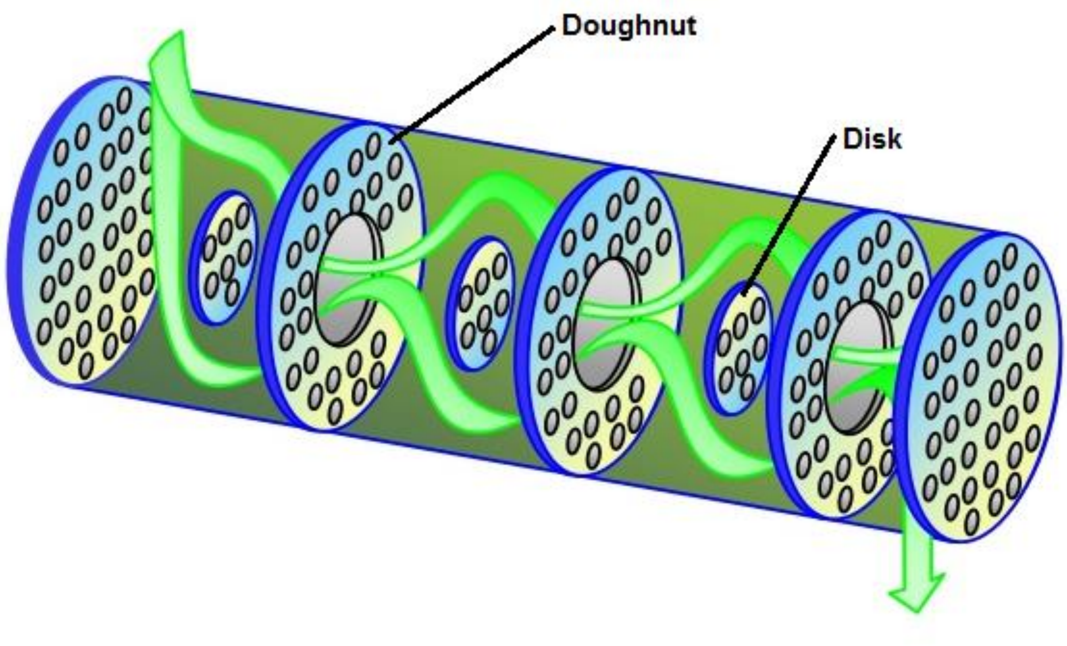

Figure 2.7 – Disk-and-Doughnut schematic [25]**.**

Based on the literature, the concept of multiple pass in the case of STHX has been successful in enhancing the shell side heat transfer.

The main focus of researchers now is to optimise the shape of the baffles to overcome the downside of conventional segmental baffle to enhance the heat transfer coefficient, lower tube vibration and reduce fouling. To tackle the mentioned drawbacks, the use of different shaped baffles such as deflector baffle, disk-and-doughnut configuration and optimising the spacing between baffles was investigated.

As mentioned before, a full understanding of the flow phenomenon should be carried out in order to identify the causes of the problems located within the shell-side design of a heat exchanger. The majority of STHX studies only focused on certain features of the design. Certain parts of the STHX include baffle cut, spacing, shell-side heat transfer, tube arrangements and pressure drop. Pekdemir et al. [28] and Halle et al. [29] worked on the pressure drop of the STHX, while Gay et al. [30] investigated the shell-side heat transfer. Amongst others, the effect of the tube arrangement on the heat transfer were investigated by Li and Kottke [31,32] and Karno and Ajib [33]. The effect of baffle spacing on the heat transfer and pressure drop was investigated by Eryener [34] and Sparrow and Reifschneider [35]. All the various analytical, experimental and numerical studies have concluded that the most important geometrical parameters on the heat transfer and pressure drop are the baffle cut and spacing.

Zhang et al. [18] conducted an experimental investigation to study the effect of segmental and helical baffles on the pressure drop and heat transfer coefficient of the STHX. With the same shell side flow rate, it was found that the heat transfer coefficient of STHX with segmental baffles is higher than that of the helical. However, the pressure drop with helical baffles was lower than that with segmental. Zhang et al. [18] also compared the performance of the STHX with helical baffles at different helix angles (20°, 30°, 40° and 50°). The results showed that the STHX with 40° helix angle outperformed the other tested heat exchangers.

Peng et al. [36] designed and tested the use of continuous helical and segmental baffles in STHXs, with both having the same tube bundle. The flow pattern in the shell side of the continuous helical baffles was forced to follow a rotational and a helical passage. The rotational helical flow has resulted in a significant increase in the heat transfer coefficient per unit pressure drop. Peng et al. [36] suggested that properly designed continuous helical baffles could reduce fouling in the shell side, as well as tube vibration. A performance comparison between continuous helical baffles and segmental baffles was experimentally carried out and it was found that continuous helical baffles resulted in nearly 10% improvement of the heat transfer coefficient for the same shell side pressure drop.

2.2.2. Numerical approach (Computational Fluid Dynamics)

Conducting experimental tests is a well-known method to analyse the fluid flow and thermal behaviour in any heat exchanger system. However, setting up an experiment is a time-consuming and relatively expensive task. Also, experimental tests do not have the ability to visualise the fluid flow and thermal behaviour inside the heat exchanger system, therefore researchers have developed a tool using Computational Fluid Dynamics (CFD) that numerically analyses the fluid flow, heat transfer and chemical reactions by solving mathematical equations inside the heat exchanger.

CFD simulation has become a powerful and accurate tool to predict the heat transfer mechanisms and velocity distribution in heat exchanger systems [37]. In addition to experimental and theoretical investigations, many researchers have also conducted numerical investigations using CFD packages to analyse the thermal performance and fluid flow behaviour of such systems including STHX [38–40] type, which is the main interest in this project.

Due to the complex fluid mechanics and heat transfer mechanisms presented on the shell-side of STHXs, CFD has become an alternative for researchers to study the shell-side design weaknesses, understanding the flow phenomenon and heat transfer behaviour numerically for multi-pass HXs, in addition to flow visualisation, flow pattern and temperature field which experimental testing cannot achieve [41]. Furthermore, CFD is an important tool to reduce the number of testing prototypes as it provides a useful preliminary design step in terms of good insight of the various flow and thermal transport phenomena that occur within the heat exchanger system [42]. Successful CFD modelling for a detailed industrial heat exchanger is, however, limited. A large computer power and memory is required to perform this analysis, in addition to the long computation time. In this case, simplification of the actual system is a mandatory task. Speaking of an industrial shell-and-tube heat exchanger containing 500 tubes and 10 baffles, the number of elements needed to run the simulation is at least 150 million [39]. One of the common approaches used in simplifications in CFD modelling are the electrical resistance analogy approach and the porous medium model, both were used by many researchers including Prithiviraj at al. [38,39] and Stevanovic [43]. The results have shown good agreement for the shell-side heat transfer coefficient and pressure drop for both approaches. However, a full CFD model of the entire system is needed for the purpose of visualising the shell-side flow and temperature distribution. The detailed modelling of the system can be used to predict important parameters, including the heat transfer coefficient and pressure drop, which will be compared to theoretical correlations. The visualisation of the flow is also important in order to identify weaknesses within the design. The weaknesses include relaminarisation and recirculation zones which can greatly affect the thermal performance of the heat exchanger.

Yonghua et al. [41] conducted an experimental and numerical investigation using Fluent to analyse the heat transfer and flow distribution on the shell-side of a STHX with flower baffles (FB-STHX). Younghua et al. [41] found that the heat transfer rate was effectively enhanced on the shell side of the FB-STHX compared to the heat exchanger without baffles. They also compared the shell side velocity distribution between FB and SG-STHX (segmental baffles STHX); it was found that the flow patterns differ between the two cases and the overall thermal hydraulic performance for the FB-STHX is better than that of the SG-STHX. This research has proved that Fluent is a powerful tool to predict the thermal performance of the single phase flow in multi-pass HXs with low computational cost.

Eshita et al. [44] numerically investigated the complex flow and temperature pattern for different flow rates inside the shell side of a short STHX using Fluent. The following points were observed during this numerical investigation:

- $K - \varepsilon$ turbulence model produced the best results in terms of velocity profile and heat transfer with an accuracy within 20% envelope compared to experimental results
- Fluent also predicted a pressure drop within 10% agreement of the one estimated by the Bell-Delaware method in baffled HXs [45]
- The convergence was improved as the inlet velocity profile was fully developed
- The STHX exit length was also investigated and it was found that the convergence improved as the outlet velocity became fully developed with increasing length

This investigation has proved again that Fluent is an efficient tool for predicting fluid flows in HXs, in addition to giving guidelines for optimum design.

Nemati Taher et al. [46] conducted a numerical investigation using Fluent to analyse the effect of non-continuous helical baffles on the performance of a STHX. Nemati Taher et al. [46] conducted this numerical simulation at 40° helix angle and 5 different baffle spaces. The 40° helix angle had already proven to be the optimum helix angle performance in helical baffles [18]. Results have shown that the more extended baffle space produced higher heat transfer and a lower pressure gradient. For the same mass flow rate, increasing the baffle space showed a decrease in heat transfer per unit area.

In general, there is no specific turbulence model which is favourable or applicable for all types of engineering problems. Instead, a good understanding of the system under investigation is essential and makes it easier to choose the most appropriate turbulence model. Depending on various considerations, the problem should be well studied, preferably theoretically if possible, to understand the fluid flow and thermal behaviour involved within the application to be modelled. Other considerations include the available computational cost and time, in addition to the level of accuracy required to generate results. This is important as some turbulence models take longer in terms of computational time, however they may produce better results quality. In conclusion, a suitable choice of the turbulence model is necessary and achieved through studying both capabilities and limitations of the numerous options.

The most common RANS equations (time averaged) classical turbulence models are as follows:

1- One equation model: Spallart-Almaras
2- Two equation model: $K-\varepsilon$ models (Standard, RNG and realizable), $K-\omega$ model and Algebraic stress model (ASM)
3- Seven equation model: Reynolds stress model

An increase in the number of equations indicates an increase in the number of partial differential equations (PDEs) that are being solved.

RANS turbulence models can be classified between low and high Re models. The low Re models are recommended in cases where the target is to predict the boundary layer velocity or thermal profile, moreover, if a boundary layer separation is expected, precisely due to the change in the pressure gradient. Those models are also recommended for problems where the pressure-drop and drags are important. In such cases, the Shear Stress Transport (SST) ω-based model is highly recommended.

For high speed cases, the Spallart-Almaras model is recommended for aerodynamics external flows. In cases where wall-bounded effects are not important, or separation is expected to take place due to presence of sharp edges within the geometry, $K - \varepsilon$ models are generally adopted.

The two-equation $K - \varepsilon$ turbulence models are very popular for a wide range of industrial turbulent flows and heat transfer simulations due to being robust, economical in terms of computational effort and cost, and finally, realistically accurate. Due to the insensitivity to boundary layer separation over smooth surfaces and adverse pressure gradients, those models suffer from an inherent draw-back as the models delay the prediction of such separations compared to reality. This prediction delay, eventually, results in an optimistic design. In any case, the boundary layer study and separation is not a point of interest in the heat exchanger under investigation.

There are two important ways in which the Realizable $K - \varepsilon$ model differs from the standard $K - \varepsilon$:

- An alternative formulation for the turbulent viscosity is contained within the realizable $K - \varepsilon$ model
- A modified transport equation for the dissipation rate ε

The K transport equation was kept the same for both Standard and Realizable models. To address the deficiency of the standard model, a new formulation of the dissipation rate ε equation was adopted based on a transport equation for the mean-square vorticity fluctuation. The turbulent viscosity μ_t has also been modified based on a new formulation of C_μ shown in equation (2.4).

The use of the Realizable $K - \varepsilon$ turbulent model has many advantages over the standard $K - \varepsilon$ [47,48]:

- Better performance
- The effect of compressibility and buoyancy can be included
- Suitable for complex flows including large strain rates such that recirculation, rotation, separation and strong pressure gradient can be modelled.

However, the Realizable $K - \varepsilon$ model still suffers from the inherent limitations of an isotropic eddy-viscosity model [47,48].

The Realizable $K-\varepsilon$ model transport equations are as follows [47,48]:

K-transport equation:

$$\rho\frac{DK}{Dt}=\frac{\partial}{\partial x_j}\left[\left(\mu+\frac{\mu_t}{\sigma_K}\right)\frac{\partial K}{\partial x_j}\right]+\mu_t S^2-\rho\varepsilon \tag{2.1}$$

where $S=\sqrt{2S_{ij}S_{ij}}$

ε-transport equation:

$$\rho\frac{D\varepsilon}{Dt}=\frac{\partial}{\partial x_j}\left[\left(\mu+\frac{\mu_t}{\sigma_\varepsilon}\right)\frac{\partial \varepsilon}{\partial x_j}\right]+C_1 S\rho\varepsilon-C_2\frac{\rho\varepsilon^2}{K+\sqrt{\nu\varepsilon}} \tag{2.2}$$

where

$$C_1=\max\left[0.43,\frac{\eta}{\eta+5}\right],\ \eta=\frac{SK}{\varepsilon},\ \ C_2=1 \tag{2.3}$$

Turbulent Viscosity:

$$\mu_t=\rho C_\mu\frac{K^2}{\varepsilon},\ \ C_\mu=\frac{1}{A_0+A_s\frac{U^*K}{\varepsilon}} \tag{2.4}$$

where

$$A_0=4.04,\ \ A_s=\sqrt{6}cos\phi,\ \ \phi=\frac{1}{3}\cos^{-1}\left(\sqrt{6}\,W\right) \tag{2.5}$$

and

$$U^*\equiv\sqrt{S_{ij}S_{ij}+\Omega_{ij}\Omega_{ij}}\ ,\qquad W=\frac{S_{ij}S_{jk}S_{ki}}{\tilde{S}}\ ,\quad \tilde{S}=\sqrt{S_{ij}S_{ij}} \tag{2.6}$$

σ_k and σ_ε are known as the turbulent Prandtl numbers for k and ε, respectively. More specifically, these are empirical constants determined from benchmark experiments of simple flows using air and water. This model has been validated for a wide range of turbulent flows and was found to be substantially better than the standard $K - \varepsilon$ model [49].

2.2.3. Disk-and-doughnut baffle shell-and-tube heat exchanger (DD-HX) and DD-HX equipped with thermosyphons

The idea of DD-HX (Figure 2.7) has come from looking for a better way to optimise the fluid flow distribution and thermal performance of shell-and-tube heat exchangers. As the name indicates, the Disk-and-Doughnut configuration consists of two baffle types: a Disk and a Doughnut (see Figure 2.7 and Figure 2.8). This design forces the flow to alternate between longitudinal and transverse directions (cross-flow) to the tube bundle. The disk baffle has an annular area between the periphery of the disk and the inner shell wall; the doughnut has a circular opening at the centre of the baffle where the flow travels through. The two baffles are kept at the same distance throughout the heat exchanger. The fluid flows in a radial direction towards the periphery of the disk, then back radially towards the centre of the next doughnut (see Figure 2.8). The high performance of the DD-HX is due to the radial flow between the bundle centre and periphery. This radial flow reduces the stagnation regions that were caused by the use of segmental baffles. Short [50] has reported that DD-HXs have approximately a 15% higher heat transfer coefficient than SG-STHXs for the same pressure drop.

Disk and Doughnut heat exchangers were used in the 1940’s in the USA; however, they are rarely used now due to manufacturing problems and the lack of design methods of calculation [51]. It is occasionally used as oil coolers at thermal power stations in some European countries.

The idea of the design was born to overcome the shortcomings of the segmental baffles, such as the high pressure drop due to the sudden contraction and expansion of the fluid, low heat transfer efficiency due to the stagnation regions, short operation time due to vibration caused by the shell-side flow across the tube bundles and high pumping power needed to offset the higher pressure drop for the same heat load [52].

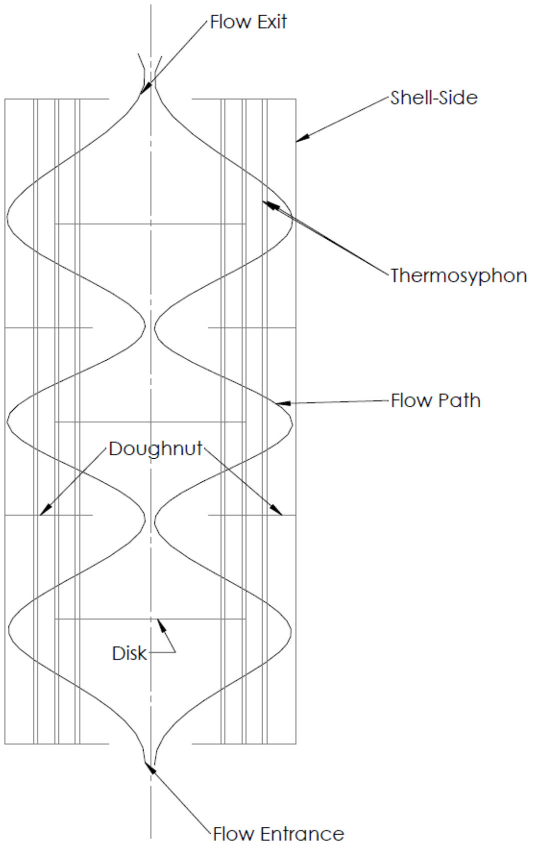

Figure 2.8 – Schematic of the through flow unit (Disk-and-Doughnut baffle) TSHX.

As mentioned before, the DD-HX configuration was born while searching for a better flow distribution and thermal performance [53]. The effect of the clearance between baffles has been well studied by researchers for the SG-STHX. Unfortunately, there is hardly any published literature available on the DD-HX configuration. Very few methods are available for its thermal design [54]. Amongst them are Donohue [55], Slipcevic [56,57] and Goyal et al. [58]. DD-HX did not achieve similar popularity as the SG-STHX, mainly due to manufacturing problems and lack of comparable data on heat transfer and pressure loss [59].

Founti et al. [53] characterised the flow pattern of a pipe-less DD-HX isothermally and demonstrated that the flow past the baffles was dominated by pressure gradients associated with strong streamline curvature. In addition, reducing the baffle spacing increased the streamline curvature, which resulted in a higher overall pressure drop. The strong streamline curvatures make the flow field independent of fluid velocity and turbulence intensity at the inlet. The other major quantitative details of the flow are that they are fully dependent of the relative position of its neighbouring baffles and not on the initial conditions [53].

Li et al. [59] showed that the average Nusselt number for the same Reynolds number (defined below) in the DD-HX is higher than that of a single SG-STHX, as well as the pressure drop. This induces a higher ratio of heat transfer to pressure drop for the DD-HX [59].

- Reynolds number is a dimensionless number which is defined by the ratio of the inertial forces to viscous forces in a fluid flow
- Nusselt number is also a dimensionless number which is defined by the ratio of the convective to conductive heat transfer across a surface

Most of the DD-HX research and development work conducted over the past years were focused on two main theories, developed by Slipcevic [56] and Donohue [55]. Both Slipcevic and Donohue developed methods of determining the overall heat transfer coefficient (HTC). Due to the complexity of the flow inside the DD-HX, the proposed method to calculate the overall heat transfer coefficient consisted in dividing the DD-HX into three zones and calculating the heat transfer coefficient in each of the zones separately. The three zones are illustrated in Figure 2.9 and are labelled 1 to 3: the first zone is located in the ring opening, the second zone is between the disk and the shell inner wall, and the third zone is located in the crossflow between two consecutive disk and doughnut baffle.

Slipcevic DD-HX Model

To achieve an effective model of a DD-HX, Splicevic [56] suggested the following design guidelines:

1- The spacing between the baffle disk and doughnut must be within 20 to 45% of the inner shell diameter, where less than 15% is not recommended
2- Higher heat transfer occurs in the cross flow region (normal to the tubes), therefore it is advisable to increase the flow velocity for higher heat transfer in the flow parallel to the tubes; this is done by placing the

baffles in a way to increase the velocity of the longitudinal flow more than that of the cross flow.

3- It is also advisable to make the area inside the ring S_{ko} the same as the annular area S_{ka} (between disk and shell):

$$S_{ko} = \frac{\pi}{4} D_o^2 \tag{2.7}$$

$$S_{ka} = \frac{\pi}{4} (D_s^2 - D_a^2) \tag{2.8}$$

where D_s is the inside shell diameter, D_o is the opening ring diameter and D_a is the disk diameter (see Figure 2.9)

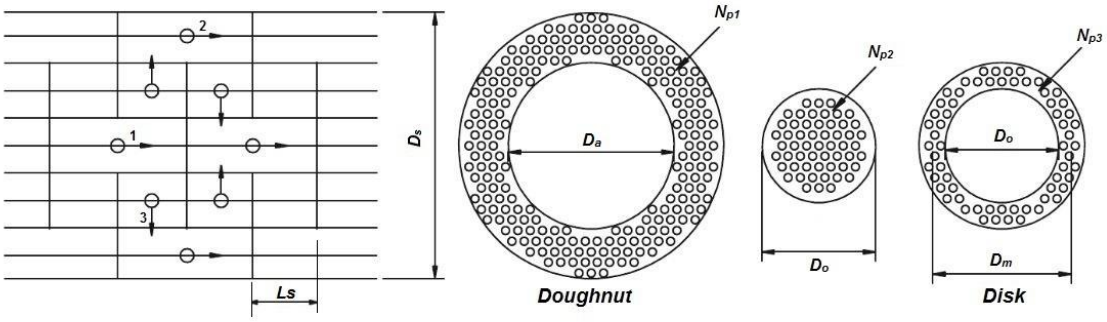

Figure 2.9 – Schematic of the different zones within the DD-HX and their dimensions.

In order to satisfy the 3rd design guideline, S_{ko} must be equal to S_{ka}, therefore:

$$D_s^2 = D_o^2 + D_a^2 \tag{2.9}$$

As mentioned before, there are two types of flow that exist inside the DD-HX; longitudinal and cross flow. The heat transfer coefficients will be calculated separately through the following steps:

Step 1: Finding the flow area in the longitudinal flow zones of the heat exchanger (noting that the flow area is the area excluding the pipes or tubes within the HX)

- Zone 1 (ring opening):

$$S_o = \frac{\pi}{4}\left(D_o^2 - N_{p2} d^2\right) \tag{2.10}$$

where d is the pipe diameter, S_o is the flow area and N_{p2} the number of pipes or tubes in the ring opening.

- Zone 2 (annulus between disk and shell wall):

$$S_a = \frac{\pi}{4}\left(D_s^2 - D_a^2 - N_{p1}d^2\right) \tag{2.11}$$

where S_a is the flow area and N_{p1} the number of tubes in the annulus region between disk and shell wall.

Step 2: Calculating the effective flow area of the cross flow region S_c

- Zone 3 (Cross-flow normal to the pipes):

$$S_c = L_s \times \sum x \tag{2.12}$$

where L_s (Figure 2.9) is the distance between two consecutive baffles and $\sum x$ is the sum of the clear distances between the neighbouring tubes to the mean diameter D_m (Figure 2.9 & Figure 2.10). This can be calculated from the engineering drawing or by using computational methods:

$$D_m = \frac{1}{2}(D_o + D_a) \tag{2.13}$$

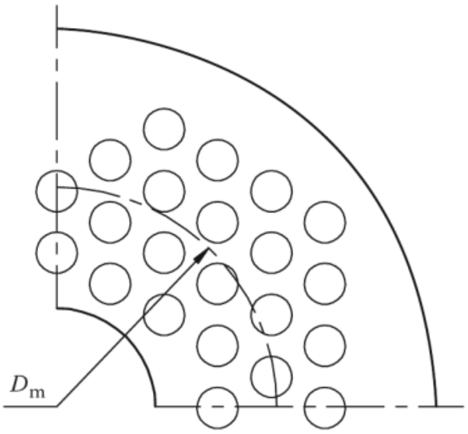

Figure 2.10 – Mean diameter to find the cross flow area [60]**.**

Step 3: Calculating the hydraulic diameter for the longitudinal flow based on the flow area inside the ring opening (S_o) and the annulus (S_a):

$$D_h = \frac{4S}{P_{wetted}} \tag{2.14}$$

Equation (2.14) represents the general formula for the hydraulic diameter where S is the flow area and P_{wetted} is the wetted perimeter.

The hydraulic diameter is essential to calculate the Reynolds number (Re), which later will be used to find the heat transfer within the heat exchanger:

$$D_{ho} = \frac{4S_o}{\pi(N_{p2}d + D_0)} \tag{2.15}$$

$$D_{ha} = \frac{4S_a}{\pi(N_{p1}d + D_a + D_s)} \tag{2.16}$$

Step 4: The heat transfer coefficients h_a and h_o are calculated for the longitudinal flow based on Hausen’s equation [61]:

$$Nu_a = 0.024Re_a^{0.8}Pr^{0.33}\left(\frac{\mu_f}{\mu_s}\right)^{0.14} \tag{2.17}$$

$$Nu_o = 0.024Re_o^{0.8}Pr^{0.33}\left(\frac{\mu_f}{\mu_s}\right)^{0.14} \tag{2.18}$$

where Nu is the Nusselt number, μ_f and μ_s are the viscosity at fluid mean temperature and tube surface temperature, respectively:

$$Nu_a = \frac{h_a D_{ha}}{k} \tag{2.19}$$

$$Nu_o = \frac{h_o D_{ho}}{k} \tag{2.20}$$

$$Re_a = \frac{U_a D_{ha}}{\mu_f} \tag{2.21}$$

$$Re_o = \frac{U_o D_{ho}}{\mu_f} \tag{2.22}$$

U_a and U_o represent the velocity of the fluid in the annular and opening ring region, respectively.

Step 5: Calculate the heat transfer coefficient h_c for the cross flow region

The heat transfer coefficient for the cross flow across the tube bundles for turbulent flow is calculated from McAdams [62]:

$$Nu_c = E \times Re_c^{0.6} \times Pr^{0.33} \times \left(\frac{T_f}{T_s}\right)^{0.14} \tag{2.23}$$

E is a constant whose value depends on the tube arrangement. It has a value of 0.33 for the staggered tube arrangement and 0.26 for the in-line tube arrangement.

The Re_c for the cross flow region is based on U_c, which is the velocity of the fluid in the cross flow region S_c:

$$Re_c = \frac{U_c d}{\mu_f} \tag{2.24}$$

Once the individual heat transfer coefficients of the three different zones are calculated, the weighted mean average HTC could be calculated. Slipcevic [56] recommends calculating the HTC for the individual tube row based on the corresponding flow cross section area. Alternatively, the crosssectional areas of the longitudinal and cross flow are calculated as follows:

$$A_a = \pi d L N_{p1} \tag{2.25}$$

$$A_o = \pi d L N_{p2} \tag{2.26}$$

$$A_c = \pi d L N_{p3} \tag{2.27}$$

where L is the tube length and:

$$N_{p3} = N_t - \left(N_{p1} + N_{p2}\right) \tag{2.28}$$

$$A_t = A_a + A_o + A_c \tag{2.29}$$

$$A_t = \pi \times d \times N_t \times L \tag{2.30}$$

Step 7: Calculating the overall heat transfer coefficient h_t

The overall heat transfer coefficient is calculated based on the total heat transfer area A_t:

$$h_t = \frac{h_a A_a + h_o A_o + h_c A_c}{A_t} \tag{2.31}$$

The Disk and Doughnut HX system that will be investigated later in this project was designed by Econotherm (UK) Ltd., and can be seen in Figure 2.11.

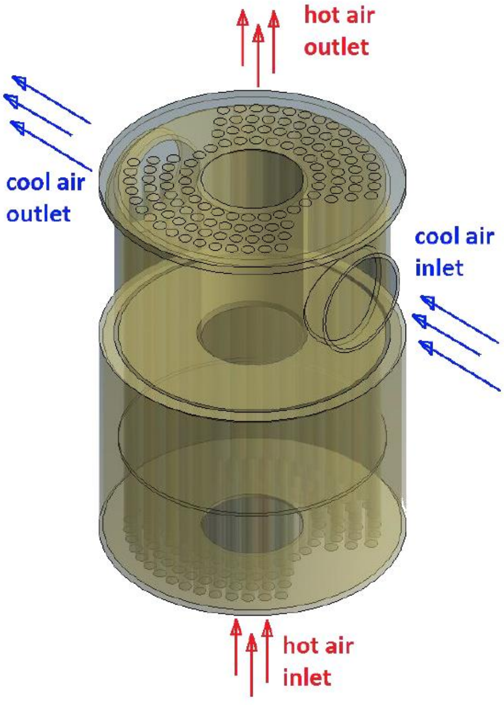

Figure 2.11 – Disk and Doughnut prototype designed by Econotherm (UK) Ltd. [9]

There are three key differences between Slipcevic's DD-HX geometry and the one investigated in this project. In Slipcevic's model, there are tubes located in the centre of the geometry through the ring hole and on the sides of the disk baffle, as can be seen in the schematic shown in Figure 2.12. In the HPHX under investigation, those are non-existent, and the reason for this difference is the use of thermosyphons as they must have contact with both a hot and a cold flow, and the contact with the cold flow is made in a ring-shaped space on the top of the heat exchanger (see Figure 2.12). A small spacing between the tubes and the disk baffle to allocate the tubes is also mentioned by Slipcevic, something that does not happen in the new geometry, where the thermosyphons are rigidly fixed to the heat exchanger.

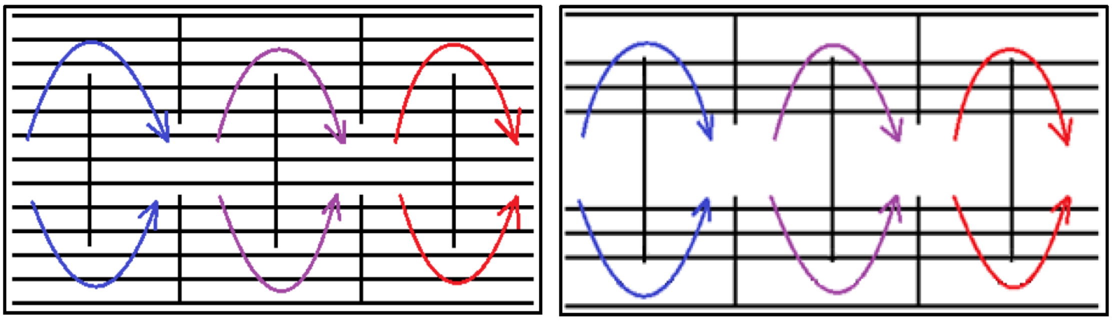

Figure 2.12 – Comparison between the model employed by Slipcevic (left) and the one studied in this project (right).

2.3. Heat pipe based heat exchanger (HPHX)

2.3.1. Heat pipe operation

Heat pipes are thermal devices that possess a low overall thermal resistance, hence transferring a large amount of heat with just a small temperature difference between the evaporator and condenser [63,64]. The heat is transferred through two-phase heat transfer mechanisms (evaporation-condensation) that occur inside the device [65]. The heat pipe technology has been widely used in heat exchangers, electronic cooling components such as in laptops and turbine rotor blades, it also recently found its application in thermal energy storage systems [66,67]. Heat pipes are called superconductors as they can transport heat of several orders of magnitude higher than that in a similar size solid rod in pure conduction. A heat pipe is an evacuated metallic tube that contains a small amount of liquid known as the working fluid. The device wall or shell is made out of either copper, stainless steel, aluminium, nickel or titanium and the working fluid can be water, ethanol, toluene, acetone, helium, hydrogen or sodium. The choice of the metal and the working fluid mainly depends on the compatibility between them and the desired operating temperature of the application. For a durable design, it is very important to match the fluid with a compatible material on one hand and keeping the saturation pressure between 0.1 and 20 bar [68] to avoid the possibility of over-pressurisation and rupture when putting the thermosyphon in a vacuum condition [69].

A heat pipe consists of three sections: evaporator, adiabatic and condenser (Figure 2.13).

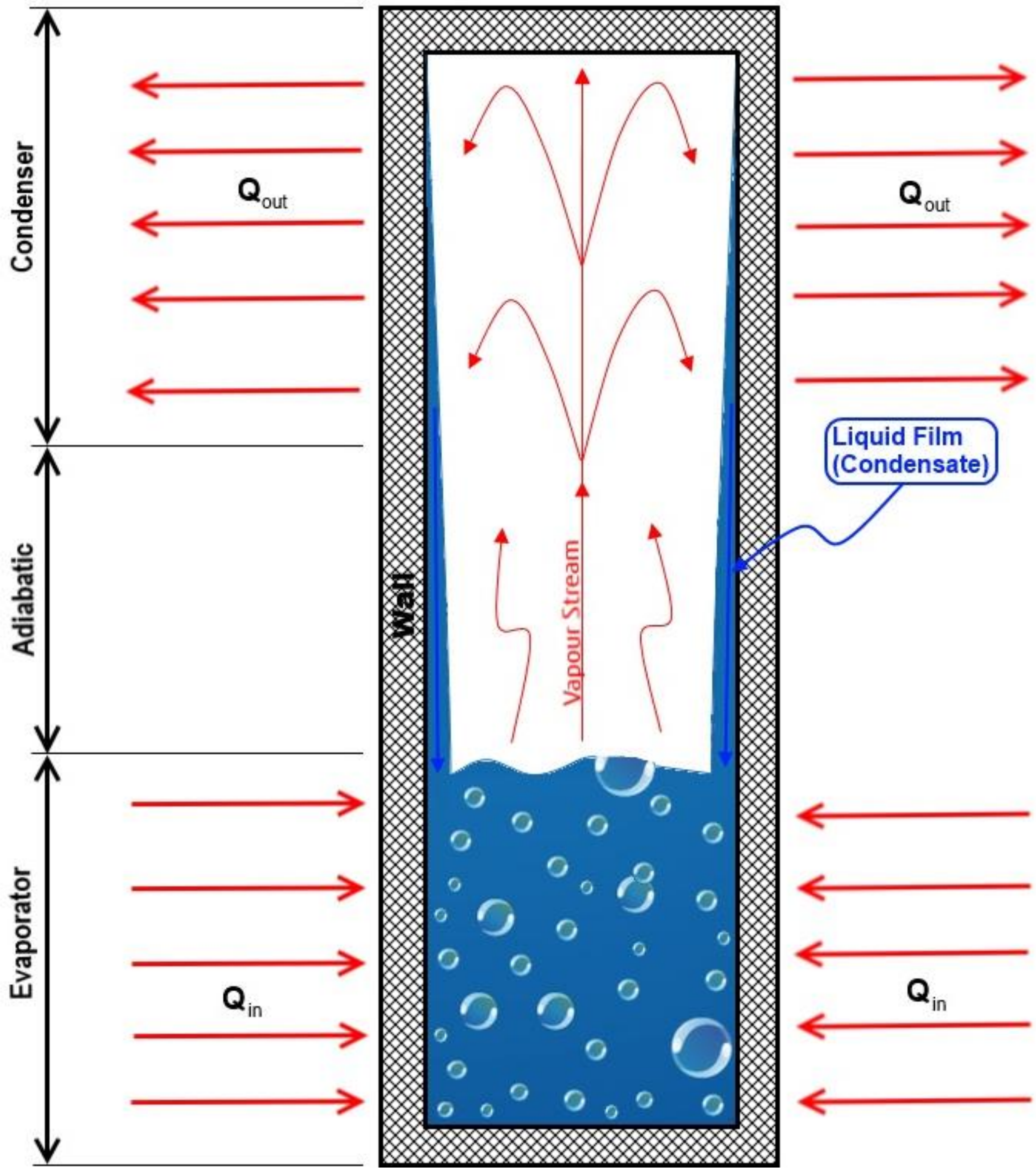

Figure 2.13 – Schematic diagram of a thermosyphon.

The evaporator is the lower end section where the working fluid is located. Heat is added (Q_{in}) to the evaporator section of the tube through a heat source where the heat is transferred by conduction through the heat pipe wall. Heat is then transferred by convection from the inside tube wall to the working fluid where the fluid absorbs the latent heat. When the temperature of the fluid exceeds its saturation temperature at a given pressure, the working fluid evaporates and vapour travels through the adiabatic section to the condenser. In the adiabatic section, no heat is added or removed ($Q = 0$); therefore, a unique feature of the heat pipe is that the evaporator and condenser sections can be separated by a large distance [7] through modifying the length of the adiabatic section. When the vapour reaches the other end of the tube, i.e. condenser, the vapour gets in contact with the inner condenser tube wall which is at a lower temperature. The vapour gives off its latent heat (Q_{out}) that was absorbed at the evaporator, then condenses forming a liquid film and returns back to the evaporator by either gravity in case of a wickless heat pipe or through capillary forces that exist inside the wicks in the case of wicked heat pipes [70]. The liquid then refills the evaporator section, hence completing the cycle. Depending on the application, the size of the heat pipe can range from a cross-sectional dimension of about 10 µm to a large scale length of the order of 100 m.

The heat exchanger is this project is equipped with a wickless heat pipe type. A wickless heat pipe, also known as two-phase closed thermosyphon (TPCT) or gravity assisted heat pipe, relies on gravity to return the liquid condensate from the condenser to the evaporator, while wicked heat pipes rely on the internal wicks to drive back the liquid condensate. A wickless heat pipe operates only when the condenser is located above the evaporator section, therefore the heat flows only in an upward direction making heat pipes behave like thermal diodes. The light weight, low resistance, simplicity and passive operation of the thermosyphon makes it suitable for a wide range of applications and operating conditions.

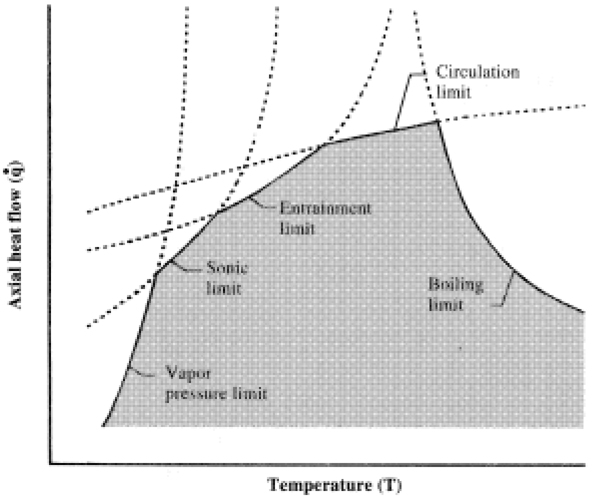

Figure 2.14 – Heat pipe operational envelope limits [71]**.**

Furthermore, thermosyphons have various operational limitations which should be taken care of in the design stage to avoid failure of the pipe. Such limitations are listed below and are shown in Figure 2.14:

4- *Viscous Limit* (or Vapour Pressure limit): This limit is frequent upon start-up; the viscous force of the fluid prevents the vapour flow from moving from the evaporator to the condenser. It is caused by having a small temperature difference between both ends, creating a low vapour pressure difference. In the worst case scenario, the vapour will not move to the condenser to complete the thermodynamic cycle.

5- *Sonic Limit*: Occurs when the vapour velocity reaches a sonic speed at the evaporator and any increase in pressure difference will not cause acceleration of the flow, effectively deactivating the thermosyphon.

6- *Entrainment Limit*: Friction between the working fluid in liquid state and vapour travelling in the opposite direction can block the thermosyphon, causing entrainment of the liquid by the vapour. Entrainment will cause a starvation of the fluid flowing from the condenser and eventual “dry out” of the evaporator [71].

7- *Boiling Limit*: Related to the rate at which the working fluid is evaporated. This limit occurs too fast and it will not give time for the cold fluid to condense, causing a dry out on the pipe.

8- *Circulation limit*: Also called capillary limit, related to wicked heat pipes where there is not enough pressure in the wick to push the liquid back to the evaporator, which causes dry out of the evaporator [72].

2.3.2. Heat exchangers equipped with TPCT

Due to the simplicity of heat pipes in terms of manufacturing and their passive operation, the TPCT has been recently integrated in heat exchangers creating a combined heat-pipe-based heat exchanger (HPHX) system which can be used in different branches of industry including power, metallurgy, oil refining and waste heat recovery technology [73,74]. Such applications include heating, ventilation and air conditioning (HVAC), waste heat recovery from exhaust gases, steam condensers, high temperature nuclear reactor technology, CPU cooling systems in laptops and many more.

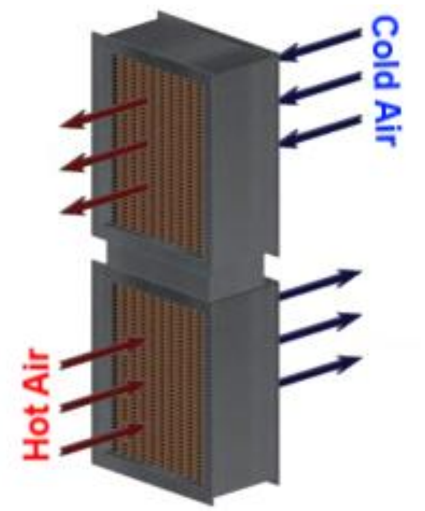

Figure 2.15 – Illustration of a typical HPHX [5].

Figure 2.15 is an example of a typical HPHX system. The heat exchanger in Figure 2.15 is a cross-flow heat-pipe-based HX where a number of heat pipes are mounted vertically and could be in a staggered or an inline configuration. As it can be seen from the figure, the hot fluid is flowing over the evaporator section and the cold fluid over the condenser section of the TPCTs, and therefore heat will only be transferred through the evaporation-condensation mechanism inside the heat pipe as the two streams are separated. In this case, the fluid flowing across the pipes can be for example air, water, oil, etc. The use of fins around the pipes is a way to increase the heat transfer area of the heat pipe and, therefore, increasing the overall thermal performance of the heat exchanger system. However, the use of fins to increase the surface area is limited as the fin efficiency decreases with length [7].

The use of thermosyphons in HXs has many advantages over conventional HXs. Based on the literature, the following advantages were drawn:

- No additional power is required as long as there is a hot stream to be absorbed by the evaporator [75]
- System is easily built and taken apart for cleaning or in case a pipe has failed [76]
- Pipes are free to expand and contract without applying stress on the housing [73]
- Isothermal operation of the pipes prevents cold and hot spots in the system, which can lead to system failure [77]
- High reliability as the failure of one heat pipe has a minimal effect on the thermal performance of the HX, due to the high number of heat pipes within the system [7,65]
- High heat recovery, effectiveness and compactness [78]
- The heat transfer area on the hot and cold streams can be modified by modifying the evaporator or condenser length to achieve a desired heat extraction
- Potential of increasing the number of heat pipes perpendicular to the flow direction [6]
- No cross-contamination between the hot and cold streams, as the streams are separated by a plate [79]

Due to new pollution and emission reduction policies, for efficient air conditioning , waste heat recovery, energy storage and many other heat transfer applications at various scales, including cost and material reduction, HPHX systems have been so far the best design solution to meet the requirements of all heat transfer systems [73].

Under a medium operating condition of temperatures below 300°C, Lukitobudi et al. [79] carried out an experimental investigation of an air-to-air thermosyphon-based heat exchanger (TSHX). The counter flow TSHX was constructed to contain 24 thermosyphons, distributed in 6 rows arranged in a staggered configuration. Considering the fluid high merit number, suitability with medium temperature, being environmental friendly and widely available, water was chosen as the working fluid. The thermosyphons were charged with water, filling 60% of the evaporator’s volume. Three different thermosyphon types were manufactured and equipped within the heat exchanger: bare copper, finned copper and finned steel tubes. The finned copper thermosyphon-based heat exchanger achieved the best performance; however there is a chance of exceeding the safe working pressure for the current operating condition (300°C). Therefore the steel finned was preferred as it was rigid and recovered sufficient thermal energy. The bare copper thermosyphons could be an alternative in case of searching for low manufacturing and maintenance cost, although providing a low heat transfer. The application of such TSHXs is to recover the waste thermal energy from the flue gas of the oven to heat up the proofing oven in bakeries.

Jouhara et al. [80] experimentally investigated the effect of changing the evaporator air inlet temperature and inclination angle on the thermal performance of a HPHX that is used in energy efficient air handling units. The investigated HPHX was cross-flow air-to-air, which consists of 9 finned thermosyphons in an inline configuration filled with water as the working fluid. The experimental investigation showed that significant energy savings can be achieved when using thermosyphons within the heat exchanger to transfer energy from two air streams at different air inlet temperatures.

Danielewicz et al. [6] has experimentally investigated the effect of changing the evaporator and condenser mass flow rate on the thermal performance of an air-to-air heat-pipe-based HX in a cross-flow pattern. The HX consisted of 100 finned thermosyphons placed vertically, arranged in 10 rows, with each row containing 10 carbon steel heat pipes of length 2200 mm and an outer diameter of 27mm. The working fluid used for this investigation was methanol. The experimental results were then used to validate a developed numerical tool through the ε-NTU (Effectiveness Number of Transfer Units) method. This method is used to predict the overall heat transfer coefficient (HTC), effectiveness, pressure drop and heat extraction duty for a given crossflow gas-to-gas HPHX. The investigation reported an increase of the heat recovery rate the more the flow progressed through the HX. It was also observed that the effectiveness increased as the ratio of both mass flow rates increased. The developed prediction model can be used for the future design of a typical cross-flow air-to-air heat pipe based HX system.

Noie et al. [69] carried out an experimental and theoretical investigation of an air-to-air cross flow HPHX that has application in operating theatres in hospitals. Based on the experimental results obtained, Noie et al. [69] proposed the following points that would play an important role in improving the efficiency and effectiveness of any HPHX system:

- Installing fins around the heat pipes
- Increasing the number of heat pipe rows
- Minimising heat loss
- Most appropriate method of charging the heat pipes to prevent accumulation of non-condensable gases
- Perfect sealing of the heat pipe to prevent loss of vacuum

2.4. Research gap

In this project, ANSYS Fluent was used as a tool to model a multi-pass type heat exchanger used in waste heat recovery applications. The multi-pass was installed on the shell-side on both the evaporator and condenser section with a staggered and an in-line tube arrangement, respectively. The heat exchanger followed the concept of a shell-and-tube heat exchanger of a smaller scale Disk-and-Doughnut baffle type STHX. A schematic is shown in Figure 2.16, where the heat exchanger under investigation can be observed if one symmetrical part is taken out. However, wickless heat pipes were used instead of the tubes. Therefore, the thermal energy was transported within the heat pipe through evaporation-condensation phenomena. The integration of the thermosyphon device in a multi-pass heat exchanger system is a recent technology. Therefore the theoretical, numerical and experimental investigations of such systems covered in this thesis is a step forward in expanding the knowledge of such systems in the heat transfer field and highlighting the advantages of such technologies.

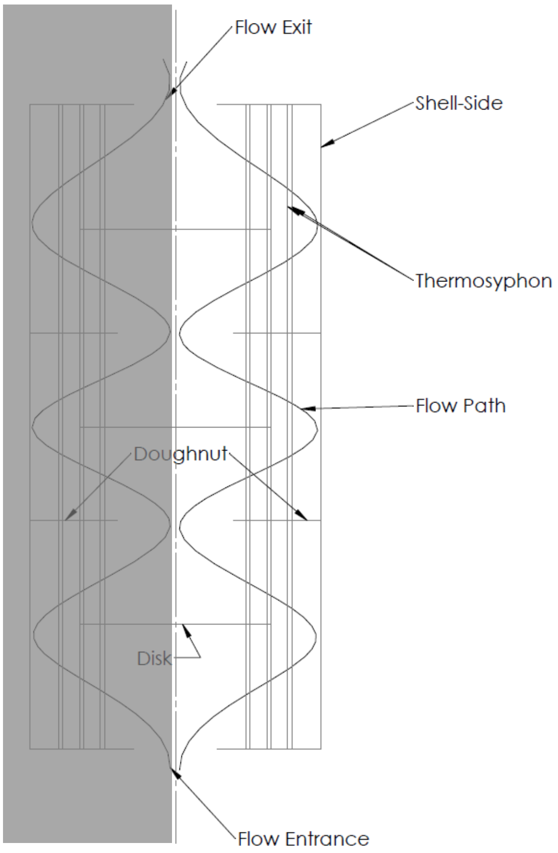

Figure 2.16 – The original concept of the investigated TSHX.

The heat exchanger was theoretically and numerically modelled using the electrical resistance approach and ANSYS Fluent, respectively. The fluid and thermal behaviour within the shell-side was theoretically modelled to completely understand the various heat transfer phenomena before validating the model by carrying out experimental testing. Two-different multi-pass configurations were chosen to carry out the validation. The more passes, the bigger the size of the device and the higher the pressure drop, which was a limitation of the design. In summary, the project used a validated CFD tool to model the shell-side convective heat transfer on the evaporator and condenser sides of a multi-pass heat-pipe-based heat exchanger. The successful validated CFD model is a step forward in the simulation of heat exchangers equipped with thermosyphons to model the shell-side behaviour. This can also be taken as an initial step to model the fouling phenomenon as it is a major industrial problem encountered in various types of heat exchangers.

Chapter 3. METHODOLOGY

The current chapter presents all the methodologies that were followed throughout the project. This chapter include theoretical, numerical and experimental methodologies of the multi-pass TSHX. The theoretical methodology illustrates the modelling procedure that was conducted at each stage of the heat exchanger, this includes justifications of the heat transfer correlations used. Consequently, the numerical methodology presents a detailed step by step outlining the various stages that were followed while using ANSYS Fluent as a numerical tool. The steps include sketching the model, grid analysis, boundary conditions and results. Finally a methodology of the experimental work was explained, stating all the various equipment used for the test rig. In addition, detailing the running procedure at different inlet conditions.

3.1. Theoretical modelling

3.1.1. Introduction

The thermosyphon based heat exchanger (TSHX) was designed in a 3D CAD software package (SolidWorks) where the design idea is adopted from the configuration of an existing Disk-and-Doughnut baffle arrangement TSHX designed by Econotherm (UK) Ltd. [9], a company that specialises in the design and manufacture of heat exchangers that use the heat pipe technology for waste heat recovery applications. As mentioned in the previous chapter, the integration of heat pipes within heat exchangers increases the overall performance of the system by transporting a large amount of heat through a small cross-sectional area. The new design is a smaller version of the existing design which is currently on the market. The design of the system relies on providing an easy access to modify the test rig by increasing the number of fluid passes on the evaporator section. However, the size of the heat exchanger has restricted the maximum number of fluid passes and thermosyphons; for manufacturing and operational cost limitations, a maximum of three passes could be installed on the designed heat exchanger with six thermosyphons arranged vertically in two rows of three thermosyphons each. The six thermosyphons are arranged in a staggered arrangement on the evaporator side and an in-line arrangement on the condenser side.

Figure 3.1 shows the heat exchanger unit under investigation. The TSHX was 2 m in height and each air pass covered 600 mm of the total length of the thermosyphons. A maximum of three air passes could be installed on the shell-side of the heat exchanger, giving a total length of 1.8 m for the evaporator and 200 mm for the condenser section. The same amount of working fluid (water) was injected into each thermosyphon during the charging process, filling each thermosyphon to a height of 600 mm corresponding to 250ml of water. Three different configurations of the test unit were investigated as follows:

- Case 1: One air-pass (cross-flow)
- Case 2: Two air-passes (multi-pass)
- Case 3: Three air-passes (multi-pass)

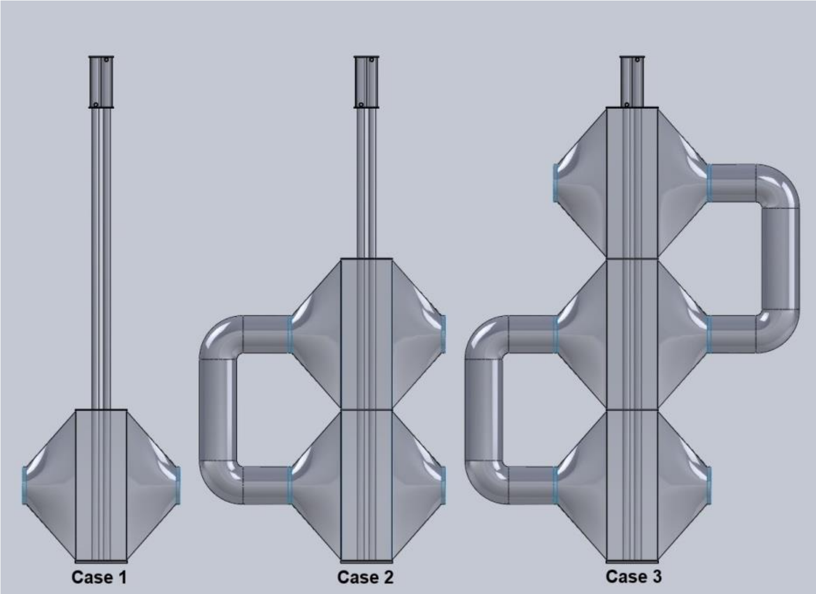

Figure 3.1 – SolidWorks drawing of the three tested models.

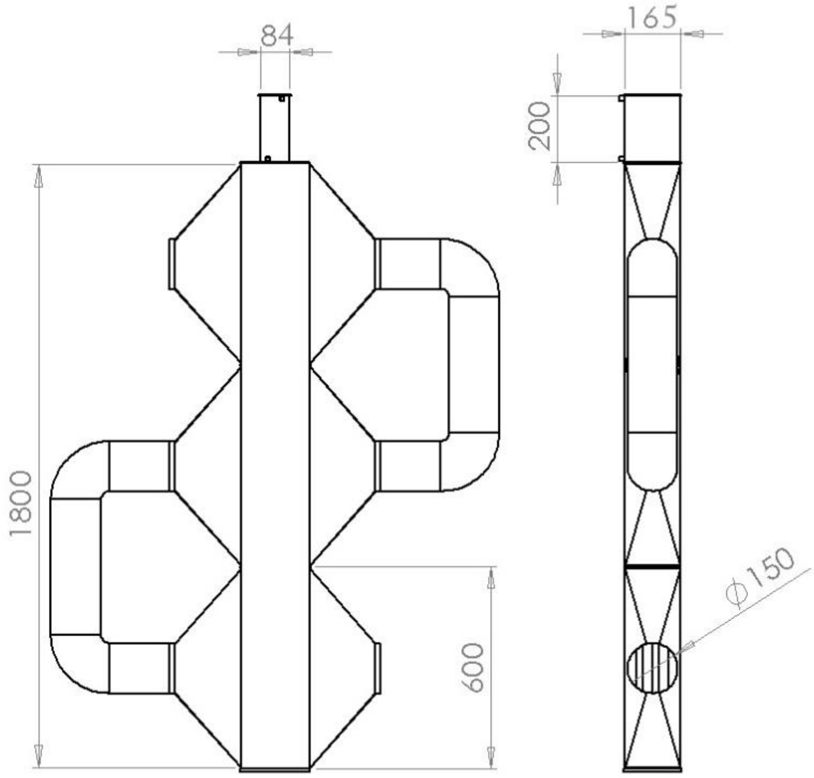

Figure 3.2 – TSHX important dimensions (in mm).

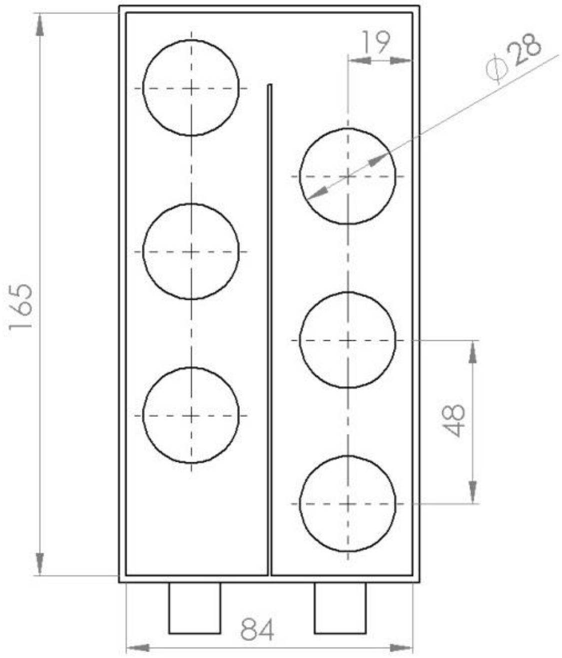

Figure 3.3 – Condenser top view dimensions (in mm).

The total height of the TSHX is 2 m as shown in Figure 3.2. Each pass covers 600 mm of the 6 TPs, giving each case a different evaporator length, 600, 1200 and 1800mm for cases 1, 2 and 3, respectively. The condenser length was kept fixed at a height of 200 mm, where the cooling medium (water) flows in a U-shaped passage (Figure 3.4) for all the three cases. The six thermosyphons have the same length as the heat exchanger, with an outer diameter of 28 mm and a wall thickness of 2.5 mm. Various researchers conducted experimental work on thermosyphons, this included different shell and working fluid combinations. Namely, carbon steel and methanol, steel and water, carbon steel and Dowtherm [6,75,81,82,76], which showed good compatibility. Though, carbon steel and water compatibility was not covered in the literature. The shell side wall was taken as adiabatic as the entire TSHX was well-insulated during the experiments. The modelling was carried out at different mass flow rates and inlet temperatures on the exhaust side. The inlet conditions were chosen based on the available equipment such as heater and fan, to build the test rig in order to carry out the experimental validation which will be covered later in the thesis. On the condenser side, the inlet conditions were kept the same including both inlet mass flow rate and temperature. The inlet conditions on both evaporator and condenser are represented in Table 3.1.

Table 3.1 – Inlet conditions on both evaporator and condenser.

	Evaporator (air)	**Condenser (water)**
Temperature (°C)	100:50:250	15
Mass flow rate (kg/s)	0.05:0.03:0.14	0.08

3.1.2. Thermal resistance analogy

In general, the thermal network consists of coupled thermal elements, each of which is characterised by a thermal resistance and a thermal capacitance. In systems involving a constant thermal conductivity and a negligible internal heat generation, steady state conditions can be considered. In this case, each thermal element can be reduced to a thermal resistance [83]. The thermal resistance network approach is an analogy that exists between the flow of electrical current and the thermal resistance which can be represented by the ratio of the driving potential (temperature difference) to the transfer rate between two points separated by a distance L_e. Equation (3.1) shows the thermal resistance which is derived from Fourier's law for one dimensional thermal conduction through a homogeneous material.

$$q = kA\frac{|T_1 - T_2|}{L_e} = \frac{|\Delta T|}{L_e/kA} \therefore R = \frac{L_e}{kA} = \frac{|\Delta T|}{q} \tag{3.1}$$

where L_e is the effective length, q represents the heat transfer rate, k is the thermal conductivity, A is the cross-sectional area of the material, R is the thermal resistance and ΔT is the temperature difference.

This method divides the TSHX system into different components where the various heat transfer modes can be applied, namely conduction, convection, condensation and boiling heat transfer. Depending on what mode of heat transfer is taking place in various components of the heat exchanger, the value of q in equation (3.1) is calculated accordingly based on heat transfer correlations chosen from the literature. The TSHX under investigation consists of several thermal resistances compared to a conventional heat exchanger. This is due to the integration of thermosyphons within the heat exchanger design, which creates extra resistances due to the phase change mechanisms inside the thermosyphons. However, adding more thermal resistances does not necessarily induce a higher overall resistance, though, it is the way that those thermal resistances are arranged within the thermal network that matter. In the case of parallel resistances, the overall resistance will be lower. The integration of thermosyphons within the heat exchanger under investigation have created extra thermal resistances acting in parallel mode relative to the separation plate between the two fluid streams, hence reducing the overall thermal resistance which is an essential reason to introduce the heat pipe technology in heat exchangers. The thermal network modelling approach was applied in order to evaluate the performance of the whole TSHX and has previously provided satisfactory results to many researchers [84,85].

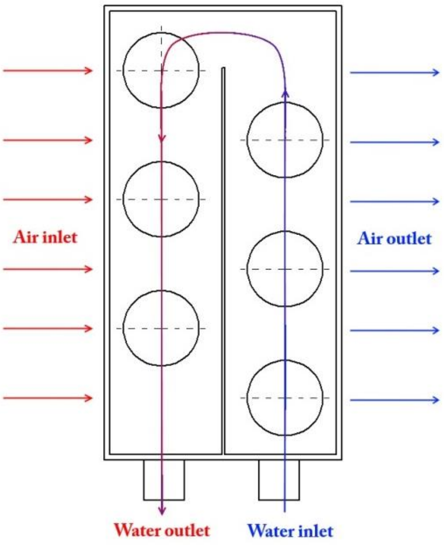

Figure 3.4 – Flow pattern in the condenser.

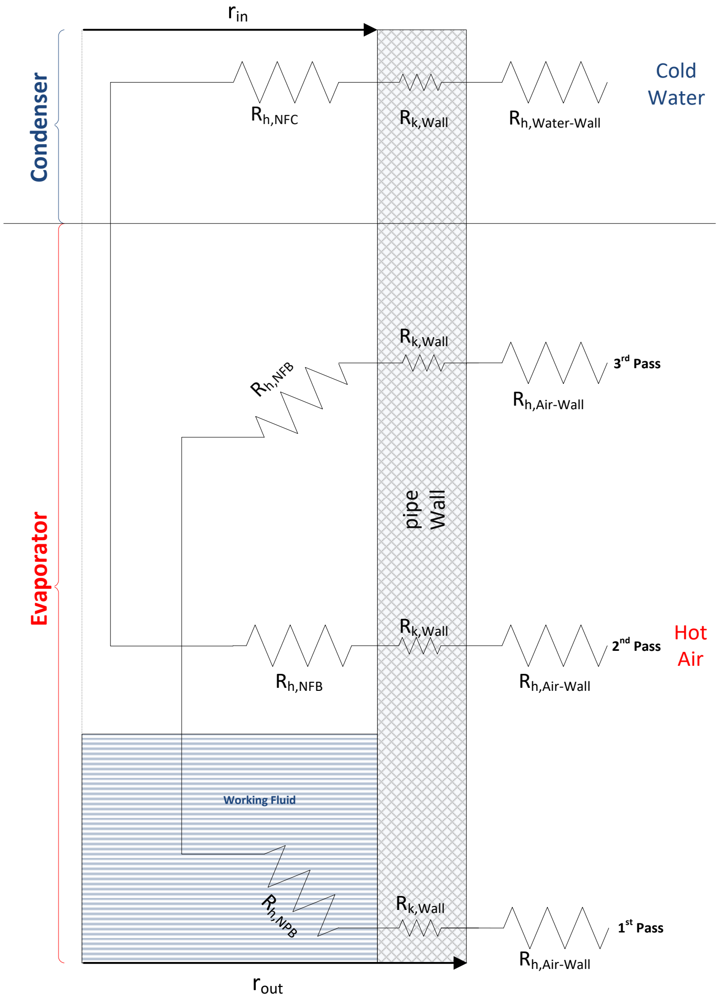

Figure 3.5 – Resistance network, Case 3.

Convective heat transfer coefficient (Air-Wall)

The major contributors for the overall thermal resistance within the TSHX are the convective resistances. Axial conduction and vapour pressure resistances were ignored during the analysis because of their negligible value. The thermal resistance of the entire TSHX system is schematically outlined in Figure 3.5 and Figure 3.7 for the three multi-pass configurations, where r_{in} and r_{out} represent the inner and outer radius of the thermosyphon, respectively. As hot air enters the heat exchanger, heat will be transferred by convection to the pipe's outer surface in the first air pass. The same happens with the second and third air passes. In each air pass and as shown in Figure 3.4 and Figure 3.6, the air crosses two rows of three thermosyphons each, in a staggered arrangement (Figure 3.6). The convective contact area A_e at the evaporator is the same for each air pass due to the same height of each pass (0.6m).

In order to calculate the average heat transfer coefficient (HTC) for the entire tube bank on the evaporator side, the following correlation was proposed by Zukauskas [86] for external flow around tube banks of less than 20, which is used to calculate the Nusselt number:

$$Nu = C_1 \times C_2 \times \left(Re_{D,max}\right)^m \times Pr^{0.36} \times \left(\frac{Pr}{Pr_w}\right)^{1/4} \tag{3.2}$$

In equation (3.2), $Re_{D,max}$ is the maximum Reynolds number which occurs at the minimum area (A_{min}) where the velocity is maximum (U_{max}). C_1 and m are values dependent of the distance between the tube bank and, therefore, dependent on the maximum Reynolds number (Table 3.2). The subscript w represents a property at the wall.

The minimum area is located in the vicinity of the tube bank. Both $Re_{D,max}$ and U_{max} were calculated through equation (3.3):

$$Re_{D,max} = \frac{\rho_{air} U_{max} D_h}{\mu_{air}} \quad and \quad U_{max} = \frac{\dot{m}_{air}}{\rho_{air} A_{min}} \tag{3.3}$$

where $\dot{m}_{air}$ is the mass flow rate of the air at each pass inlet, D_h is the hydraulic diameter of the air inlet, μ_{air} is the air dynamic viscosity and ρ_{air} is the air density.

All the properties including Prandtl number, dynamic viscosity and density are evaluated at the film temperature.

Table 3.2 – Constants for Equation (3.2) for various Re_{max} [86].

Configuration	Re_{max}	C_1	m
Staggered	$10 — 10^2$	0.90	0.40
Staggered	$10^2 — 10^3$	Approximated as a single (isolated) cylinder	
Staggered ($S_T/S_L < 2$)	$10^3 — 2 \times 10^5$	$0.35 \times \left(\frac{S_T}{S_L}\right)^{1/5}$	0.60
Staggered ($S_T/S_L > 2$)	$10^3 — 2 \times 10^5$	0.40	0.60
Staggered	$2 \times 10^5 — 2 \times 10^6$	0.022	0.84

C_2 is a correction factor to be used for tube banks (N_L) of 20 or less. The TSHX under investigation consists of 6 thermosyphons in a staggered arrangement; therefore, a corresponding correction factor value of 0.95 was selected as shown in Table 3.3.

Table 3.3 – Corresponding correction factor C_2 for different number of tubes (staggered) [86].

N_L	1	2	3	4	5	6	7	8	9
C_2	0.68	0.75	0.83	0.89	0.92	0.95	0.97	0.98	0.99

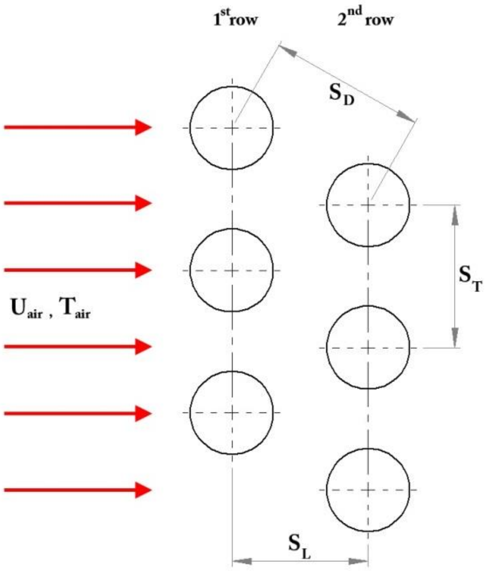

Figure 3.6 – Flow across the tube bank on the evaporator section (staggered).

The resistance to convection heat transfer between the shell side fluid (air or water) and the pipe outer surface is listed in Table 3.6: equations (3.8) and (3.13).

Convective heat transfer coefficient (Water-Wall)

On the condenser shell side, forced convection heat transfer occurs between the pipe outer surface and the heat sink where heat is recovered by water. Figure 3.4 shows the flow pattern of the water entering the condenser covering each thermosyphon one by one in an in-line configuration following a U-shaped passage. Therefore, the Zukauskas convection correlation for external flow was selected to calculate the Nusselt number for a single cylinder in a cross flow as it is applicable to this case.

$$Nu_D = C \times Re^m \times Pr^n \times \left(\frac{Pr}{Pr_w}\right)^{\frac{1}{4}} where, \qquad 0.7 \leq Pr \leq 500 \tag{3.4}$$

All the properties in equation (3.4) are evaluated at T_∞ except for Pr_w which should be evaluated at the wall temperature (T_w). The exponent n is a constant whose value depends on the Prandtl number (n=0.37 for $Pr \leq 10$). The values of constants C and m in equation (3.4) depend on the turbulence of the fluid between the tubes, whose values can be found in Table 3.4. Following the calculation of the shell side convective heat transfer coefficients, the resistance on the shell side evaporator and condenser was then calculated using equations (3.8) and (3.13), respectively.

Table 3.4 – Values for constants C and m at various Reynolds numbers.

Re	C	m
$1—40$	0.75	0.4
$40—1000$	0.51	0.5
$10^{-3}—2\times10^{5}$	0.26	0.6
$2\times10^{5}—10^{6}$	0.076	0.7

Conduction through the thermosyphon wall

As hot air enters the heat exchanger in a cross flow configuration across the thermosyphons, the heat is transferred radially by conduction through each thermosyphon's wall thickness where the resistance is calculated using equation (3.9). Axial conduction along the length of the thermosyphon was not taken into account due to its negligible value.

Pool boiling heat transfer

In case 1, where one air pass is applied across the six thermosyphons, a filling ratio of 100% is considered as the evaporator is completely full with water (Figure 3.7). Therefore, the only mode of heat transfer that exists inside the evaporator is nucleate pool boiling. However, there are several boiling heat transfer correlations which were found in the literature and used by many researchers [70,78]. Such correlations include Rohsenow [84], Cooper [87] and Imura [88] which have shown reasonable accuracy.

To achieve an accurate modelling of the TSHX, a careful selection of each mode of heat transfer correlation was necessary, more specifically the correlations used for pool boiling and film condensation. Therefore, an experimental evaluation of a single thermosyphon was carried out at different evaporator and condenser inlet conditions. The heat transfer coefficient of different pool boiling correlations at different evaporator heat input and condenser water inlet flow rates were modelled theoretically and compared to experimental boiling heat transfer coefficients. One pool boiling correlation was chosen to carry out the modelling of the TSHX based on the best agreement achieved with the experimental boiling HTC for a range of heat fluxes tested. Table 3.5 lists the most common boiling heat transfer correlations used in thermosyphons for validation.

Table 3.5 – Nucleate pool boiling heat transfer correlations.

Rohsenow [84]	$h_{nb} = \dfrac{q^{2/3}}{\dfrac{C_{sf} \times h_{fg}}{c_{p,f}} \times \left(\dfrac{L_B}{h_{fg} \times \mu_f}\right)^{0.33} \times pr^{1.7}}$ Where, $L_B = \left[\frac{\sigma}{g(\rho_f - \rho_g)}\right]^{1/2}$ is the bubble length scale	(3.5)
Cooper [87]	$h_{nb} = 55 \times pr^{0.12 - 0.4343 \times \ln(R_p)} \times (-\log_{10} P_r) \times M^{-0.5} \times q^{0.67}$	(3.6)
Imura et al. [70]	$h_{nb} = 0.32 \left(\dfrac{{\rho_f}^{0.65} \times {k_f}^{0.3} \times {c_{p,f}}^{0.7} \times g^{0.2}}{{\rho_g}^{0.25} \times {h_{fg}}^{0.4} \times {\mu_l}^{0.1}}\right) \times \left(\dfrac{P_{sat}}{P_{atm}}\right)^{0.3} \times q^{0.4}$	(3.7)

The subscripts l and g correspond respectively to the liquid and gas/vapour phases.

In the Rohsenow correlation, equation (3.5), the coefficient C_{sf} and exponent n both rely on the surface-liquid combination. Vachon et al. [89] suggested using $C_{sf} = 0.0147$ and $n = 1$ for a combination of water and polished copper. As mentioned before, the thermosyphons are made of carbon steel and filled with water, no value of C_{sf} was investigated by previous researchers for such surface-liquid combination whatsoever. Carrying out the experimental investigation of a single thermosyphon was beneficial to decide which pool boiling correlation performs accurately with such material and working fluid combination. In addition, a new value for C_{sf} was proposed which could be used in modelling thermosyphons with the same surface-liquid combination.

Referring to Cooper, equation (3.6):

$M = 18.02\ g/mol$, represents the molar mass of water

R_p was suggested by Cooper [90] to be set to $1\ \mu m$ for undefined surfaces

$P_r = \frac{P_{atm}}{P_{cr}}$ is the pressure ratio where $P_{cr} = 220.93\ bar$

Nucleate film boiling

In cases 2 and 3 (Figure 3.5 and Figure 3.7), the evaporator length was increased by 0.6 m in each case, keeping the same amount of working fluid in each thermosyphon. The filling ratios in cases 2 and 3 are therefore $1/2$ and $1/3$, respectively. An extra mode of convective heat transfer is considered within the thermosyphons in the 2nd and 3rd air passes which is in parallel with the pool boiling mode. This mode of heat transfer takes place through the liquid condensate film returning to the evaporator pool, and is referred to as nucleate film boiling (see equation (3.11)).

Table 3.6 – Thermal resistance correlations.

Resistance	**Heat transfer mode**	**Analytical/empirical**		**References**
$R_{h,Air-Wall}$	Air-Wall convection	$\frac{1}{h_{convection}A_e}$	(3.8)	[91]
$R_{k,Wall}$	Conduction across thermosyphon wall	$\frac{\ln\left(\frac{r_{out}}{r_{in}}\right)}{2\pi kL}$	(3.9)	[92]
$R_{h,NPB}$	Nucleate pool boiling (Rohsenow)	$\frac{\dot{q}}{A} = \mu\, h_{fg}\sqrt{\frac{g(\rho_L-\rho_v)}{\sigma}}\left(\frac{c_p\Delta T_b}{h_{fg}C_{sf}}\right)^{\frac{1}{3}} Pr^{-\frac{n}{3}}$	(3.10)	[93]
$R_{h,NFB}$	Nucleate film boiling	$\frac{\dot{q}}{A} = (1.155\times10^{-3})Nu_{\mu_f}^{0.33}Pr^{0.35}K_p^{0.7}\left(\frac{q_e l_m}{\rho_V h_{fg} v_l}\right)^{0.7}\frac{\Delta T_b k}{l_l}$	(3.11)	[94]
$R_{h,NFC}$	Film condensation	$h_m = 0.943\times\left(\frac{k_l^3\rho_L(\rho_L-\rho_V)gh_{fg}}{\mu_l\theta l}\right)^{1/4}$	(3.12)	[95]
$R_{h,Water-Wall}$	Water-Wall convection	$\frac{1}{h_{convection}A_c}$	(3.13)	[91]

Filmwise condensation

The vapour inside the thermosyphon travels vertically towards the condenser section where, upon coming into contact with the inner pipe cold surface, it condenses back to liquid, releasing its latent heat, which will be absorbed by water surrounding the six thermosyphons. This mode of heat transfer is essential for a thermosyphon to complete its thermodynamic cycle.

During the condensation process, vapour condenses on a cold surface in two different ways depending on whether it wets the surface or not. If the liquid condensate wets the surface, the liquid forms a continuous liquid film and this is referred to as filmwise condensation. If the liquid condensate does not wet the surface, this eventually forms droplets of water and this is referred to as dropwise condensation. Despite the higher heat transfer coefficient obtained from dropwise condensation, long term dropwise condensation is difficult to maintain. The reason is that the material requires a special type of surface finish to promote this mode of condensation heat transfer. Today, all surface conditions are designed to operate in filmwise condensation [96]. For this investigation, filmwise condensation was considered, where the area averaged version of Nusselt's theory was applied as it is very commonly used within the laminar regime for filmwise condensation on a vertical flat plate [97,95], equation (3.12).

Thermal resistance and conductivity, k

The thermal resistance in equation (3.14) is defined as the ratio of the temperature difference across a component i to the corresponding rate of heat transfer. The application of the approach would identify which component within the HX system restricts the majority of the heat transfer and the design could be revised.

$$R_i = \frac{\Delta T_i}{Q_i} \tag{3.14}$$

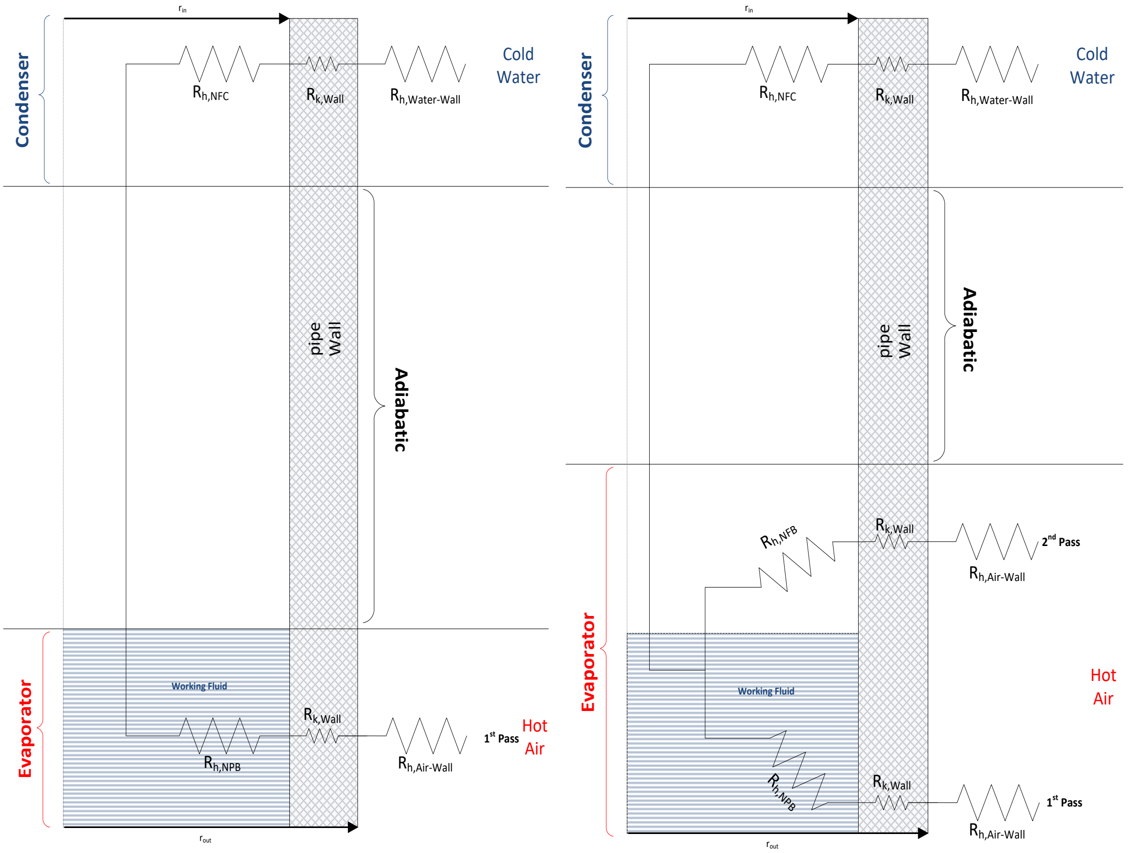

Figure 3.7 – Resistance network, Case 1 (left) and Case 2 (right).

In the first case and referring to Figure 3.7, the internal resistance of one thermosyphon is calculated by the following equation:

$$R_{TS} = \left(R_{k,Wall} + R_{h,NPB}\right)_{pass1} + \left(R_{h,NFC} + R_{k,Wall}\right)_{Condenser} \tag{3.15}$$

For the second and third cases, the internal resistance of one thermosyphon is presented in equations (3.16) and (3.17), respectively:

$$R_{TS} = \left(\left(\frac{1}{R_{k,Wall} + R_{h,NPB}}\right)_{pass1} + \left(\frac{1}{R_{k,Wall} + R_{h,NFB}}\right)_{pass2}\right)^{-1} + \left(R_{h,NFC} + R_{k,Wall}\right)_{Condenser} \tag{3.16}$$

$$R_{TS} = \left(\left(\frac{1}{R_{k,Wall} + R_{h,NPB}}\right)_{pass1} + \left(\frac{1}{R_{k,Wall} + R_{h,NFB}}\right)_{pass2} + \left(\frac{1}{R_{k,Wall} + R_{h,NFB}}\right)_{pass3}\right)^{-1} + \left(R_{h,NFC} + R_{k,Wall}\right)_{Condenser} \tag{3.17}$$

Assuming all the six thermosyphons have equal internal resistances, the above equations can be simplified as follows:

$$\frac{1}{R_{6TPs}} = \sum_{i=1}^{6} \frac{1}{R_i} \tag{3.18}$$

Adding more thermosyphons to the heat exchanger system will add extra resistances in a parallel configuration as can be seen from equation (3.19). Therefore, the internal and total resistance of the whole system will be reduced and more heat will be recovered,

$$R_{6TS} = \frac{R_{TS}}{6} \tag{3.19}$$

The total thermal resistance R_{Total} of the system is needed to calculate the overall heat transfer by adding the external convective heat transfer, giving a total thermal resistance for case 1 as follows:

$$R_{Total} = R_{6TS} + R_{h,Air,Wall} + R_{h,Water,Wall} \tag{3.20}$$

For the second and the third cases, the resistance of the convective heat transfer in the second and third pass from the air to the pipe outer wall will also be added.

The internal thermal resistance of a single thermosyphon (R_{TS}) is an essential parameter for the purpose of calculating the effective thermal conductivity of a thermosyphon. In the following chapter, the thermal conductivity will be calculated from equation (3.21) and used in ANSYS Fluent where it replaces the phase change heat transfer mechanisms inside the thermosyphon by pure conduction heat transfer,

$$R_{TS} = \frac{L}{kA_{TS}} \quad \therefore \quad k = \frac{L}{R_{TS}A_{TS}} \tag{3.21}$$

Equation (3.21) describes the parameters that relate the thermal conductivity k to the thermal resistance R_{TS}, where L is the length of the thermosyphon and A_{TS} is its cross-sectional area.

3.2. CFD modelling

The recent improvements in numerical techniques, more specifically related to the computational speed, has made Computational Fluid Dynamics (CFD) a quick and efficient tool to assess the fluid flow distribution, pressure drop and thermal analysis in various types of heat exchangers. This tool can be used to design heat exchangers from scratch or to suggest design modifications in the optimisation phase.

In this study, a solution methodology using ANSYS Fluent (version 16.2) as a commercial CFD package was chosen to carry out the numerical analysis. ANSYS Fluent focused mainly on analysing the thermal behaviour of the shell-side fluid, therefore computational heat transfer (CHT) or numerical heat transfer (NHT) is a more appropriate name for this analysis.

Following the theoretical modelling described in the previous chapter, ANSYS Fluent was used as a CFD solver to simulate the designed heat exchanger to obtain a good prediction of the shell-side thermo-fluid behaviour of the air and water within the evaporator and condenser sections, respectively. The prediction was based on obtaining a localised solution of variables including temperature, velocity and pressure, moreover an adequate visualisation of variable fields in the domain which cannot be achieved through experiments. In order to carry out a detailed CFD model, a number of simplifications of the real heat exchanger have to be made. Those simplifications can save a large amount of computing power, memory and time, while still keeping the most relevant aspects of the physics of the problem.

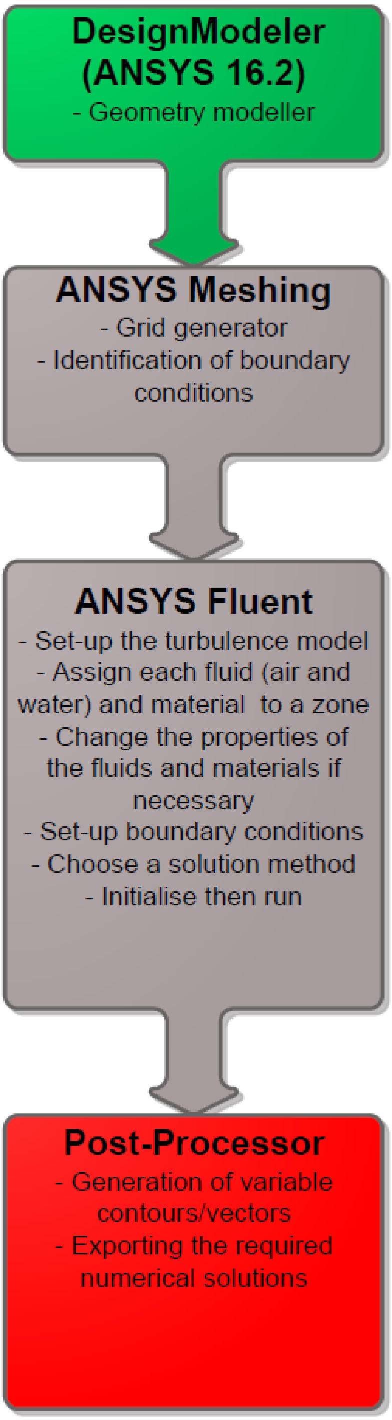

Figure 3.8 – Schematic of ANSYS Fluent solution process.

To simulate an industrial heat exchanger, Prithiviraj et al. [39] reported the need of at least 150 million elements within a model containing 500 tubes and 10 baffles. Fadhl et al. [98] carried out a transient simulation of a two-dimensional CFD model of a small thermosyphon charged with water, 500mm in length. For an accurate simulation, they reported the use of a very small time step of 0.0005 seconds as to catch the fine interface between liquid and vapour. Moreover, the steady state condition was reached after 60 seconds. Speaking of an industrial size heat exchanger integrated with several heat pipes, the model would require an enormous amount of time to perform the simulation, which is not possible by using an ordinary computer.

In the current project and to overcome the mentioned drawbacks by increasing the speed of the simulation modelling, many simplifications of the real DD-HX were considered. A smaller scale unit with a small number of thermosyphons was designed. Also, the two-phase heat transfer mechanisms within the thermosyphons were replaced by pure conduction where the thermal conductivity parameter was calculated from the resistance approach discussed in the previous chapter.

The heat exchanger model was constructed in ANSYS Workbench 16.2. Figure 3.8 shows a schematic diagram describing the process followed by ANSYS Fluent starting from building the model to generate and post-process the results which will be explained in the following sections.

3.2.1. DesignModeler and mesh generation

In order to predict the thermal behaviour of the shell-side fluids, the three cases were drawn in ANSYS DesignModeler (Figure 3.9). The first case was numerically modelled in the literature by Ramos et al [84], and represented a cross-flow configuration of the modelled TSHX system. The exact same dimensions used to build the theoretical model were applied for the numerical model, and were also be applied for experimental testing to achieve a fair validation.

As it can be seen from the figure, a maximum of three passes around the 6 thermosyphons were installed. There are two important limitations that restricted the number of passes on the evaporator shell-side. The first limitation comes from controlling the computational cost of the model as adding more passes increases the number of grid cells needed within the domain, hence increasing the computing cost. Another limitation arises from building the actual test rig during the experimental stage, as more passes require more materials and bigger equipment to overcome the higher pressure drop across the inlet and outlet of the evaporator shell-side, hence a higher running cost. As mentioned before, the

6 thermosyphons are represented as 6 solid rods during the numerical modelling, which can be seen as a dark colour mounted in a vertical position in Figure 3.9. It is also worth mentioning that both numerical and experimental tests were carried out in parallel.

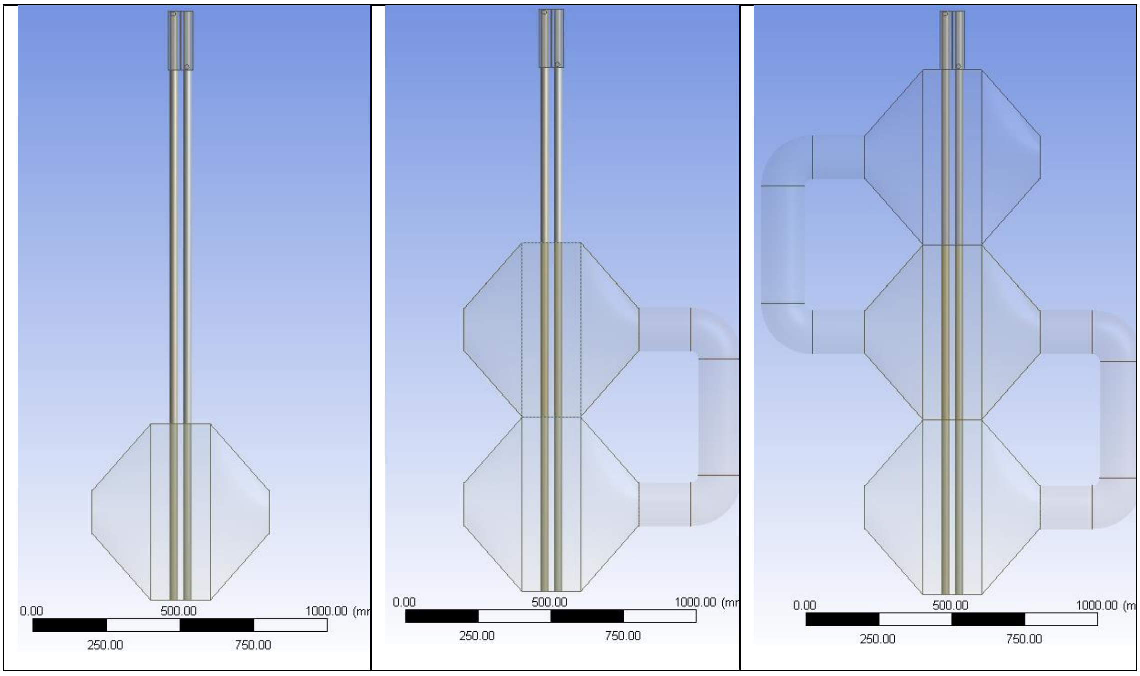

Figure 3.9 – Cases 1, 2 and 3 drawn in DesignModeler.

Grid generation has a significant impact on the accuracy of the model and various considerations are taken into account when generating high quality CFD meshes. Following the construction of the three cases in DesignModeler, the models are then discretised in ANSYS meshing.

In DesignModeler, each time a body is created it is placed in a new part. In Case 3, for example, a total of 14 bodies were created giving a total of 14 new parts. Bodies include two elbows, 1st pass, 2nd pass, 3rd pass, six rods, condenser, condenser inlet and condenser outlet. All the 14 parts must be converted into a single part using the “Form New Part” command which is available in the ANSYS DesignModeler application and known as “multibody parts”. This step is important; otherwise each body will be meshed separately causing no connection between the bodies, hence causing inaccurate results or even errors. This can be shown in Figure 3.10 where the two bodies are connected with common mesh nodes at various locations around the interface. Appendix B shows another close-up photo of the mesh connecting the rods and the surrounding fluid. This step was also necessary as without it, two bodies of the same fluid will not be merged. In other words, air won't flow from the first pass through the elbow as the two bodies will be separated by a virtual wall.

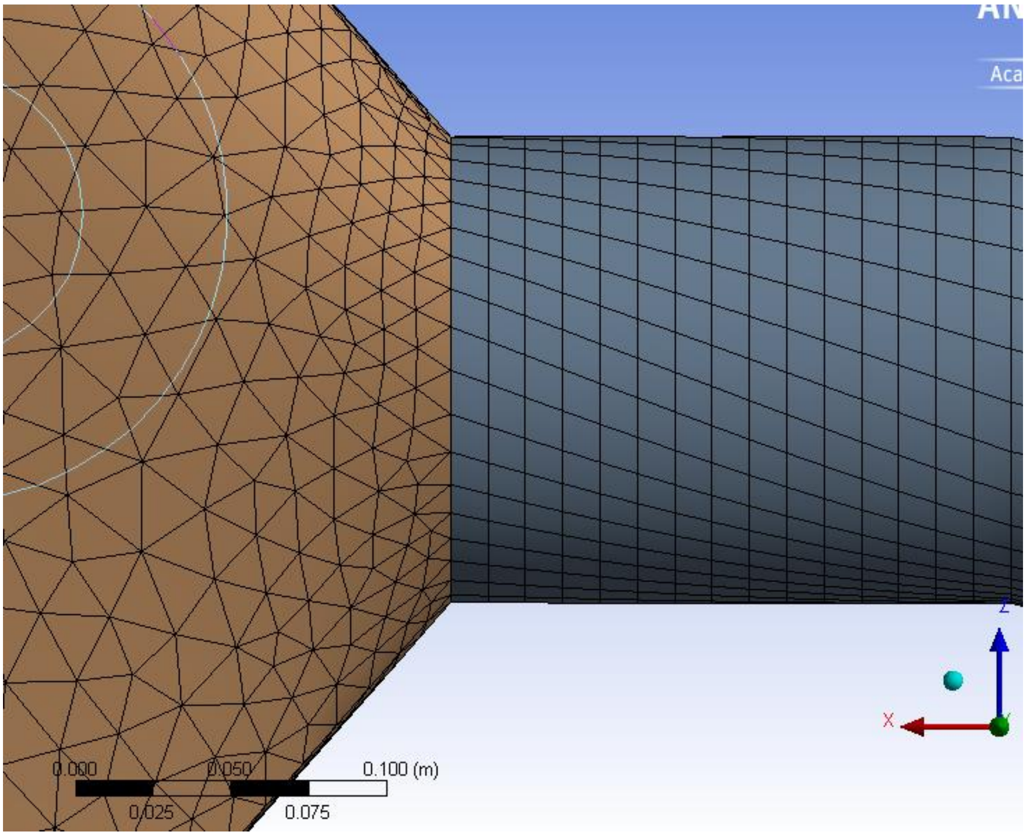

Figure 3.10 – Close-up photo of the mesh connection between the elbow and pass 3.

A grid analysis study was initially conducted in order to choose an optimised mesh to run the three different cases at various air inlet conditions. The analysis compared the results with experimental data to ensure an adequate number of elements while minimising computational cost and time. Simulations were run at different test conditions and mesh densities. Several mesh densities were tested, however, only three different densities were chosen for the analysis: coarse, medium and fine. The comparison between experimental and numerical results mainly focused on the evaporator and condenser outlet temperatures, i.e. air and water outlet temperatures. For comparison, one mesh density was chosen and applied to the three test cases and this was based on a grid analysis for the most complicated case, i.e. case 3.

Table 3.7 – Mesh parameters for case 3.

	Coarse	***Medium***	***Fine***
Relevance	0	50	100
Nodes	650,472	1,600,751	2,328,476
Elements	2,147,026	4,942,635	8,009,957
Maximum skewness	0.88	0.89	0.84
Average skewness	0.228	0.220	0.211
Iteration per second	2-5 s	6-10 s	11-15 s

As mentioned above, mesh refinement was conducted on the most complicated case (case 3) by changing the relevance value in the global mesh sizing control. Relevance is a useful parameter to achieve an automatic global refinement or coarsening of the mesh. The default value of the relevance is 0 and the value can be changed between -100 to +100, where the values of -100 and +100 correspond respectively to a very coarse mesh and a very fine mesh. Three different mesh densities were chosen based on increasing the relevance value from 0 (coarse) to 100 (fine), where a relevance of 50 was considered as a medium size mesh. Table 3.7 shows the different parameters which were taken into account when analysing the mesh size and quality. It can be clearly noted that an increase of the relevance value increases the number of elements, simulation time and improves the quality of the mesh by reducing the skewness of the cells, where, an increase in the skewness can cause convergence issues during the simulation. The skewness was taken as a parameter to measure the quality of the mesh. Based on ANSYS meshing user guide [99], the skewness is a measure of how close a cell is from an ideal cell, where a skewness of zero and 1 correspond to an equilateral and degenerate cell quality respectively (Table 3.8).

Table 3.8 – List of skewness values with corresponding cell quality [99]**.**

Value of Skewness	**Cell Quality**
1	Degenerate
0.9 — <1	Bad
0.75 — 0.9	Poor
0.5 — 0.75	Fair
0.25 — 0.5	Good
>0 — 0.25	Excellent
0	Equilateral

According to ANSYS meshing user guide for 3D problems [99], the quality of most cells should be good or better, therefore a value of skewness less or equal to 0.5. Only a small percentage of cell quality should be fair and very few cells in the poor range. From looking at Figure 3.11, the skewness is plotted for the entire model, more specifically for case 3. Exactly what ANSYS meshing user guide suggested is applied to the current model, the majority of the cells clearly lie below 0.5, hence in the good cell quality range, followed by just a small percentage in the fair range and a very few cells have a poor quality. A photo of an automatic generated mesh with high skewness for case 3 is available in Appendix B. The photo shows a clear bad quality mesh as the skewness is very close to 1.

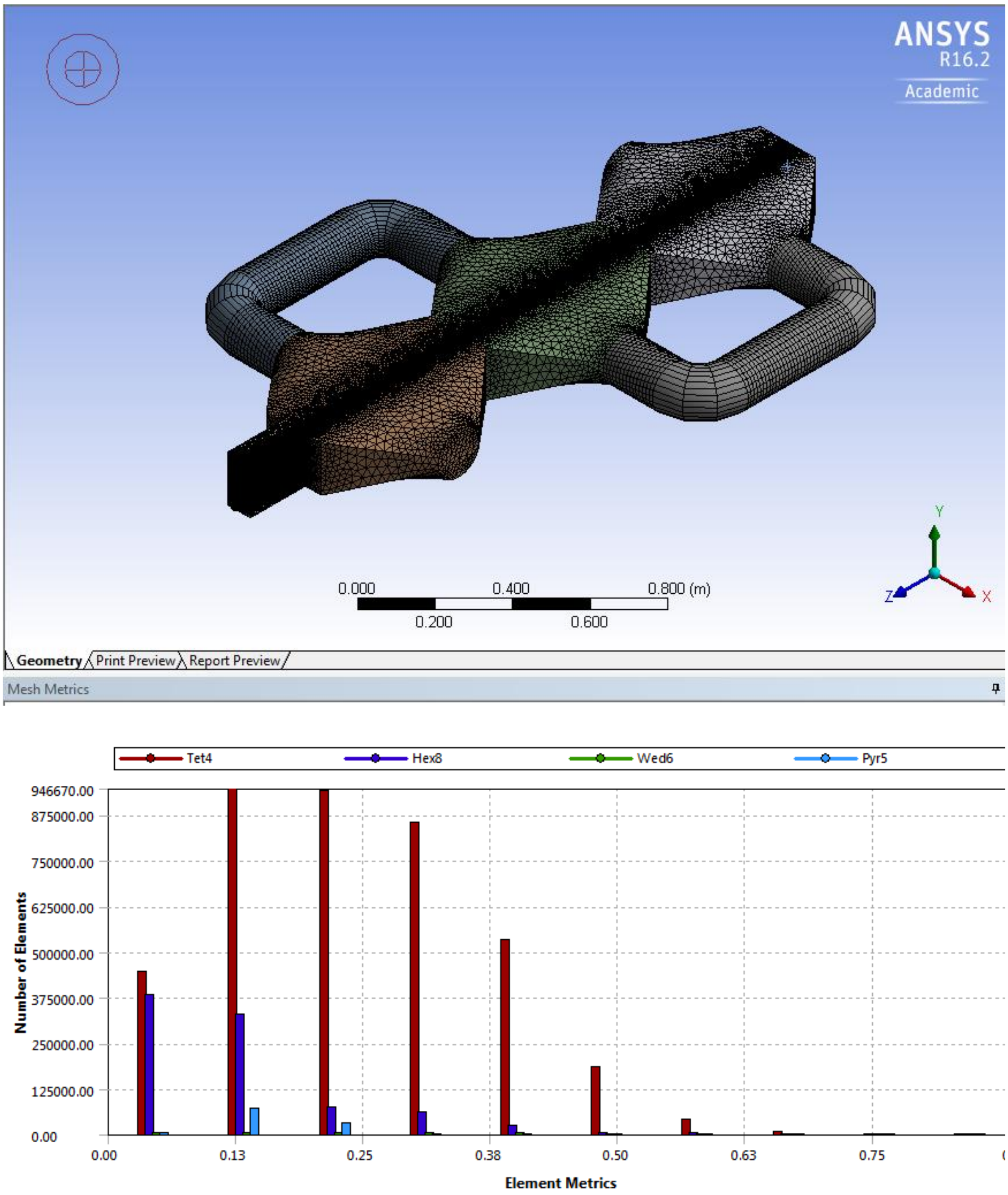

Figure 3.11 – Skewness graph for case 3, medium mesh size.

The mesh generated was dominated by tetrahedral shaped elements located everywhere in the control volume except in the elbows and solid rods, which were dominated by hexahedral elements (Figure 3.12 and Figure 3.13).

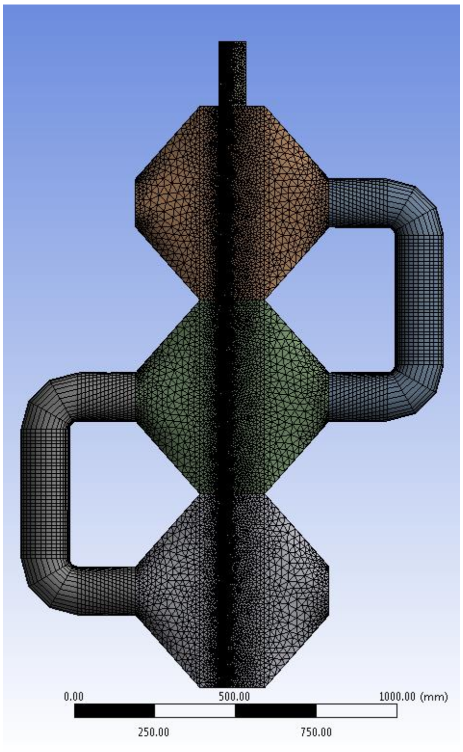

Figure 3.12 – Medium mesh of the whole system (case 3).

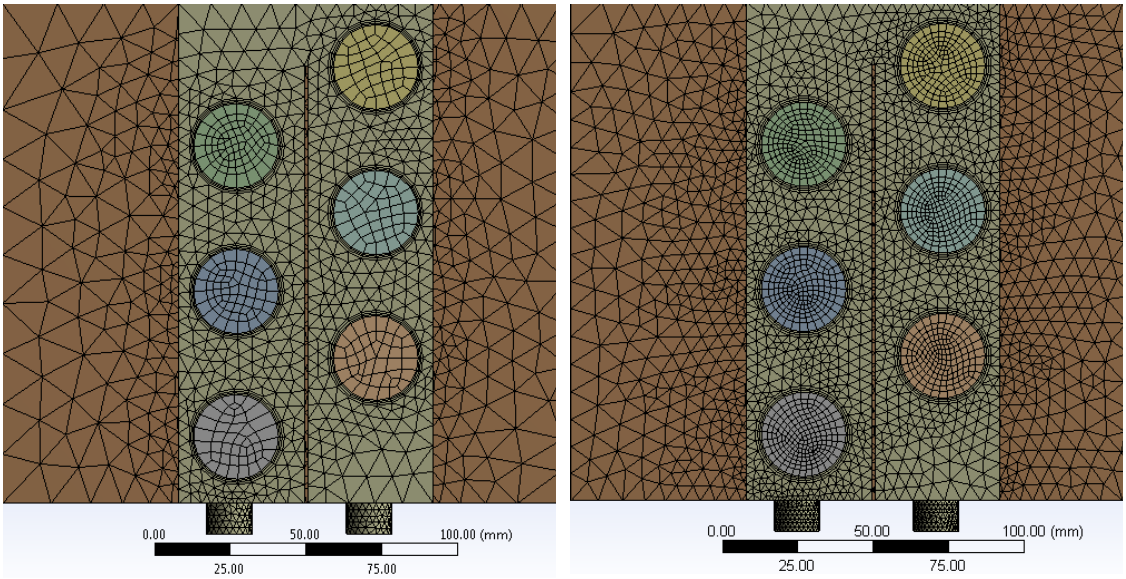

Figure 3.13 – Top view of the condenser: Coarse mesh (left) and fine mesh (right).

In order to simulate the convective heat transfer between the fluids (air and water) and the solid rods accurately, an inflation layer consisting of three layers of elements was placed around the six solid rods (Figure 3.13). The presence of an inflation layer would increase the skewness of the mesh as it may cause a stairstep in the mesh. However, it leads to more accurate results as the critical regions in the domain are the solid-fluid interfaces; therefore a thin layer is needed to develop a smooth thermal boundary layer.

3.2.2. Grid analysis

Figure 3.14 to Figure 3.17 show the percentage error between CFD and experimental results for case 3, being the most complicated case. The analysis was conducted on two different air inlet conditions (150 and 250°C). The figures clearly show that the medium mesh and the fine mesh produce almost identical results, which demonstrates that increasing the number of elements beyond the medium mesh will just increase computational time and cost with no significant improvement in the accuracy of the results. Hence, the fine mesh was excluded from the analysis. The figures also illustrate that the coarse mesh has performed better, in terms of producing results closer to the experimental results, than the medium mesh. The coarse mesh, however, caused issues regarding convergence as the residuals showed a significant fluctuation for all the transport equations including continuity, energy and momentum. Based on the previous analysis, the medium mesh was chosen for all three cases for the rest of the simulations. Another characteristic can be deduced from the above results related to the signs of the errors. The positive values for air outlet temperatures indicate that the CFD over-predicts the air outlet temperatures. The heat exchanger wall was set to be 100% adiabatic during the simulations, which neglects any heat loss across the boundary, resulting in slightly elevated air outlet temperatures.

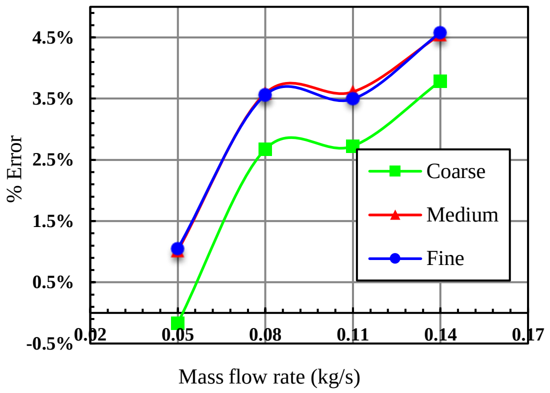

Figure 3.14 – Percentage error at 150°C for the air outlet temperatures (case 3).

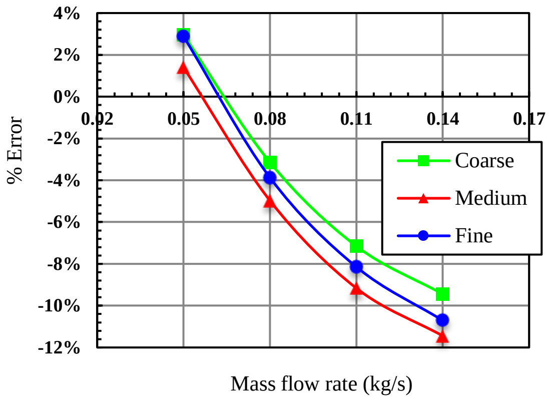

Figure 3.15 – Percentage error at 150°C for the water outlet temperatures (case 3).

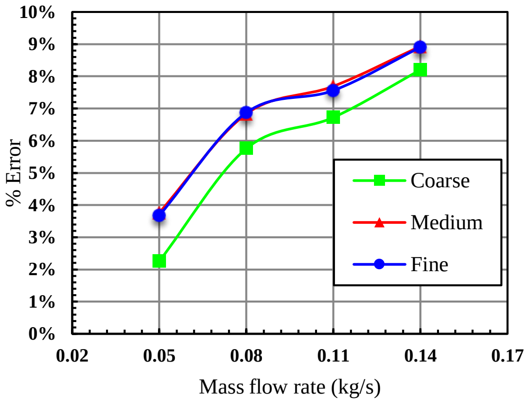

Figure 3.16 – Percentage error at 250°C for the air outlet temperatures (case 3).

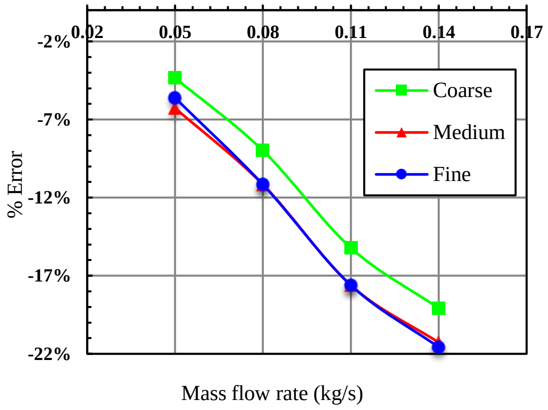

Figure 3.17 – Percentage error at 250°C for the water outlet temperatures (case 3).

3.2.3. Boundary conditions

ANSYS Fluent offers a wide range of boundary conditions to be applied on inlets, outlets and walls of a particular physical model. In order to select the most appropriate boundary condition, a good understanding of the solution domain is essential and makes the choice of selection easier. Many variables should be taken into account when studying the solution domain; such variables include the behaviour of pressure, velocity, density and temperature.

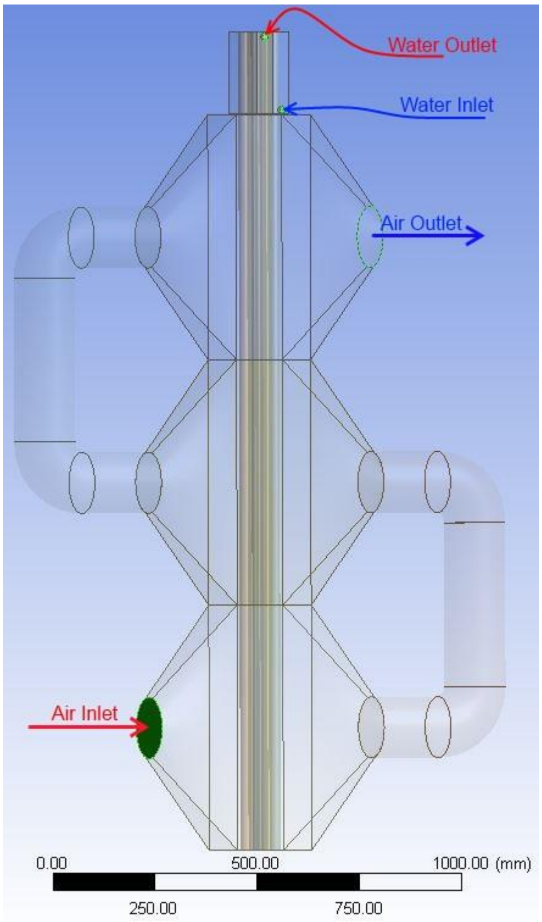

Figure 3.18 – Inlet and outlet boundary conditions locations (case 3).

The heat exchanger under investigation consists of two fluids: air (evaporator) and water (condenser). The density of both fluids was considered to be temperature-dependent as shown in Appendix A. The temperature change effect on density was small for air and even smaller for water due to the insignificant change in temperature between each inlet and outlet. The behaviour of the two fluids was then considered as incompressible.

Table 3.9 shows the different boundary types and test conditions that were chosen for the simulation while Figure 3.18 shows the location zones. The mass flow rate was defined at both evaporator and condenser inlets, while the pressure was defined at both outlets.

Referring to ANSYS Fluent user guide 16.2 [48], both mass flow inlet and velocity inlet boundary conditions are equally compatible with incompressible flow, although it was easier to deal with the mass flow rate. The velocity, however, can be calculated from equation (3.3) and applied as a boundary condition.

Table 3.9 – Boundary conditions.

	BC Type	**Mass Flow Inlet (kg/s)**	**Inlet Temperature (°C)**
Air Inlet	Mass flow inlet	0.05 to 0.14 at increments of 0.03	100 to 250 at increments of 50
Air Outlet	Pressure outlet	—	—
Water Inlet	Mass flow inlet	0.08	≈15
Water Outlet	Pressure outlet	—	—

On the other hand, a pressure outlet boundary condition type was applied on both air and water flow outlets. ANSYS Fluent user guide clearly describes every boundary condition and its limitations. For an unsteady flow with changing density, even if the flow is incompressible, it is advisable to use a pressure outlet [48] which is the case in the current model. The outflow boundary condition type was not considered at the outlet as it is mostly applicable for stable and fully developed flow, which is not the case in the model.

Table 3.10 – Default settings for pressure outlet conditions.

Gauge Pressure (Pa)	0
Backflow Total temperature (K)	300
Backflow Turbulent Intensity	5%
Backflow Turbulent Viscosity Ratio (kg/m.s)	10

The pressure outlet boundary condition relies on a few parameters shown in Table 3.10. The default values were considered due to insufficient information on the flow behaviour at the outlet boundary. The outlet backflow re-entering the computational domain is unknown, therefore, a direction vector normal to the outlet boundary was specified for the backflow direction specification method to avoid recirculation at the outlet, hence convergence difficulties will be minimised.

On the evaporator (air) side, four different mass flow rates were considered: 0.05, 0.08, 0.11 and 0.14 kg/s. For each mass flow rate, four different inlet temperatures were examined: 100, 150, 200 and 250°C, giving a total of 16 different combinations of mass flow rate and inlet temperature. On the condenser (water) side, only one mass flow rate and one inlet temperature were chosen, 0.08 kg/s and 15°C respectively. In Fluent, the heat exchanger walls were set as adiabatic ($\dot{Q} = 0$) and a no-slip condition was imposed on all walls. In the case of external flows, it is recommended that turbulence intensity and viscosity ratio should be specified at the inlet [100]. No information was available for the inlet turbulence intensity of either air or water flows, and therefore the default value of 5% was chosen for both inlets.

As mentioned before, the properties of both fluids (air and water) were treated as temperature-dependent. A simple user-defined function (UDF) was written in the C programming language (see Appendix A) and linked to Fluent to customise the properties of air and water. The UDF is used to update the density, dynamic viscosity and specific heat on each cell at every iteration based on the temperature change. This is important as it gives a more realistic visualisation of the velocity distribution as properties affect the convection heat transfer around the pipes. There are three arguments to $DEFINE\_PROPERTY$: $name, c$ and t. The $name$ is supplied, in this case, density, specific heat and dynamic viscosity. The other two arguments, c and t are variables known as cell and thread, respectively. The variables are passed by the solver (ANSYS Fluent) to the written UDF where only the $real$ properties are computed for a single cell then returned to the solver.

3.2.4. Turbulence modelling

Based on the combination chosen for air inlet mass flow rates and temperatures, and on the equations provided for external flow around a tube bank in a staggered arrangement (section 3.1.2), the Reynolds number was found to be in the range of 10^4, hence the flow is turbulent.

According to the literature, the Reynolds-averaged Navier-Stokes (RANS) equations approach was chosen for this investigation to close the system of mean flow equations. Overall, RANS models are very well-known to be the most economic approach to solve complex industrial flow problems. The numerical modelling for this project focuses more on the shell-side convection heat transfer. For this reason, Large Eddy Simulation (LES) was not considered as it is more suitable for projects where the flow distribution and visualisation is more important, thus requiring a denser mesh to catch the small eddies within the flow, which is computationally more expensive. The investigation of particulate fouling would be ideal for using such an approach if a high power computer is available.

The three-dimensional Realizable $K - \varepsilon$ turbulence model was adopted by many researchers [84,101,102] to model the shell side heat transfer in various types of heat exchangers, and has provided satisfactory results. The Realizable $K - \varepsilon$ was employed in this project for all the multi-pass configurations as it is suitable for cases where a model involves moderate swirl, vortices and flow separation without providing an accurate resolution of the boundary layer separation [103]. In addition, a pressure-based solver was chosen as it is more efficient in steady-state simulations [84]. The residuals of all the transport equations were set to 10^{-6} to give enough time for the simulation to reach a steady-state condition. In the solution methods, the SIMPLE algorithm scheme was chosen with satisfactory results (shown in section 4.2).

3.2.5. Near-wall treatment and convergence

The presence of walls within the domain significantly enhances turbulence. Moreover, the non-slip condition applied on the walls affects the mean velocity of the field, causing in return, higher turbulence. In the current project, air and water flow across the tube bundle of six cylindrical rods, through which heat transfer is taking place near the tubes' wall region. To account for the wall effects in the region close to the wall, two approaches are available in Fluent for this modelling which are both considered as a near-wall treatment: wall function approach and near-wall model approach.

The region near the wall can be subdivided into three layers: viscous sublayer, buffer and fully turbulent layer. The viscous sublayer region, also known as the laminar region, is the first layer closest to the wall. Since a no-slip condition is imposed on the wall, the turbulent stresses vanish which makes the viscous stresses dominant in that region. This region greatly affects both momentum and heat transfer.

In the outer region, the flow is fully turbulent and unaffected by the viscosity near the wall. Lastly, the region between the viscous sublayer and outer layer is known as the buffer layer where both fluid viscosity and turbulence are evenly contributing (Figure 3.19).

A dimensionless distance known as y^+, normal to the wall, is used as a parameter to indicate the distance at which a certain layer is located from the wall, and defined as,

$$y^+ = \frac{\rho_f u_\tau y}{\mu_f} \quad \text{where,} \; u_\tau = \sqrt{\frac{\tau_{wall}}{\rho_f}} \tag{3.22}$$

where y is the first cell height away from the wall which is 0.6 mm as the first layer thickness for the inflation layer was set to that value. u_τ is the friction velocity and τ_{wall} is the wall shear stress which is affected by the velocity of the fluid near the wall. The subscript f refers to the fluid, which is air and water on the evaporator and condenser shell side, respectively. The calculation of y^+ is however not required as it is available in ANSYS Fluent.

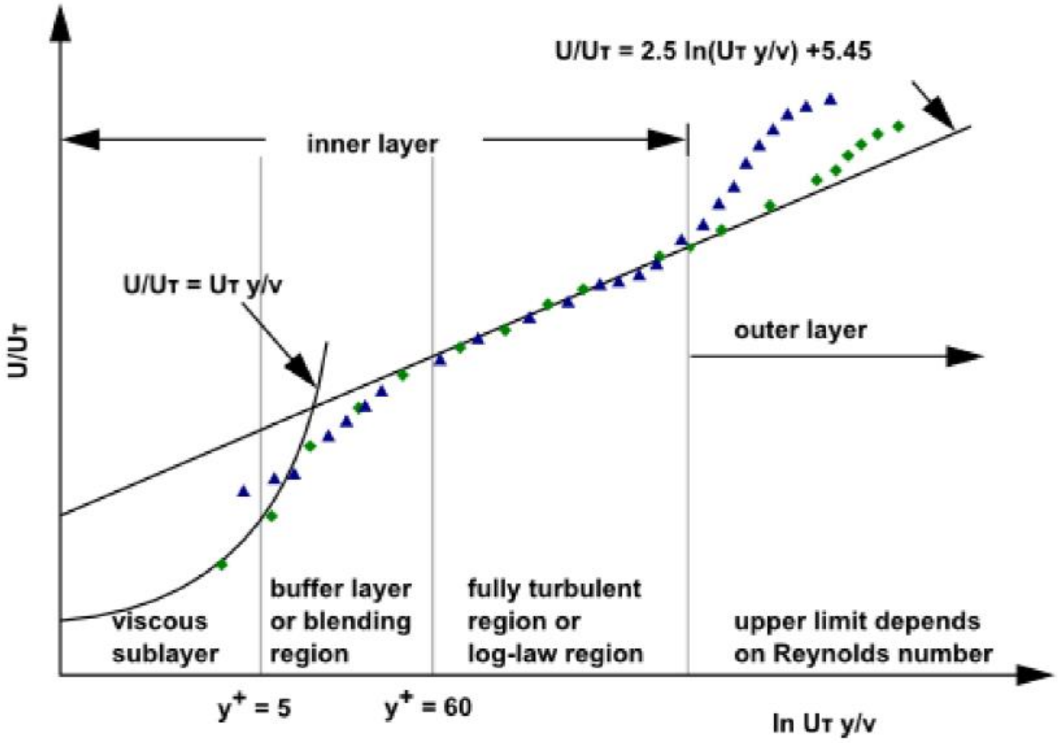

Figure 3.19 – Near-wall region [47].

Depending on the type of problem and the accuracy needed, the near wall region can be resolved using either a near-wall model approach or a wall function. Both approaches are available with the $K - \varepsilon$ turbulence model.

The near-wall model approach, such as “Enhanced wall treatment”, operates by modifying the turbulence model which allows resolving the complete near-wall region, including the viscosity-affected region all the way down to the wall. This approach requires a very fine mesh near the wall to achieve a good resolution of the boundary layer.

The wall function approach avoids modifying the chosen turbulence model and does not resolve the viscosity-affected region near the wall (viscous and buffer layer), instead, wall functions are used to link the viscosity-affected region between the wall with the fully turbulent region. Both approaches are schematically shown in Figure 3.20.

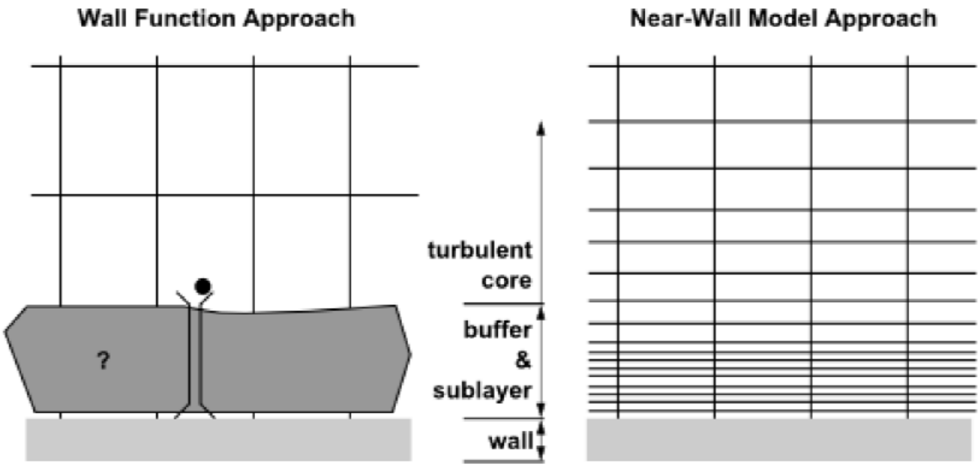

Figure 3.20 – Near-wall treatment [47]**.**

In the current project, the near-wall model approach is not necessary as a detailed study of the boundary layer development near the tube bundle is desirable but not essential, in addition to limiting computational power and time. Moreover, the focus of the project is to use ANSYS Fluent as a tool to develop a validated model to be used in future heat exchanger systems. Hence, the wall function approach was implemented.

In general, and based on the literature, all the research that has been dedicated to numerical modelling of multi-pass heat exchangers (i.e. STHXs) in ANSYS

Fluent, have used the standard wall function to model the near-wall region, although the choice of such near-wall treatment was not well justified and other wall functions don’t seem to have been used. Referring to ANSYS Fluent user and theory guide [48,47], the scalable wall function is in general more recommended than the standard wall function. Although the shortcoming of all wall functions due to the deterioration of the numerical results if the near wall region is under refined, the scalable wall function was exceptional.

The value of y^+ relies on the overall Reynolds number. In general, a y^+ value of less than 15 near the wall usually results in causing errors in wall shear stress and wall heat transfer. Except for the scalable wall function, such errors cause a deterioration of the wall function used, hence decreasing the accuracy of the results. Hence, a y^+ value of about 15 has been taken as a lower limit. For a coarser mesh of y^+ greater than 11, both standard and scalable wall functions have identical effect [47].

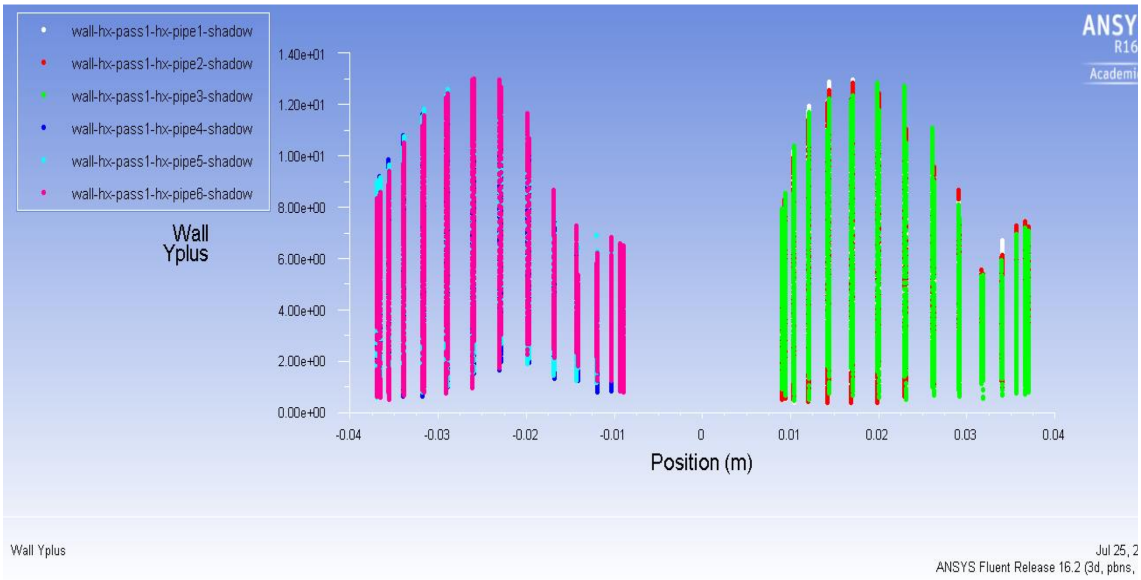

Figure 3.21 – y-plus value on the first cell near the 6 solid rods (case 2, 150°C, 0.14 kg/s).

As it can be seen from Figure 3.21, the value of y-plus was plotted in ANSYS Fluent around each pipe for case 2 using standard wall function. The y-plus value is calculated at the closest node to the pipe wall, more specifically, at a distance of 0.6 mm which is the value specified for the first layer thickness in the inflation layer. The figure shows that all the y-plus values fall below 15. Hence, the use of the scalable wall function.

There are several things to take into consideration when checking the reliability of a model. Obviously, what mainly needs to be taken into account is how close the numerical and experimental are. Besides that, other parameters should be looked at to gain an understanding of the fluid flow and thermal behaviour inside the model. Such parameters include the total heat transfer rate, which can be used as an indication of the energy balance of the system

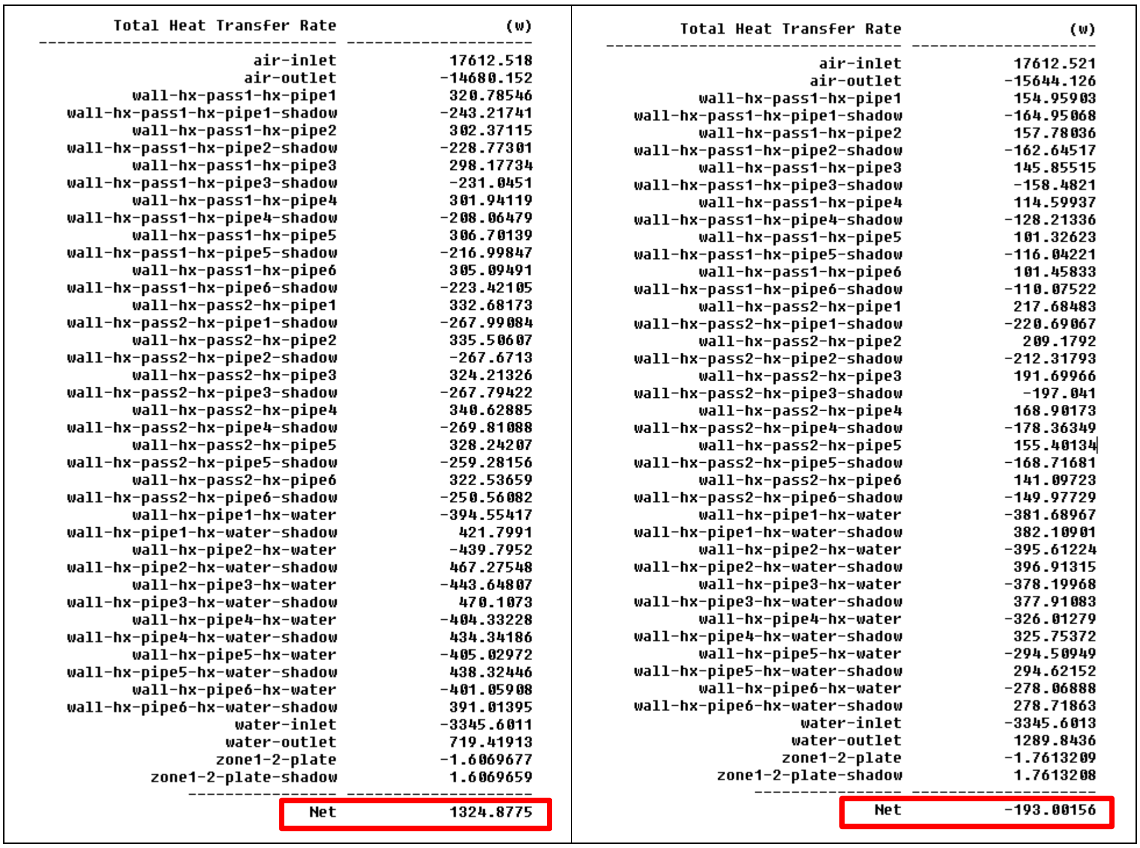

```
        Total Heat Transfer Rate                  (w)
-------------------------------- --------------------
                       air-inlet            17612.518
                      air-outlet           -14680.152
          wall-hx-pass1-hx-pipe1            320.78546
   wall-hx-pass1-hx-pipe1-shadow           -243.21741
          wall-hx-pass1-hx-pipe2            302.37115
   wall-hx-pass1-hx-pipe2-shadow           -228.77301
          wall-hx-pass1-hx-pipe3            298.17734
   wall-hx-pass1-hx-pipe3-shadow            -231.0451
          wall-hx-pass1-hx-pipe4            301.94119
   wall-hx-pass1-hx-pipe4-shadow           -208.06479
          wall-hx-pass1-hx-pipe5            306.70139
   wall-hx-pass1-hx-pipe5-shadow           -216.99847
          wall-hx-pass1-hx-pipe6            305.09491
   wall-hx-pass1-hx-pipe6-shadow           -223.42105
          wall-hx-pass2-hx-pipe1            332.68173
   wall-hx-pass2-hx-pipe1-shadow           -267.99084
          wall-hx-pass2-hx-pipe2            335.50607
   wall-hx-pass2-hx-pipe2-shadow            -267.6713
          wall-hx-pass2-hx-pipe3            324.21326
   wall-hx-pass2-hx-pipe3-shadow           -267.79422
          wall-hx-pass2-hx-pipe4            340.62885
   wall-hx-pass2-hx-pipe4-shadow           -269.81088
          wall-hx-pass2-hx-pipe5            328.24207
   wall-hx-pass2-hx-pipe5-shadow           -259.28156
          wall-hx-pass2-hx-pipe6            322.53659
   wall-hx-pass2-hx-pipe6-shadow           -250.56082
          wall-hx-pipe1-hx-water           -394.55417
   wall-hx-pipe1-hx-water-shadow             421.7991
          wall-hx-pipe2-hx-water            -439.7952
   wall-hx-pipe2-hx-water-shadow            467.27548
          wall-hx-pipe3-hx-water           -443.64807
   wall-hx-pipe3-hx-water-shadow             470.1073
          wall-hx-pipe4-hx-water           -404.33228
   wall-hx-pipe4-hx-water-shadow            434.34186
          wall-hx-pipe5-hx-water           -405.02972
   wall-hx-pipe5-hx-water-shadow            438.32446
          wall-hx-pipe6-hx-water           -401.05908
   wall-hx-pipe6-hx-water-shadow            391.01395
                     water-inlet           -3345.6011
                    water-outlet            719.41913
                   zone1-2-plate           -1.6069677
            zone1-2-plate-shadow            1.6069659
                ---------------- --------------------
                             Net            1324.8775
```

```
        Total Heat Transfer Rate                  (w)
-------------------------------- --------------------
                       air-inlet            17612.521
                      air-outlet           -15644.126
          wall-hx-pass1-hx-pipe1            154.95903
   wall-hx-pass1-hx-pipe1-shadow           -164.95068
          wall-hx-pass1-hx-pipe2            157.78036
   wall-hx-pass1-hx-pipe2-shadow           -162.64517
          wall-hx-pass1-hx-pipe3            145.85515
   wall-hx-pass1-hx-pipe3-shadow            -158.4821
          wall-hx-pass1-hx-pipe4            114.59937
   wall-hx-pass1-hx-pipe4-shadow           -128.21336
          wall-hx-pass1-hx-pipe5            101.32623
   wall-hx-pass1-hx-pipe5-shadow           -116.04221
          wall-hx-pass1-hx-pipe6            101.45833
   wall-hx-pass1-hx-pipe6-shadow           -110.07522
          wall-hx-pass2-hx-pipe1            217.68483
   wall-hx-pass2-hx-pipe1-shadow           -220.69067
          wall-hx-pass2-hx-pipe2             209.1792
   wall-hx-pass2-hx-pipe2-shadow           -212.31793
          wall-hx-pass2-hx-pipe3            191.69966
   wall-hx-pass2-hx-pipe3-shadow             -197.041
          wall-hx-pass2-hx-pipe4            168.90173
   wall-hx-pass2-hx-pipe4-shadow           -178.36349
          wall-hx-pass2-hx-pipe5            155.40134
   wall-hx-pass2-hx-pipe5-shadow           -168.71681
          wall-hx-pass2-hx-pipe6            141.09723
   wall-hx-pass2-hx-pipe6-shadow           -149.97729
          wall-hx-pipe1-hx-water           -381.68967
   wall-hx-pipe1-hx-water-shadow            382.10901
          wall-hx-pipe2-hx-water           -395.61224
   wall-hx-pipe2-hx-water-shadow            396.91315
          wall-hx-pipe3-hx-water           -378.19968
   wall-hx-pipe3-hx-water-shadow            377.91083
          wall-hx-pipe4-hx-water           -326.01279
   wall-hx-pipe4-hx-water-shadow            325.75372
          wall-hx-pipe5-hx-water           -294.50949
   wall-hx-pipe5-hx-water-shadow            294.62152
          wall-hx-pipe6-hx-water           -278.06888
   wall-hx-pipe6-hx-water-shadow            278.71863
                     water-inlet           -3345.6013
                    water-outlet            1289.8436
                   zone1-2-plate           -1.7613209
            zone1-2-plate-shadow            1.7613208
                ---------------- --------------------
                             Net           -193.00156
```

Figure 3.22 – Total heat transfer for: Standard wall function (left) and Scalable wall function (right), (case 2, 150°C, 0.014kg/s).

A comparison was made between the total heat transfer rates between the two wall functions: standard and scalable. This is shown in Figure 3.22 and computed by the following formula:

$$Q_{total} = Q_{convection} + Q_{conduction} + Q_{radiation} \tag{3.23}$$

where radiation heat transfer was not taken into consideration. Depending on the specified boundary condition, the convection heat transfer is then calculated, where 25°C is taken as the reference temperature. The conduction heat transfer through the cylindrical rods will be explained in more detail in section 4.2.4. In general, the conduction heat transfer is calculated by the product of the thermal conductivity of the material along with the dot product of both temperature gradient and the projected area through which the heat is flowing.

Ideally, and based on the energy balance equation, the net heat result of the total heat transfer of any system should be zero. The total heat transfer rate of the system using the standard wall function is shown in Figure 3.22 as 1324.88 W, whereas the value is 193 W when using the scalable wall function. This indicates lower heat losses achieved when using the scalable rather than the standard wall function. A possible reason could be due to the inaccurate prediction of the near wall region under the standard wall function, because of the low value of y^+.

Convergence

There is no universal method for judging the convergence of results. Different inlet conditions and cases converged at different times and residual levels than was expected. Convergence mainly depends on the size of the case and the initial guess of the flow field. Based on ANSYS Fluent user guide [48], it is noted that the convergence should be judged on both value and behaviour. A continuous decrease or maintaining a low residual is desirable for several iterations before assuming that a solution is converged. In general, the default convergence criterion in ANSYS Fluent is sufficient in most cases, however it is advisable to let the criterion be as low as 10^{-6} for the energy equation and 10^{-3} for the other variables.

In all the modelled cases, it was observed that the more passes on the evaporator, the longer time the model took to converge. As mentioned before, all the criteria in the residuals were set to 10^{-6} to give all the cases sufficient time to reach a steady state condition. In some cases and inlet conditions, the criterion was inappropriately chosen which gave the opportunity to look for other sources to judge the convergence. To ensure that all the cases achieved a converged solution, a few parameters were analysed in more detail. The temperatures on both evaporator and condenser outlets were plotted at the end of each iteration and displayed to observe their behaviour. As both outlet temperatures reached a constant value, this implied that both conductive and convective heat transfer inside the model have reached a steady state condition. This was a good indication that the system achieved a converged solution. Another parameter that was kept under observation is the scaled residuals, i.e. continuity, velocity, energy, etc. Some inlet conditions converged before reaching the defined scaled residual of 10^{-6}, but as long as the residuals are decaying to a small value then levelling out, a solution was considered to be converged.

For all cases, the maximum number of iteration was set to 5000 to provide sufficient time for convergence. The scaled residuals were observed to ensure a smooth decrease is maintained throughout the simulation, as in steady flows, fluctuating residuals should be avoided.

3.3. Experimental methodology

Following the theoretical and CFD modelling of the designed multi-pass heat exchanger, essential experimental validation was carried out in order to achieve a validated CFD model. The test rig was manufactured at Econotherm (UK) Ltd. (Bridgend, Wales), a company specialised in manufacturing waste heat recovery systems integrated with heat pipe technology. Ramos et al. [84] carried out the experimental work of the cross-flow configuration (case 1) of the thermosyphon heat exchanger (TSHX). The test rig was then updated into two and three pass configurations for the investigation.

3.3.1. Single thermosyphon

3.3.1.1. Test rig

To ensure the correct correlations are used for the theoretical modelling of the system, it was important to characterise the thermal performance of an individual thermosyphon. This was done by operating the thermosyphon under different inlet conditions and parameters that have an effect on thermal performance.

The tested thermosyphon was the same as the ones that were installed in the multi-pass heat exchanger. The thermosyphon consisted of a 2m long carbon steel tube with an outer diameter of 28mm and a wall thickness of 2.5mm. The rest of the parameters are listed in Table 3.11.

Table 3.11 – Design summary of the thermosyphon.

Parameters	
Wall material	Carbon-steel
Outer diameter (mm)	28
Wall thickness (mm)	2.5
Total length (m)	2
Evaporator length (m)	1
Adiabatic length (mm)	800
Condenser Length (mm)	200
Filling ratio= $\frac{V_{fluid}}{V_{evaporator}}$ (%)	50

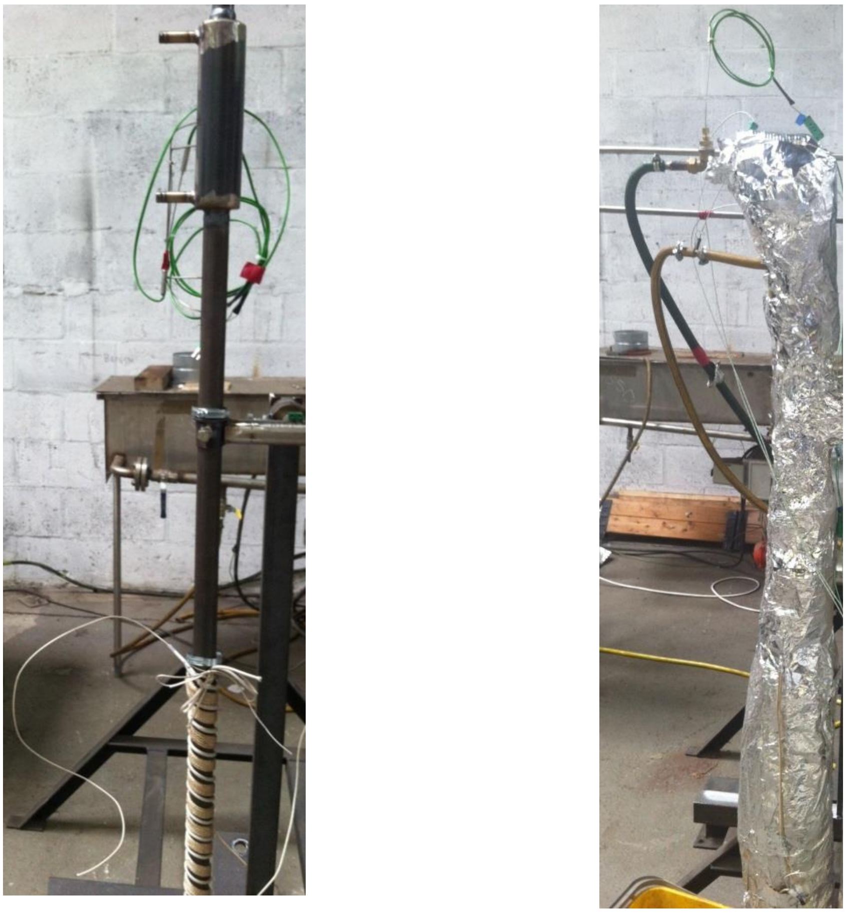

Figure 3.23 – Single thermosyphon, uninsulated (Left) and insulated (Right).

Figure 3.24 shows a schematic diagram of the experimental apparatus used in this investigation. The test rig consisted of a thermosyphon, heater, measuring instruments and cooling water circuit. Three rope heaters of 500 W each were wrapped around the thermosyphon covering the total evaporator section of 1m in length, leaving the adiabatic section with a length of 800 mm. A Rockwool insulation type was placed around the thermosyphon outer wall where it was wrapped with a thermal insulation foil as shown in Figure 3.23. The insulation increased the thermal resistance to convection heat transfer, hence reducing the heat loss to surroundings.

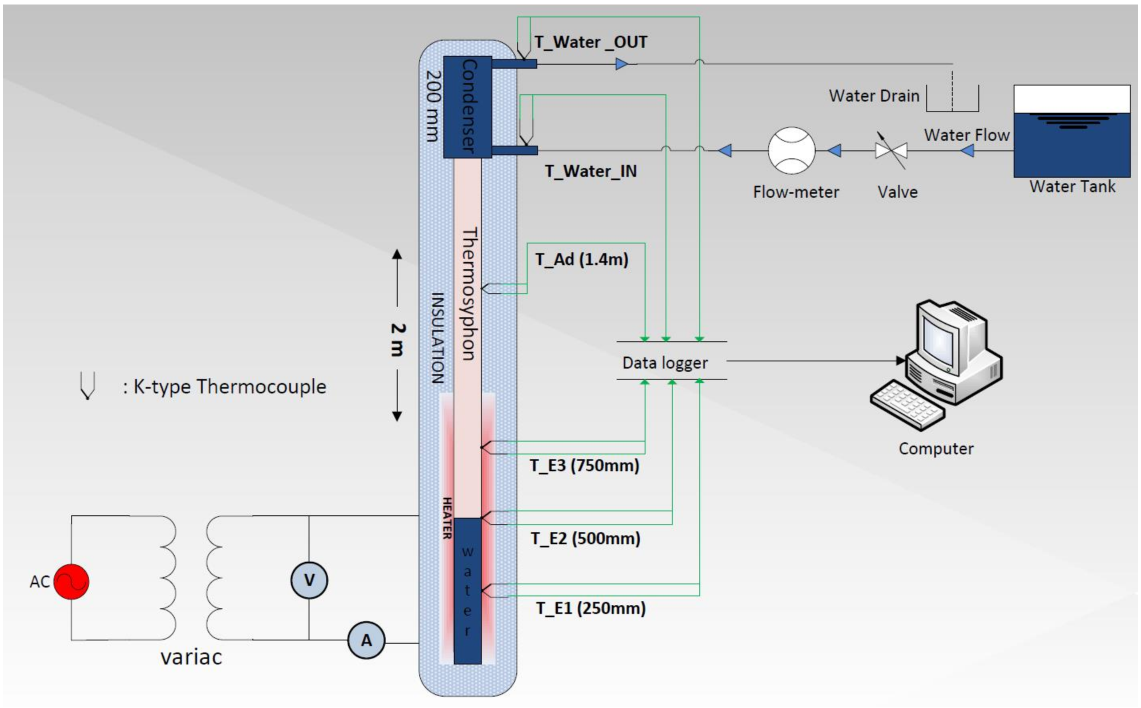

Figure 3.24 – Schematic diagram of the tested thermosyphon.

3.3.1.2. Filling ratio (FR)

The thermal performance of a thermosyphon is significantly affected by various parameters including the geometry, thermal and hydrodynamic properties of the working fluid, vapour temperature and pressure, inclination angle and mostly filling ratio [104]. The filling ratio of a thermosyphon represents the ratio of the volume of working fluid added to the volume of the evaporator section.

In order to design a thermosyphon, it is important to choose a suitable filling ratio that maximises the amount of heat transfer, while avoiding limitations including the dryout of the liquid film. This introduces the term ‘optimum filling ratio’. This term is described as the minimum amount of working fluid (or filling ratio) needed to achieve a complete continuous circulation of the vapour and liquid film within the thermosyphon for a specific heat input. Normally, an increase of the evaporator temperature causes the dryout phenomenom. This problem can be tackled by increasing the filling ratio at the evaporator. Compared to an optimum filling condition, the addition of more working fluid follows an increase in the thermal resistance as observed by Jouhara et al. [70].

Since the heat transfer coefficient (HTC) of the liquid film is significantly higher than that of the liquid pool, having a filling ratio above the optimum would decrease the liquid film length as the liquid pool height increases, hence decreasing the performance of the thermosyphon.

In general, more than 25% filling ratio is necessary in order to obtain a high heat transfer rate [105]. Naresh et al. [67] experimentally investigated the thermal performance of an internally finned thermosyphon. The thermosyphon was charged with water or acetone for three different filling ratios, 20, 50 and 80%. The test was carried out for power inputs between 50 and 275 W. Results showed that the 50% filling ratio was found to be the optimum. Paramatthanuwat et al. [106] also confirmed that a filling ratio of around 50% is considered as optimum and enhances the heat transfer rate.

During the charging process, and to compensate the amount of fluid that will be evaporated, an extra 10% of the volume was always added to obtain the correct filling ratio. A total amount of 230ml was injected inside each thermosyphon. This amount filled half of the evaporator section, giving a filling ratio of 50%. This filling ratio allowed the investigation of both nucleate pool and film boiling heat transfer mechanisms, as under a 100% filling ratio, a thermosyphon operates in a pool boiling condition, hence eliminating the nucleate film boiling heat transfer regime.

Based on the literature, a filling ratio of 50% was applied for all tests in order to avoid some limitations such as dry-out and Geyser boiling phenomena in the experiments, as these phenomena occur at a small or large filling ratio, respectively.

3.3.1.3. Working fluid selection

The selection of the working fluid was mainly based on the fluid availability, cost, heat input and compatibility with the pipe material. Four different fluids were tested, namely water, acetone, ethanol and toluene. For each test, the same amount of fluid was injected in the thermosyphon for a fair comparison with other working fluids.

Naresh et al. [67] experimentally investigated the thermal performance of a thermosyphon filled with two different working fluids, water or acetone. At lower heat input (175 W), acetone was found to perform better than water, this was due to the lower saturation temperature of the acetone. However, water performed better at higher power input where acetone undergoes dryout.

In the thermosyphon and in the absence of the wicking limit, the temperature drop may be significant. To control the issue, a good selection of the working fluid is important to minimise this temperature drop. A figure of merit is a scale introduced for thermosyphons to indicate the performance of the working fluid based on the number calculated from the following equation:

$$FOM = \left(\frac{h_{fg} \times k_l \times \rho_l}{\mu_l}\right)^{0.25} = \frac{Positive\ effect}{Negative\ effect} \tag{3.24}$$

The numerator represents all the properties of a specific fluid that have a positive effect on thermal performance, where the denominator represents an opposite effect

where k_l is the thermal conductivity, μ_l is the dynamic viscosity and h_{fg} is the latent heat of vaporisation of the fluid.

For optimum performance of the thermosyphon, the value of the figure of merit (FOM) should be maximised. It is good to note that the value of the FOM is relatively insensitive to the temperature, i.e for water, this number stays above 4000 for a temperature range of 0.01°C to 350°C [107].

Table 3.12 – Maximum TPCT figure of merit values for selected fluids [107]***.***

Fluid	Temperature (°C)	FOM$_{max}$ $(kg/K^{0.75}s^{2.5})$
Water	180	7542
Ammonia	-40	4790
Methanol	145	1948
Acetone	0	1460
Toluene	50	1055

Table 3.12 illustrates the maximum FOM value at various temperatures for different working fluids. This table gives an idea of the range of FOM number for the tested working fluids.

Table 3.13 – FOM for the tested fluids at 25°C.

Tested fluid	FOM $(kg/K^{0.75}s^{2.5})$
Water	4960.75
Acetone	1557.54
Ethanol	1242.22
Toluene	1133.65

Table 3.13 contains the calculated FOM for the four tested working fluids. The FOM was calculated based on a reference temperature of 25°C. It can be clearly seen that water outperforms all other working fluids based on its figure of merit. This will also be confirmed from the results shown in the following chapter.

3.3.1.4. Condenser

The tested thermosyphon was sealed at the bottom and a vacuum valve installed at the top of the condenser section (see Figure 3.25). The valve is there to fill the tube with the working fluid as well as eliminating any non-condensable gases each time a different test is carried out. A complete extraction of non-condensable gases was achieved by purging. The accumulation of non-condensable gases at the top of the thermosyphon decreases the effective length of the condenser which, in return, reduces the amount of the heat recovered, hence reducing the performance of the thermosyphon.

The condenser section of the tested pipe consisted of a 200mm length concentric tube acting as a cooling water jacket around the top section of the pipe. The inside wall water jacket design consisted of a helical path (Figure 3.26) to create a good mixing of the water flow and increase the contact surface area, hence enhancing the convective heat transfer coefficient. The fin height, thickness and pitch are 10, 1 and 5 mm, respectively (Table 3.14). The helical condenser was eliminated once the heat pipe was installed within the multi-pass heat exchanger.

Figure 3.25 – Top-view of the thermosyphon.

Figure 3.26 – Helical condenser.

Table 3.14 – Helical condenser dimensions.

Parameters	**Dimensions (mm)**
Fin pitch	5
Fin thickness	1
Fin height	10
Tube length	200
Finned tube length	160

3.3.1.5. Instrumentation and operations

As previously mentioned, Figure 3.24 shows a schematic diagram of the experimentally tested thermosyphon, including both hot and cold circuits. As can be seen from the hot circuit, a variac (Figure 3.27) was connected in parallel to a voltmeter (Figure 3.27), while connected in series to an ammeter (Figure 3.27). The variac was there to control the power supplied by the heaters.

Figure 3.27 – variac (left), ammeter and voltmeter (right).

On the other hand, the cold circuit for the condenser consisted of water at ambient temperature ≈15°C coming from the tank, flowing in a 13mm hose through the flow-meter where the flow rate was controlled and measured using an Omega FTB370 series turbine flow sensor connected to a 6-digit ratemeter for data display (see Figure 3.28). Thereafter, the water entered the condenser in a helical passage around the pipe and exited from the top, where the water was drained.

Figure 3.28 – Turbine flow sensor (left), ratemeter (right).

A total of 6 K-type thermocouples were installed at various locations along the outer wall of the thermosyphon to measure the temperature distribution. Three thermocouples were installed on the evaporator section as shown in Figure 3.24; this would give sufficient data on the boiling regime. One thermocouple was installed on the adiabatic section, this thermocouple was important in giving an indication of the saturation temperature of the pipe. Figure 3.29 shows how a thermocouple was installed on the thermosyphon surface. It can be clearly seen that the thermocouple’s head was installed in a small drilled hole half-way through the thickness of the pipe. This ensured an accurate reading of the wall temperature as it will be less affected by the heaters surrounding the thermocouples. The two remaining thermocouples were installed on the condenser, more specifically, at the water inlet and outlet of the heat sink.

The thermocouples were connected to a data logging station which recorded and stored the wall temperature on a personal computer for a certain duration of time. The data-logger was set to log the thermocouple readings every second over a time span of 25 minutes for each evaporator heat input and condenser mass flow rate combination. This duration of time was enough for all the thermocouple readings to reach a steady state condition where no change in temperatures took place at a specific location.

Figure 3.29 – Thermocouple/surface contact.

Experimentally, an accurate measurement of the evaporator and condenser temperatures is essential for an accurate determination of the thermal performance of the thermosyphon. After recording the thermocouple readings, characterising the thermosyphon temperatures becomes a relatively simple task. This is done by averaging the temperature of each thermocouple along each section. Although the thermosyphon was completely insulated by rockwool insulation material to reduce the heat loss by convection to the surroundings, heat losses were still possible. This made it somehow a more difficult task to accurately characterise the thermal power transfer (Q_{in}) for the thermosyphon. Therefore, and in order to gain confidence in the measured value of Q_{in} supplied by the heaters, an energy balance approach was performed. This approach compared the electrical power supplied to the evaporator and the heat recovered from the condenser through the cooling water.

The power supplied by the heaters to the evaporator was calculated by measuring both current and voltage, then multiplying them with each other as shown in equation (3.25)

$$Q_{in} = V \times I \tag{3.25}$$

where V is the voltage and I is the current.

On the condenser side, the heat was extracted by the cooling water and measured by performing a heat balance equation such that:

$$Q_{out} = \dot{m} \times c_p \times (T_{out} - T_{in}) \tag{3.26}$$

where $\dot{m}$ is the mass flow rate of the water entering the condenser measured by the flowmeter, c_p is the specific heat at constant pressure and $(T_{out} - T_{in})$ is the temperature difference between the inlet and outlet of the condenser.

3.3.1.6. Test plan

Two tests were carried out for the single thermosyphon: the first test (Test 1) was conducted at Econotherm (UK) Ltd. with the second one (Test 2) at the Centre of Sustainable Energy Use in Food Chains (CSEF), Brunel University London.

Test 1 was carried out to choose an optimum working fluid for the thermosyphon. Based on available working fluids, the thermosyphon was charged each time with a different working fluid. As previously mentioned, four different working fluids were tested: Water, Ethanol, Acetone and Toluene. Different fluids have different thermophysical properties and therefore different rates of heat transfer.

Table 3.15 – Test 1 plan for the single thermosyphon.

	160 V	**195 V**	**230 V**
0.0125 kg/s	0.0125 kg/s & 160 V	0.0125 kg/s & 195 V	0.0125 kg/s & 230 V
0.025 kg/s	0.025 kg/s & 160 V	0.025 kg/s & 195 V	0.025 kg/s & 230 V
0.05 kg/s	0.05 kg/s & 160 V	0.05 kg/s & 195 V	0.05 kg/s & 230 V

Table 3.15 shows the different combinations of evaporator heat input and condenser mass flow rate. A total of 9 tests were carried out for each fluid. The three different voltage sizes 160, 195 and 230 correspond respectively to a power of 600, 900 and 1300 W. on the condenser side, the water entering the condenser was varied between a small, medium and a maximum mass flow rate, respectively 0.01, 0.025 and 0.05 kg/s.

Table 3.16 – Test 2 plan for the single thermosyphon.

	100 V	**150 V**	**200 V**
0.03 kg/s	0.03 kg/s & 100 V	0.03 kg/s & 150 V	0.03 kg/s & 200 V
0.06 kg/s	0.06 kg/s & 100 V	0.06 kg/s & 150 V	0.06 kg/s & 200 V
0.09 kg/s	0.09 kg/s & 100 V	0.09 kg/s & 150 V	0.09 kg/s & 200 V

The second test (Test 2) was conducted to characterise the behaviour of water as the working fluid and to assess the compatibility between water and carbon-steel. Such a combination was not covered in the literature. Due to the limited budget available to cover a longer stay at Econotherm (UK) Ltd., test 2 was carried out in the CSEF laboratory at Brunel University.

Table 3.16 shows the different inlet conditions that were tested while carrying out the single thermosyphon experiment with water being the working fluid. The heaters were controlled by the variac where the voltage was changed from 100 to 200V at 50V increments. The mass flow rate of the water going through the condenser was controlled by a valve where the mass flow rate was changed from 0.03 to 0.09 at 0.03 kg/s increment, giving a total of 9 combinations of the tested inlet conditions.

3.3.2. Multi-pass test rig

The heat exchanger under investigation consisted of six thermosyphons installed vertically and arranged in two rows, each with three thermosyphons. The thermosyphon bundle was in a staggered arrangement on the evaporator (air) side and in an in-line arrangement on the condenser (water) side. As mentioned before, the unit under study was built by Econotherm (UK) Ltd., a small scale version of a real shell-and-tube heat exchanger with a Disk-and-Doughnut baffle arrangement currently on the market.

Prior to filling and sealing the thermosyphons, the six carbon steel thermosyphons went through a vigorous internal surface modification to enable the compatibility of carbon steel with water as the working fluid. The process that was done on the pipe internal wall is referred to as passivation and is well described by Reay et al. [108] where the oxidation on the inside surface of the pipe was achieved with superheated steam vapour during the charging process. The passivation process prevented the chemical interaction between the carbon steel wall and the water that undergoes continuous boiling/condensation cycles during operation, and ensured a prolonged operating life of the carbon steel thermosyphon.

As previously mentioned, the unit was manufactured with the same dimensions as were modelled theoretically. The TSHX was 2 m in length and each air pass covered 600 mm of the total length of the thermosyphons. A maximum of three air passes could be installed on the shell-side of the heat exchanger, giving a total length of 1.8 m for the evaporator and 200 mm for the condenser section. The thermosyphons had the same length as the TSHX and had an outside diameter of 28 mm and a wall thickness of 2.5 mm. The same amount of working fluid (water) was injected into each thermosyphon during the charging process, filling each thermosyphon to a height of 600 mm giving a total volume of 250 ml. Two different multi-pass configurations of the unit were tested as follows:

- Case 2, two air passes
- Case 3, three air passes

The thermosyphon condenser sections were installed in a U-shaped (2-pass) flow passage (Figure 3.30), where the purple arrow indicates the water flow direction.

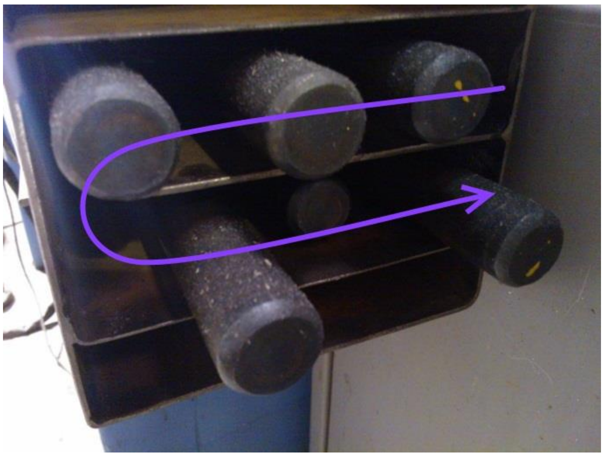

Figure 3.30 – Top view U-shaped condenser.

Figure 3.31 shows the three different configurations of the test unit at Econotherm (UK) Ltd. The air flow in each case is indicated by a black arrow. The TSHX under investigation was well insulated to minimise heat loss in order to achieve, to a reasonable extent, the boundary conditions assumed during the numerical modelling, where external walls were taken to be adiabatic.

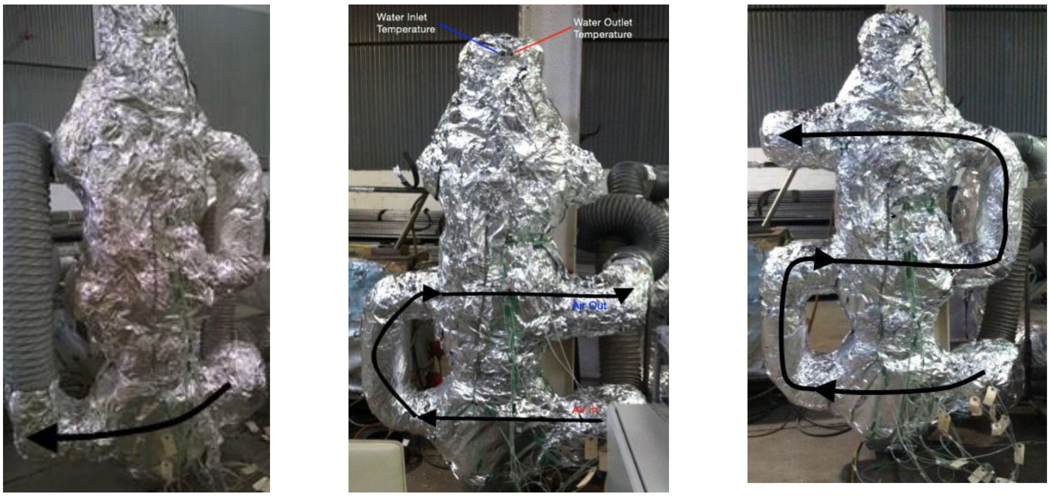

Figure 3.31 – One, two and three air passes (left to right).

3.3.2.1. Operational procedure

The TSHX operated between two different fluid circuits, namely a hot air circuit and a cold water circuit. In Figure 3.32, the hot side is represented by solid lines while the cold side in shown by dashed lines. The air flow was generated by a variable frequency fan and four different flow rates were considered: 10, 20, 30 and 40 HZ corresponding to 0.05, 0.08, 0.11 and 0.14 kg/s, respectively. During the analysis of the test results, it was observed that the results at both extremes, 50 and 300°C, showed inconsistency compared to other inlet conditions. This was due to the instability of the boiling regime at a very low and a very high evaporator inlet temperature. For this reason, the conditions mentioned were excluded from the analysis.

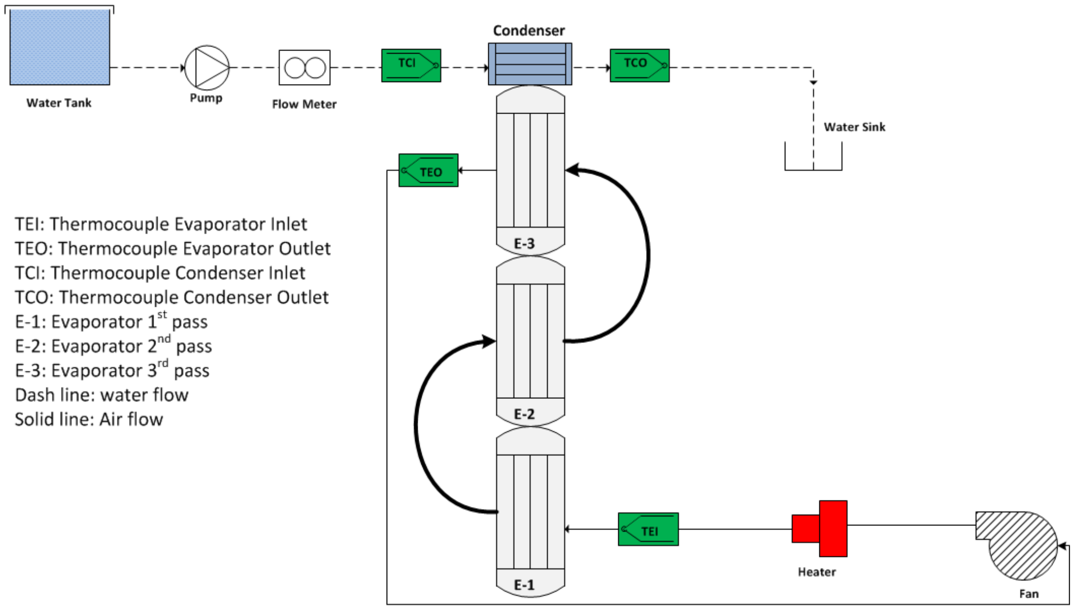

Figure 3.32 – Air (evaporator) and water (condenser) circuit.

The fan blew the air into the heater, where its temperature was controlled by a thermocouple feedback loop. The temperature of the hot air entering the HX was varied between 50°C and 300°C in steps of 50°C (Table 3.17). The air was then forced to enter the shell-side first air pass, flowing across the staggered tube bundle where heat was absorbed by the thermosyphons. Passes were connected by elbows, directing the air flow externally in U-shaped passages, with the hot air crossing the tube bundle once in each pass. Finally, the hot air exited the HX and returned to the fan in a closed loop circuit. Table 3.17 represents all the different combinations, 16 in total, of air inlet flow rates and temperatures that have been conducted during the test.

Table 3.17 – Test plan for the TSHX for all cases.

	10 HZ	**20 HZ**	**30 HZ**	**40 HZ**
50°C				
100°C	10HZ & 100°C	20HZ & 100°C	30HZ & 100°C	40HZ & 100°C
150°C	10HZ & 150°C	20HZ & 150°C	30HZ & 150°C	10HZ & 150°C
200°C	10HZ & 200°C	20HZ & 200°C	30HZ & 200°C	10HZ & 200°C
250°C	10HZ & 250°C	20HZ & 250°C	30HZ & 250°C	10HZ & 250°C
300°C				

Water was the fluid medium on the condenser side used to recover the heat absorbed by the evaporator section. Water was initially located in a tank at an ambient temperature of approximately 15°C and then pumped through a flow meter before flowing at a rate of 0.08 kg/s around the thermosyphons, one by one in an in-line configuration (Figure 3.30).

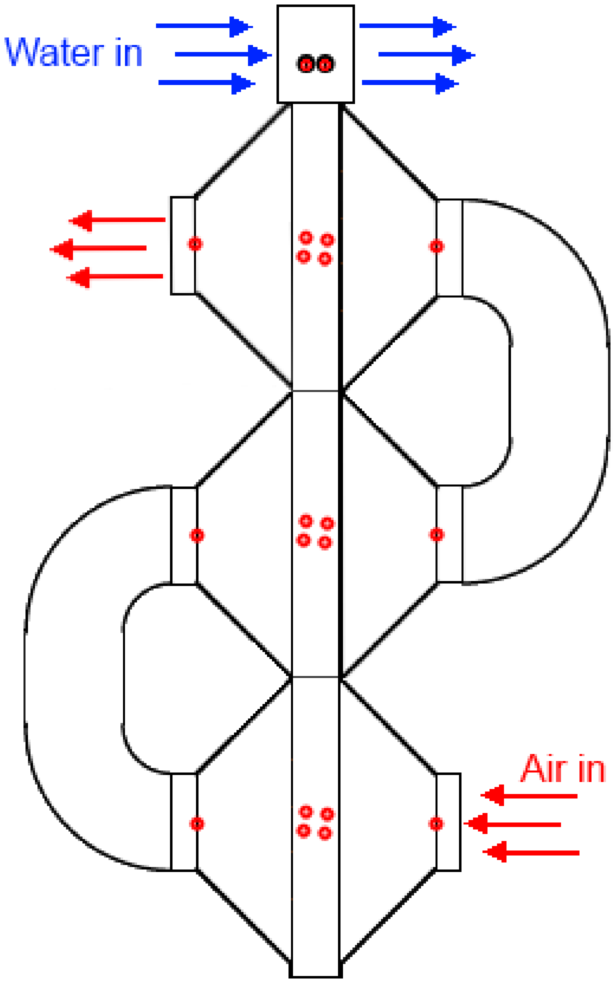

Figure 3.33 – Thermocouple locations (each red dot represents a K-type thermocouple).

A total of 22 K-type thermocouples were installed at various locations across the test unit, at the inlet and outlet of each air pass and at the inlet and outlet of the cooling water (Figure 3.33). Thermocouples were also brazed on the outer surface of the thermosyphons in each air pass (Figure 3.34).

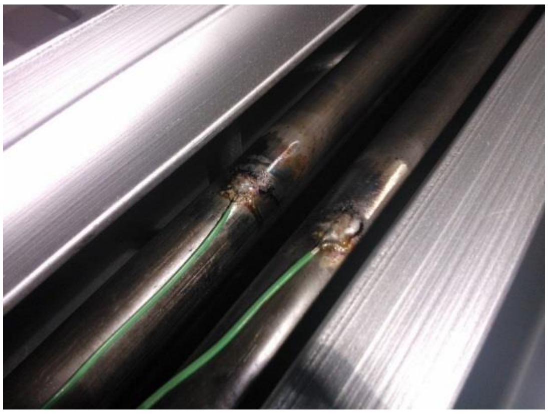

Figure 3.34 – Brazed thermocouple on thermosyphon outer wall.

3.3.3. Uncertainty analysis

No physical quantity can be measured with certainty, and measurements always contain errors. Such errors can propagate through an experimental procedure due to many factors mainly human error, equipment usage and inaccurate experiment set-up.

The thermocouples were most likely the main source of errors in the experiment conducted. An uncertainty study was carried out to investigate the error propagation on the heat recovered by the condenser at the two extreme air inlet temperatures (100°C and 250°C) for the multi-pass. The uncertainty in the heat transfer recovered in the condenser was calculated using equations (3.27) and (3.28), where the uncertainty associated with the temperature reading is estimated to be ±0.05% of the reading plus 0.3°C and that in the flowmeter reading 2%:

Table 3.18 – Equations used for the uncertainty calculation.

Mathematical Operation	**Associated Error**	
Multiplication/ Division	$\mathrm{S}_{\dot{\mathrm{Q}}_\mathrm{c}} = \dot{\mathrm{Q}}_\mathrm{c}\sqrt{\left(\frac{\mathrm{S}_{\mathrm{FR}_\mathrm{w}}}{\mathrm{FR}_\mathrm{w}}\right)^2 + \left(\frac{\mathrm{S}_{\Delta\mathrm{T}_\mathrm{c}}}{\Delta\mathrm{T}_\mathrm{c}}\right)^2}$	(3.27)
Addition/ Subtraction	$\mathrm{S}_{\Delta\mathrm{T}_\mathrm{c}} = \sqrt{\left(\mathrm{S}_{\mathrm{T}_\mathrm{c,o}}\right)^2 + \left(\mathrm{S}_{\mathrm{T}_\mathrm{c,i}}\right)^2}$	(3.28)

Table 3.18 shows an example on how the uncertainty of the heat transfer rate is computed for the multi-pass TSHX and the single thermosyphon. In the above equations, $S_{\dot{Q}_c}$ is the associated error calculated based on the uncertainty of the volume fraction (mass flow rate) and the uncertainty of the temperature difference as shown in equation (3.27). In addition and as seen from equation (3.28), the associated error of the temperature difference is based on both associated errors of the condenser water inlet and outlet temperatures. The remaining equations are listed in Appendix C.

Once the associated error of the heat transfer rate $S_{\dot{Q}_c}$ is computed, the uncertainty will be calculated as follow:

$$Uncertainty = \frac{S_{\dot{Q}_c}}{\dot{Q}_c} \qquad (3.29)$$

Chapter 4. RESULTS AND DISCUSSIONS

4.1. Single thermosyphon results

The following section analyses the results generated from the two tests of the single thermosyphon. The first test (test 1) consisted of evaluating the thermal performance of the thermosyphon for different evaporator and condenser inlet conditions where four different working fluids were experimentally tested. The thermosyphon was charged with water, acetone, toluene and ethanol for each test. A second test (test 2) was also carried out, however, to investigate the choice of a boiling correlation to be used in theoretical modelling procedure. Test 2 was conducted at different evaporator and condenser inlet conditions. A few well-known boiling correlations were tested for a range of testing conditions. A correlation must satisfy the combination of carbon-steel as the thermosyphon shell material with the best performed working fluid from test 1.

4.1.1. Thermosyphon Test 1

The first single thermosyphon test was conducted at different evaporator heating inputs, where the power of the heater was set to produce three different heat transfer rates: 600, 900 and 1300 W. On the condenser side, the mass flow rate of the water cooling was halved twice, starting with a maximum flow rate of 0.05 kg/s, followed by a flow rate of 0.025 kg/s and finally 0.0125 kg/s.

Figure 4.1 to Figure 4.4 show the thermal behaviour of the tested thermosyphon under the different heating inputs and cooling water mass flow rates. A similar behaviour of the various working fluids has been observed. More specifically, a higher performance is observed at higher cooling water flow rates and evaporator input power. However, the trend of the graph can be imperfect at some conditions; this could be mainly due to the uncertainty that exists within the instrumentation used to collect the data: thermocouples, flow meter, voltmeter etc.

The performance of the working fluids was each compared to an "ideal" thermosyphon when operated with zero uncertainty and heat losses. Q_{in} represents the evaporator applied heat transfer rate while Q_{out} represents the condenser heat recovered by the cooling water. As it can be seen from Figure

4.1 to Figure 4.4, all the results fall below the straight line y=x (“ideal”). This explains that the heat recovered from the condenser was always less than the heat supplied to the evaporator as 100% insulation can never be achieved, though it can be minimised. At higher evaporator heat inputs, the heat loss was larger, observed by the wider deviation from the line y=x.

Looking at the comparison between the performances of the four working fluids in Figure 4.4, it can be clearly seen that water outperformed the other three working fluids. This was also observed in chapter 5 with the value of FOM that was calculated and discussed for all the working fluids.

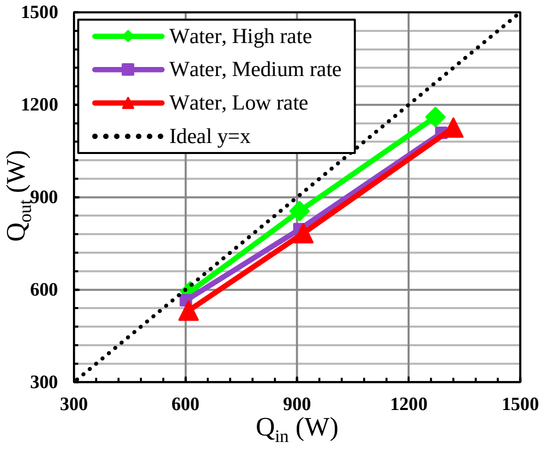

Figure 4.1 – Water as the working fluid at different inlet conditions.

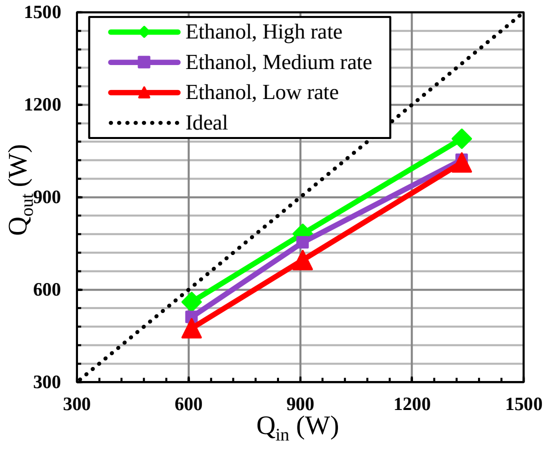

Figure 4.2 – Ethanol as the working fluid at different inlet conditions.

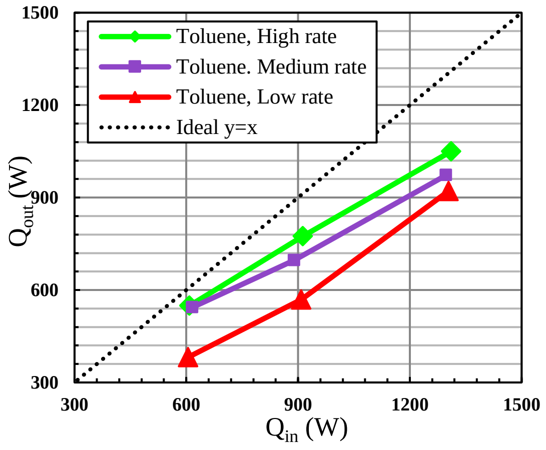

Figure 4.3 – Toluene as the working fluid at different inlet conditions.

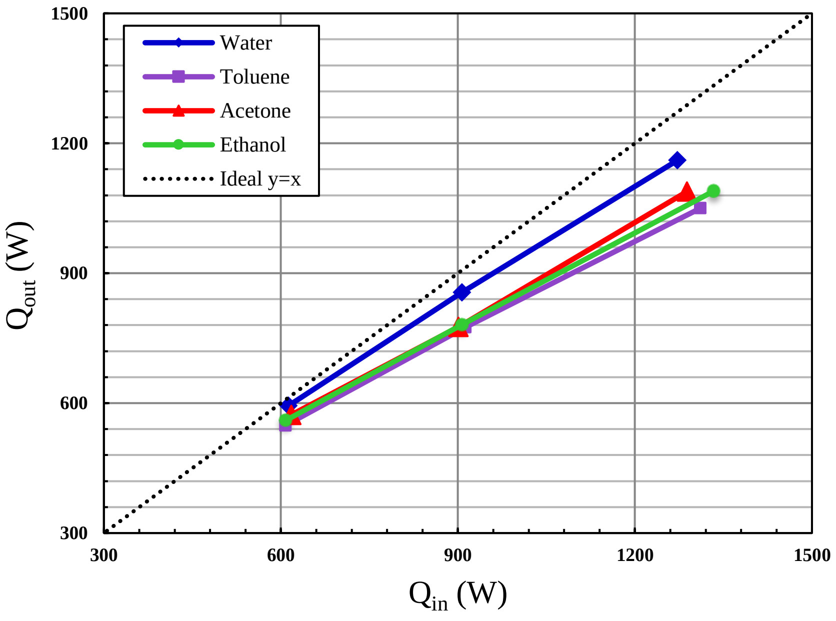

Figure 4.4 – Comparison between the four working fluids (at high flow rates).

4.1.2. Thermosyphon Test 2

As mentioned before, Test 2 was carried out to develop an understanding of how the single thermosyphon operates in pool boiling mode with water as the working fluid after it was shown to have a better thermal performance than the other working fluids tested. However, the aim was not to perform extensive comparisons of all pool boiling correlations. Instead, the analysis was focused on discussing the applicability of a small portion of the pool boiling correlations that are frequently used in thermosyphon publications. Eventually, one pool boiling correlation was chosen to be used in the theoretical modelling of the multi-pass as a whole heat exchanger system.

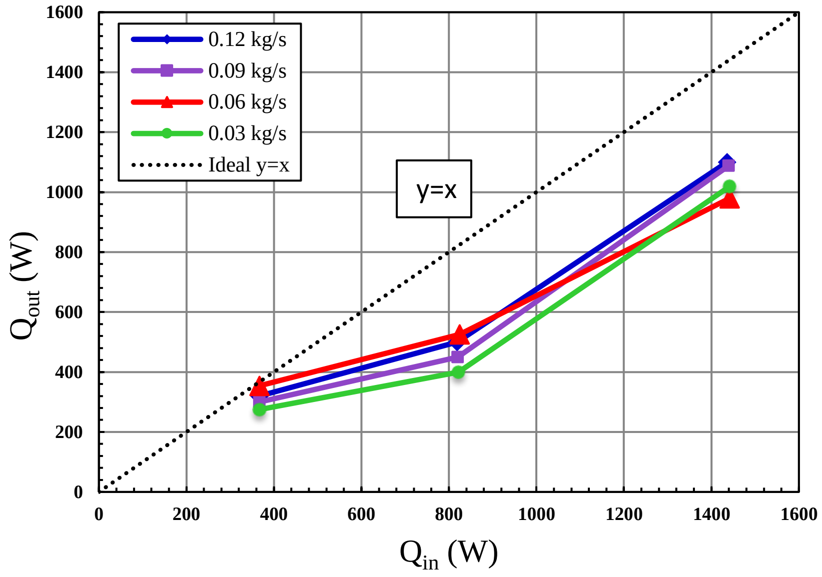

Figure 4.5 – Single thermosyphon behaviour with water as the working fluid for different inlet conditions.

Figure 4.5 shows the behaviour of the single thermosyphon for different water cooling flow rates, which ranged between 0.03 and 0.12 kg/s at 0.03 kg/s increments. The trend for all testing conditions is almost the same except for the flow rate of 0.06 kg/s, where a measurement error is expected to have occurred during the test. Instead, the trend for 0.06 kg/s should be between 0.03 and 0.09 kg/s as the higher the mass flow rate of the cooling fluid, the higher the heat recovered. A maximum heat transfer rate of around 1100W was observed at a combination of maximum flow rate (0.12 kg/s) and evaporator heat input (1442W).

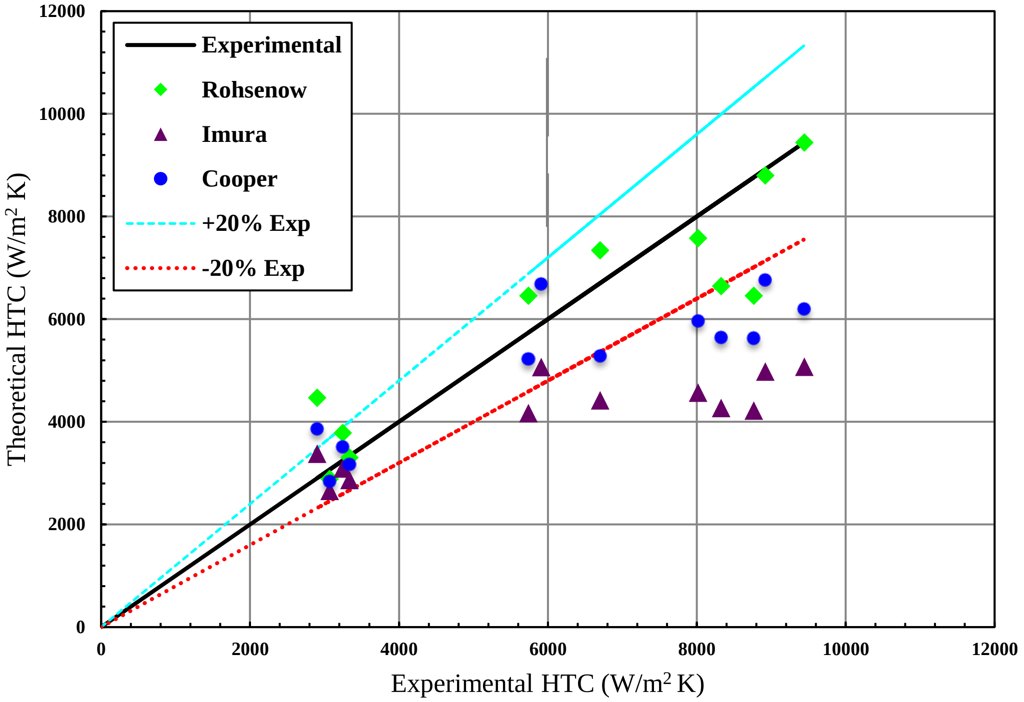

Figure 4.6 – Experimental HTC vs theoretical HTC.

The convective heat transfer coefficient (HTC) was calculated for different pool boiling correlations that are extensively used in the literature [70,109,110]. Such correlations include Rohsenow, Cooper and Imura. A graph was generated in Figure 4.6 to compare the experimental heat transfer coefficient calculated through equation (4.1), and the theoretical HTC is predicted using well-known correlations which are listed in Table 5 (chapter 3).

$$q_e = h_{pb} \times A_e \times (T_{e,in} - T_{sat})$$

Rearranging for h_{pb}:

$$h_{pb} = \frac{q_e}{A_e \times (T_{e,in} - T_{sat})} \tag{4.1}$$

where h_{pb} is the pool boiling heat transfer coefficient, A_e is the evaporator heat transfer area and $(T_{e,in} - T_{sat})$ is the temperature difference between the evaporator inlet wall and the thermosyphon working (saturation) temperature.

It can be clearly seen from Figure 4.6 that the theoretical (predicted) HTC using the Rohsenow pool boiling correlation has the same trend as the experimental one. Moreover, the majority of the testing conditions lie within 20% of the experimental results, demonstrating that Rohsenow pool boiling correlation is reliable to be used in the theoretical modelling of the thermosyphon heat exchanger (TSHX).

Rohsenow [93] has proposed that the pool boiling heat transfer enhancement phenomenon is caused by a continuous local liquid circulation near the heated surface, followed by successive bubble detachments. After some manipulation, Rohsenow managed to relate all the parameters affecting the pool boiling regime based on the mass velocity of vapour leaving the heated surface and bubble detachment diameter [111]. The equation is listed below:

$$\frac{c_{p,l} \times \Delta T}{h_{lv}} = C_{sf} \times \left\{\frac{\dot{q}}{h_{lv} \times \mu_l} \times \left[\frac{\sigma}{g \times (\rho_l - \rho_v)}\right]^{0.5}\right\}^{m} \times \left(\frac{c_{p,l} \times \mu_l}{k_l}\right)^{n} \quad (4.2)$$

As it can be seen from equation (4.2), the correlation is based on a constant C_{sf} and two exponents n and m. Other than water, the values of the two exponents n and m were found to be 1.7 and 0.33 through fitting curves to experimental results. According to Rohsenow, the value of n should be changed to 1 in the case of water being the working fluid.

Table 4.1 – Values of Rohsenow parameters for various water-surface combinations.

Surface	$C_{sf}/n/m$	**References**
Polished copper	0.0128/1.7/0.33	[89]
Lapped copper	0.0147	[112]
Scored copper	0.0068/1.7/0.33	[113]
Ground and polished stainless steel	0.008/1/0.33	[114]
Teflon-pitted stainless steel	0.0058	[112]
Chemically etched stainless steel	0.0133	[112]
Mechanically polished stainless steel	0.0132	[112]
Polished platinum	0.013/1/0.33	[93]
Polished tube/ brass	0.009/1.1/0.33	[114]

As mentioned before, the pool boiling correlation of Rohsenow relies on an adjustable surface/fluid parameter named C_{sf}, a constant depending on the surface finish of the inner evaporator wall and the working fluid. Table 4.1 shows various C_{sf} values for a few water-surface combinations. It is evident that this value is significantly affected by the surface finish of the metal. Usually, in practice, the value of this constant is unknown and has to be guessed. As a first approximation, a value of 0.013 is recommended [96]. In addition to justifying the use of Rohsenow's pool boiling correlation, test 2 allowed the prediction of a new value of C_{sf} for future analysis of thermosyphons made out of carbon steel and charged with water. The prediction of the value of C_{sf} for such combination was never covered in the open literature. Using the trial and error method, a C_{sf} value of 0.05 was eventually found to correlate the predicted HTC with the experimental HTC. The use of such a value does not perfectly predict the measured value of HTC; however it does provide a reasonable agreement over the entire tested range. The predicted constant is used in the theoretical modelling process of the multi-pass heat exchanger.

4.2. Multi-pass results

In order to gain confidence in the numerical tool modelled in ANSYS Fluent, it was important to generate experimental results by running the whole TSHX system. The experimental results will be compared to the numerical results generated in Fluent and, if the validation lies within an acceptable accuracy, then the numerical tool will be trusted and taken forward for further investigation. The validation will be based on comparing the heat transfer rate for the whole TSHX system at different inlet conditions for the two multi-pass configurations (case 2 & 3).

To obtain a validated model, the following conditions on both CFD and experiment were taken into account:

- The same geometrical dimensions were applied
- The comparison was made for the same inlet conditions
- A steady state condition was always ensured for each test
- During the experiments, the TSHX was well insulted to minimise heat losses as a 100% adiabatic condition was assumed in the modelling
- The same mesh parameters were applied for all the cases

4.2.1. Experimental validations and comparison

Figure 4.7 to Figure 4.9 compare the theoretical results, CFD and experimental data at different air inlet temperatures and mass flow rates where the lowest and highest heat transfer rates occur at the following combinations of air inlet conditions: (0.05kg/s, 100°C) and (0.14kg/s, 250°C), respectively. Not surprisingly, the highest rate of heat transfer occurred with the highest values of air inlet parameters for case 3, while the lowest rate of heat transfer occurred at the lowest values of these parameters for case 1.

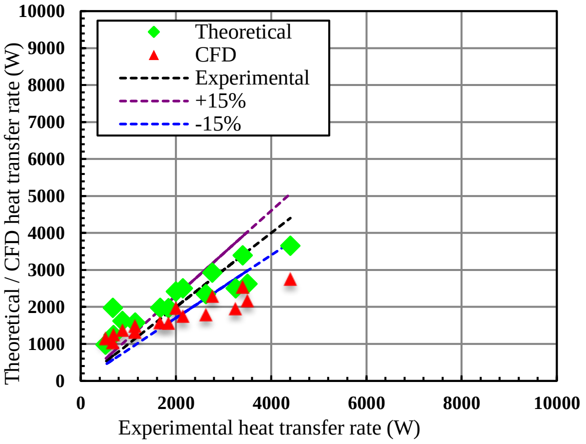

Figure 4.7 – Comparison between experimental, theoretical and CFD results (case 1).

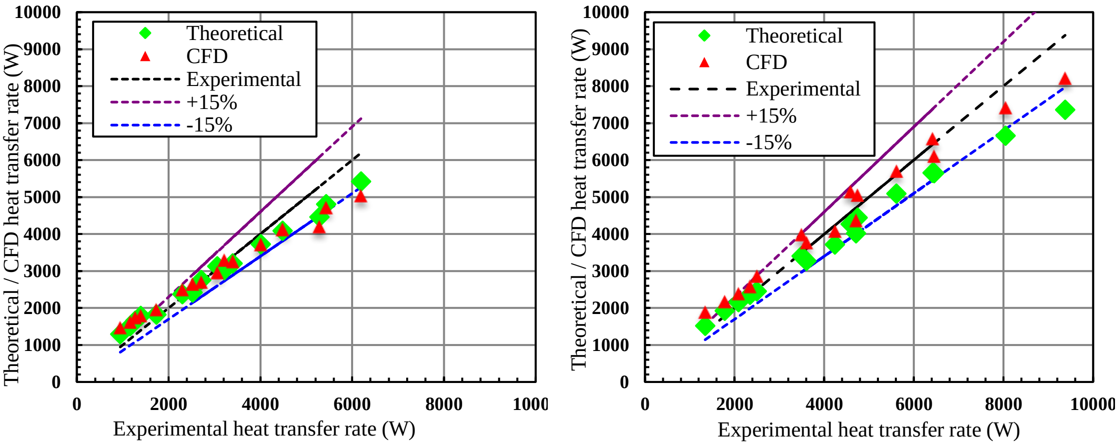

Figure 4.8 – Comparison between experimental, theoretical and CFD results (case 2).

Figure 4.9 – Comparison between experimental, theoretical and CFD results (case 3).

As stated in the previous chapters, a theoretical model of all cases was developed using existing correlations available in the literature and these have been previously used by many researchers, including Ramos et al. [17] and Mroue et al. [18], and shown to be reasonably accurate. Correlations from Zhukauskas, Rohsenow and Nusselt [84,85] were used to model the convection, boiling and condensation heat transfer mechanisms inside and outside the thermosyphons. The overall heat transfer rate was then calculated and compared with experimental and numerical (CFD) results. It can be clearly seen that the majority of the CFD and theoretical results lie within a 15% envelope of the experimental heat transfer.

Looking at Figure 4.7 to Figure 4.9, the CFD and theoretical heat transfer rates closely follow the experimental line y=x (black) at low values of air inlet parameters. The percentage error increases at higher values. This can be due mainly to the lack of information on turbulence. The value of the turbulence intensity of both air and water could improve the results once implemented in Fluent. As mentioned before, the turbulence intensity of both air and water was kept at the 5% default value. However, increasing the mass flow rate or the inlet air temperature will lead to higher turbulence and, therefore, higher convective heat transfer which was not taken into account in the simulation.

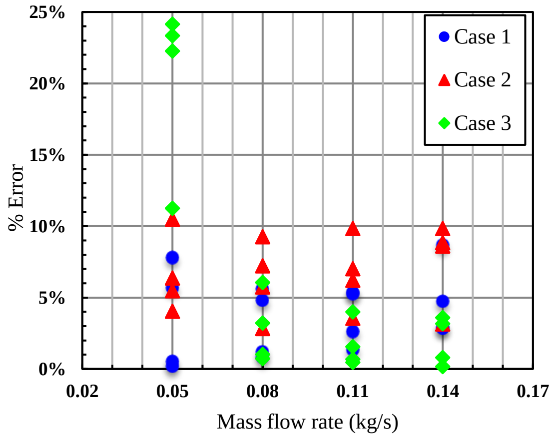

Figure 4.10** – **Percentage error of the <u>evaporator</u> outlet temperature at different air mass flow rates.

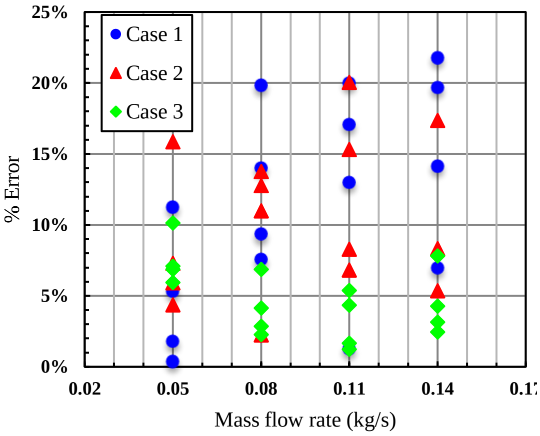

Figure 4.11 – Percentage error of the condenser outlet temperature at different air mass flow rates.

Figure 4.10 and Figure 4.11 show the percentage error between experimental and CFD results for the outlet temperature on the evaporator and condenser sections at different inlet conditions. For the three cases, the figures have shown that the majority of the results lie within a 15% envelope as mentioned before.

Another comparison has been made between CFD and experimental results on the outlet temperature of both evaporator and condenser. The comparison is illustrated from Figure 4.12 to Figure 4.17. The line y=x represents the best fitting correlation between both CFD and experimental results. The CFD results show a slight overestimation of the outlet temperature of the evaporator, but this was expected as the CFD imposes a 100% adiabatic wall whereas, in reality, complete insulation is hardly achieved.

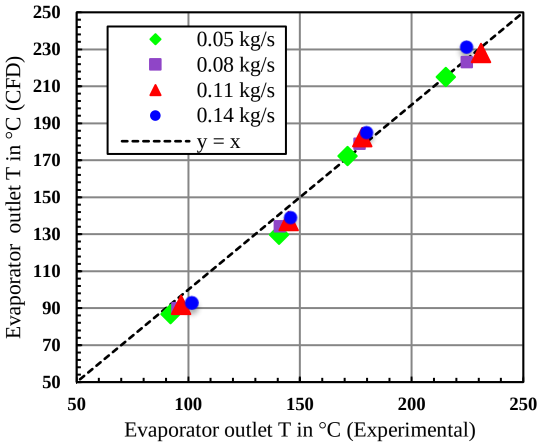

Figure 4.12 – Evaporator outlet temperature for CFD and experimental at different inlet conditions (case 1).

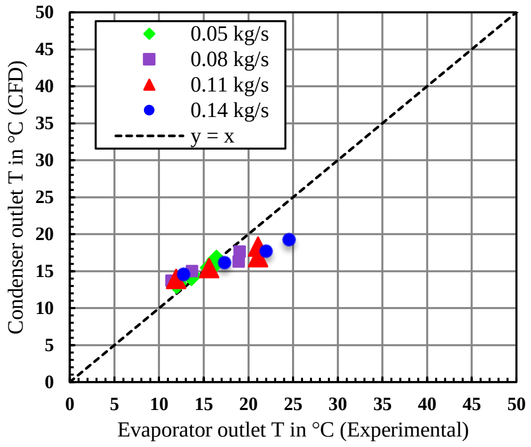

Figure 4.13 – Condenser outlet temperature for CFD and experimental at different inlet conditions (case 1).

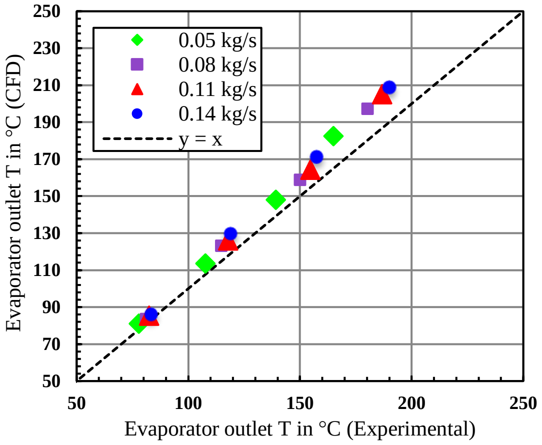

Figure 4.14 – Evaporator outlet temperature for CFD and experimental at different inlet conditions (case 2).

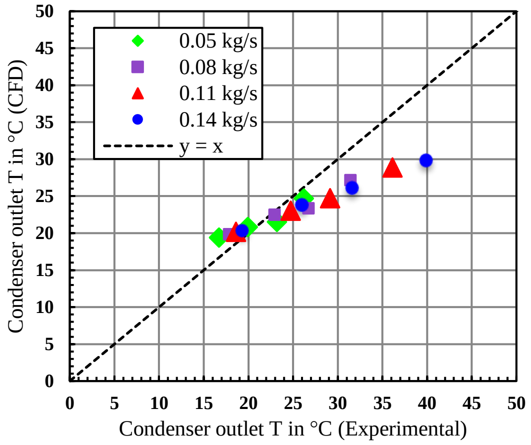

Figure 4.15 – Condenser outlet temperature for CFD and experimental at different inlet conditions (case 2).

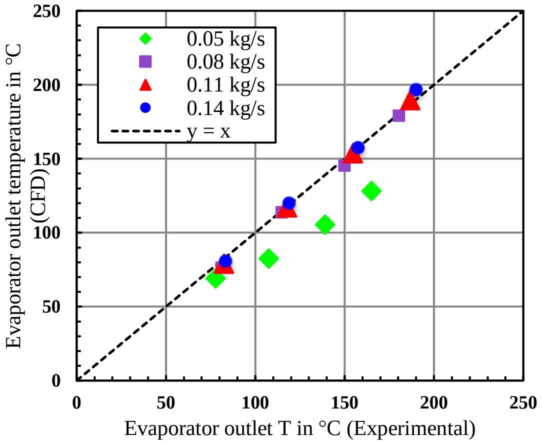

Figure 4.16 – Evaporator outlet temperature for CFD and experimental at different inlet conditions (case 3).

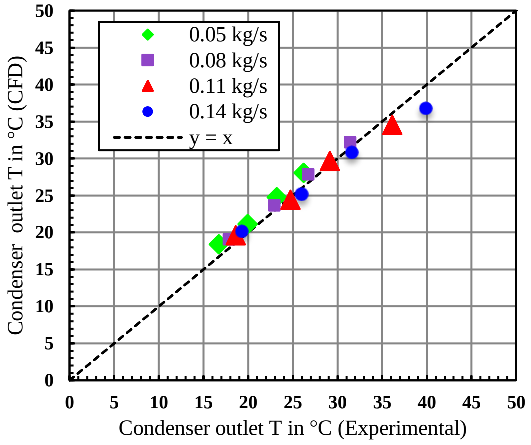

Figure 4.17 – Condenser outlet temperature for CFD and experimental at different inlet conditions (case 3).

4.2.2. Experimental results

A plot of the temperature versus the mass flow rate was created for both multi-pass cases to ensure the results were consistent. Figure 4.18 to Figure 4.25 show the temperature of the flow at the inlets and outlets of the evaporator and condenser sections of the heat exchanger. It can be observed that the duty of the heat exchanger increases at higher mass flow rates and higher inlet temperatures, shown by the greater temperature difference on the water side at higher temperatures and mass flow rates. The same behaviour was observed for the two multi-pass configurations.

At lower flow rates, the pipe is given more time to absorb the heat and that is reflected in an increase of the temperature difference across the evaporator, but as has been mentioned before, this does not reflect an increase in the duty or total heat transfer rate, shown in Figure 4.26 and Figure 4.27. In other words, increasing the evaporator mass flow rate leads to a lower temperature difference across the evaporator, however, a higher heat transfer as the mass flow rate has greater influence on the duty than the temperature difference.

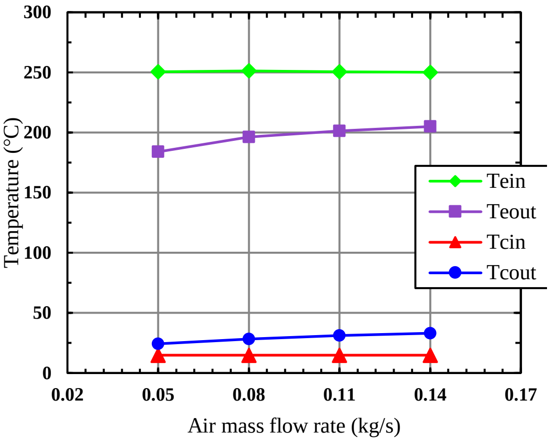

Figure 4.18 – Temperature distribution along the heat exchanger for 250 °C inlet temperature (case 2).

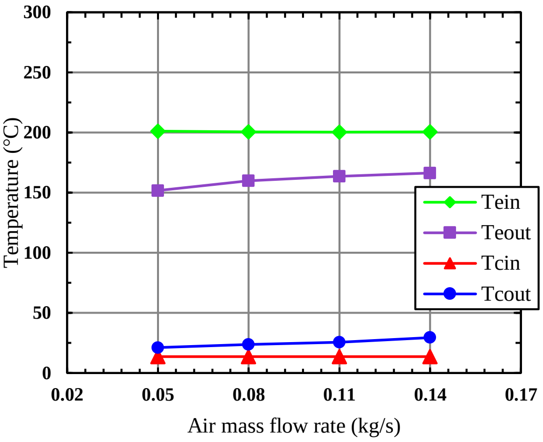

Figure 4.19 – Temperature distribution along the heat exchanger for 200 °C inlet temperature (case 2).

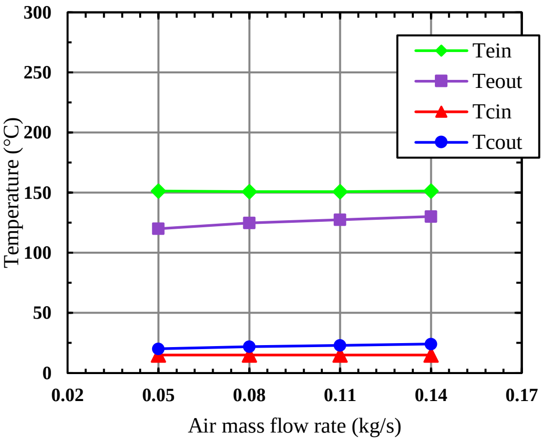

Figure 4.20 – Temperature distribution along the heat exchanger for 150 °C inlet temperature (case 2).

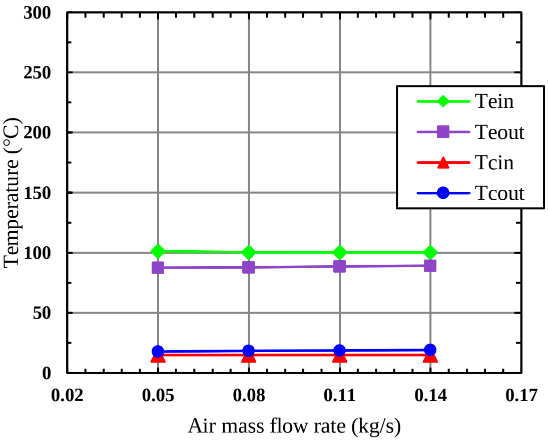

Figure 4.21 – Temperature distribution along the heat exchanger for 100 °C inlet temperature (case 2).

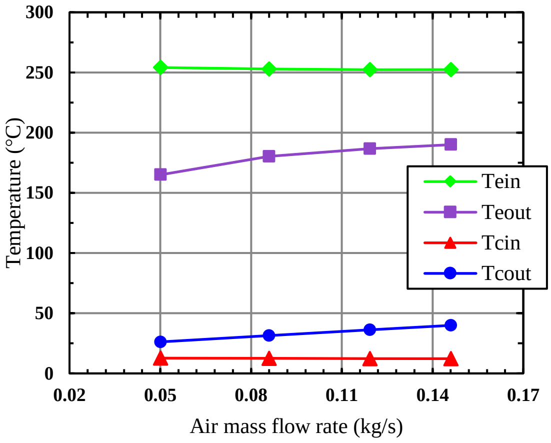

Figure 4.22 – Temperature distribution along the heat exchanger for 250 °C inlet temperature (case 3).

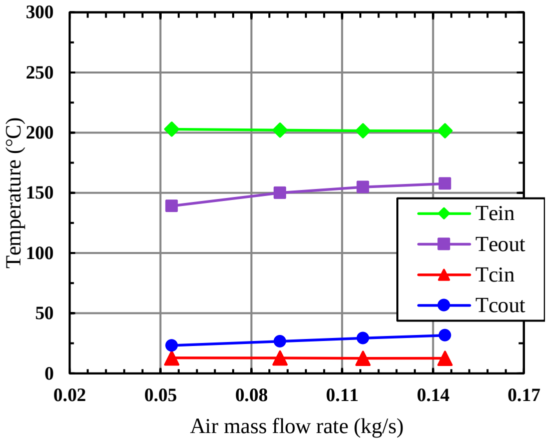

Figure 4.23 – Temperature distribution along the heat exchanger for 200 °C inlet temperature (case 3).

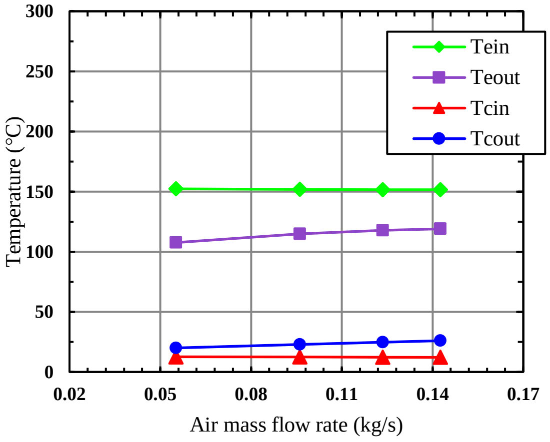

Figure 4.24 – Temperature distribution along the heat exchanger for 150 °C inlet temperature (case 3).

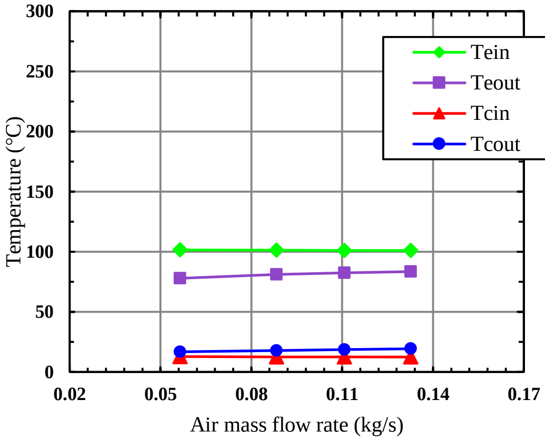

Figure 4.25 – Temperature distribution along the heat exchanger for 100 °C inlet temperature (case 3).

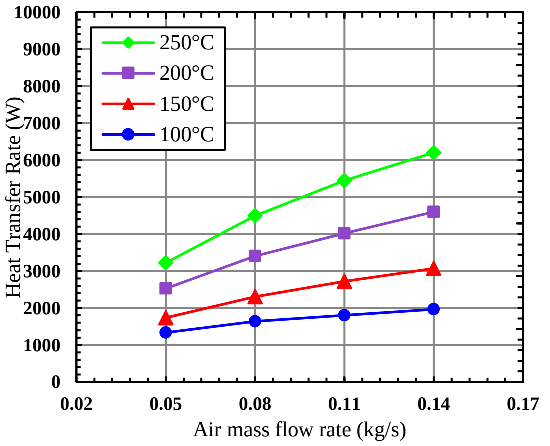

Figure 4.26 – Heat Transfer Rate of the Heat Exchanger according to the inlet conditions (case2).

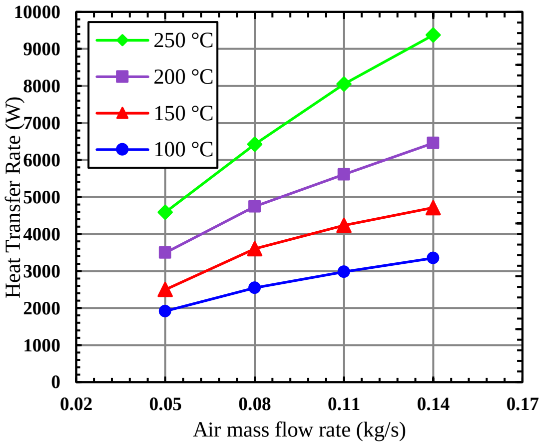

Figure 4.27 – Heat Transfer Rate of the Heat Exchanger according to the inlet conditions (case 3).

Figure 4.29 to Figure 4.32 compare the working temperature of the heat pipes for each inlet condition. Four thermocouples were brazed on the outer wall of the thermosyphon at a height of 1.5 m measured from the bottom of the pipe. Basically, the thermocouples were placed in the adiabatic section of the pipe (technically the third pass for case 3). The temperature measured in the adiabatic section is used as the saturation/working temperature of the pipe. The working temperature increased with the increase in mass flow rate and inlet temperature at the evaporator section, as expected. However, there was a difference in temperature between each individual pipe. The pipes were numbered in accordance to the diagram in Figure 4.28.

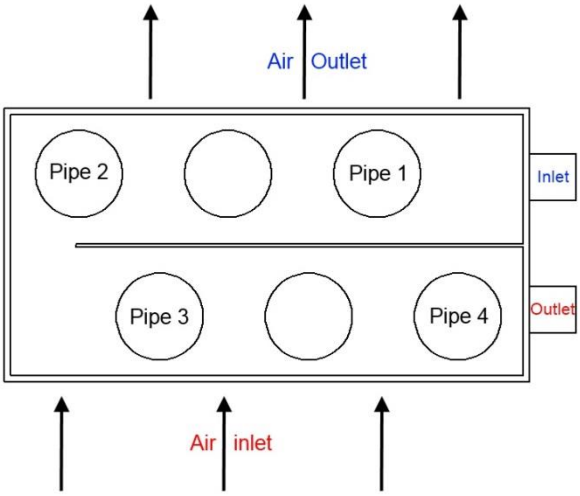

Figure 4.28 – Pipe numbering.

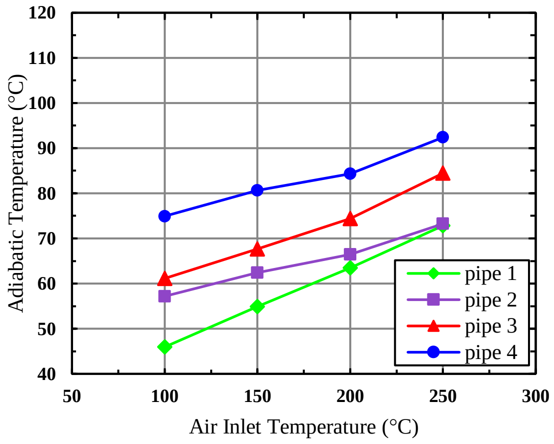

Figure 4.29 – Working temperature of each pipe for different inlet temperatures and 0.05 kg/s (case 2).

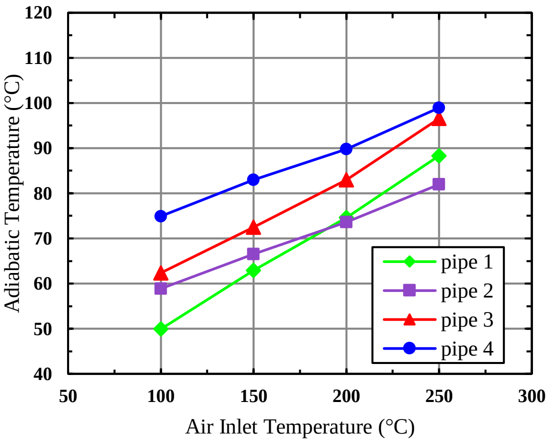

Figure 4.30 – Working temperature of each pipe for different inlet temperatures and 0.08 kg/s (case 2).

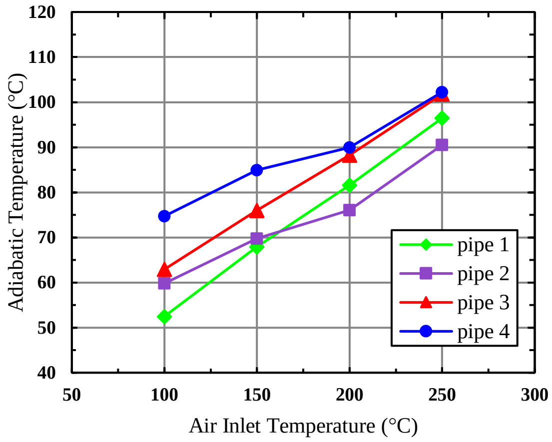

Figure 4.31 – Working temperature of each pipe for different inlet temperatures and 0.11 kg/s (case 2).

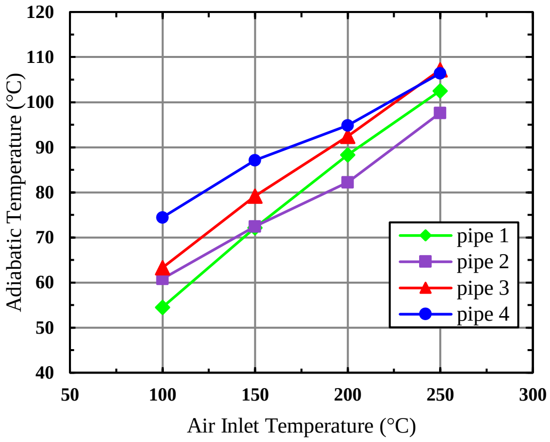

Figure 4.32 – Working temperature of each pipe for different inlet temperatures and 0.14 kg/s (case 2).

It can be observed that the heat pipe with the highest average working temperature was pipe 4; it is located on the row of pipes that first made contact with the hot flow at the first pass and it is the heat pipe farthest away from the condenser inlet. After pipe 4, all the pipes followed in the inverse order to the condenser section, therefore 3 had the next highest average temperature, followed by 2 and 1, the closest to the condenser inlet. Pipes 1 and 2 are located on the first row of the second pass in the evaporator section.

With the increase in mass flow rate, the temperatures became more similar to one another but it can still be observed that the average working temperature of pipes 3 and 4 was higher at lower air inlet temperatures. This was due to a combination of factors. Firstly, as can be observed in Figure 4.28 and has been mentioned before, pipes 3 and 4 are on the first row that cames into contact with the evaporator inlet. Secondly, they are also located the farthest away from the condenser inlet, receiving warmer water at the condenser side, which resulteds in a lower difference in temperature between the bottom and the top of the heat pipe, maintaining higher working fluid temperature.

Figure 4.33 to Figure 4.40 show the heat transfer rate (Q) across each air pass for both multi-pass configurations (case 2 and 3) of the heat exchanger unit for each different inlet condition. Total represents the total heat transfer rate taking into account both air passes. The trend is for the temperature difference across the first pass to be larger than the second and the third pass due to a higher difference in temperature between the incoming flow and the working temperature of the pipes, therefore higher heat transfer rates. Increasing the inlet air temperature results in a higher temperature difference across each pass and therefore an increase in the heat transfer rate. Likewise, increasing the mass flow rate increases the overall turbulence, also having the effect of increasing the overall heat transfer rate.

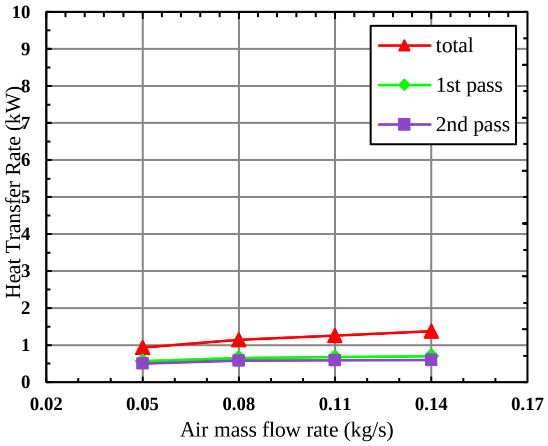

Figure 4.33 – Heat transfer rate for different flow rates at 100°C air inlet temperature (case 2).

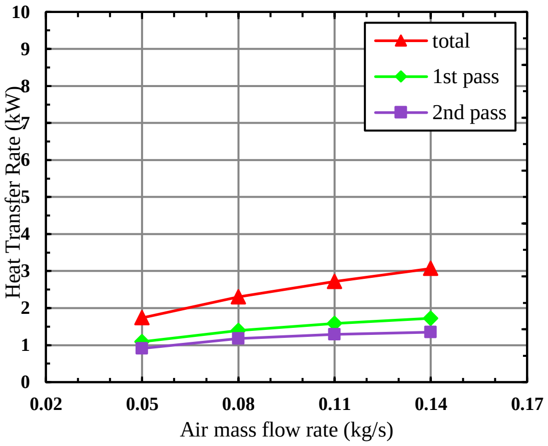

Figure 4.34 – Heat transfer rate for different flow rates at 150°C air inlet temperature (case 2).

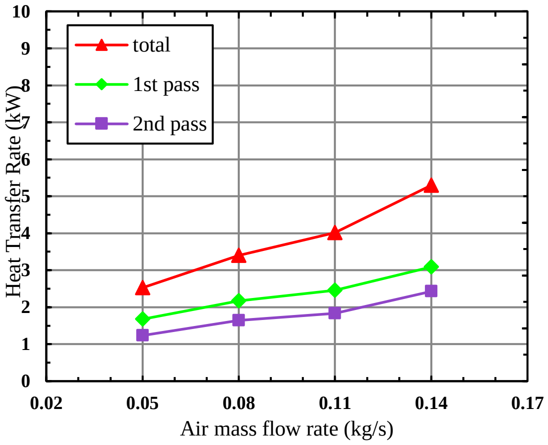

Figure 4.35 – Heat transfer rate for different flow rates at 200°C air inlet temperature (case 2).

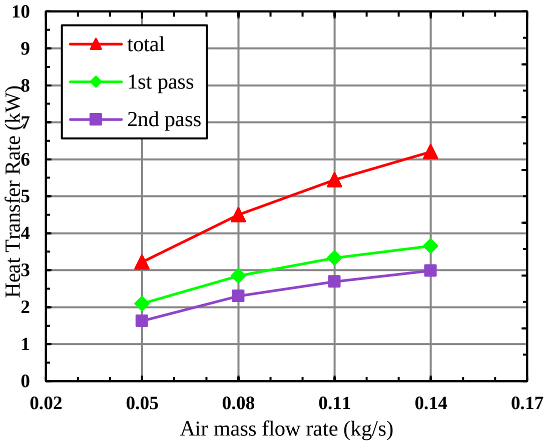

Figure 4.36 – Heat transfer rate for different flow rates at 250°C air inlet temperature (case 2).

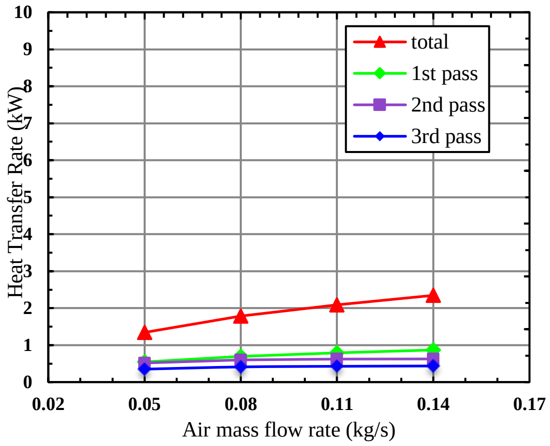

Figure 4.37 – Heat transfer rate for different flow rates at 100°C air inlet temperature (case 3).

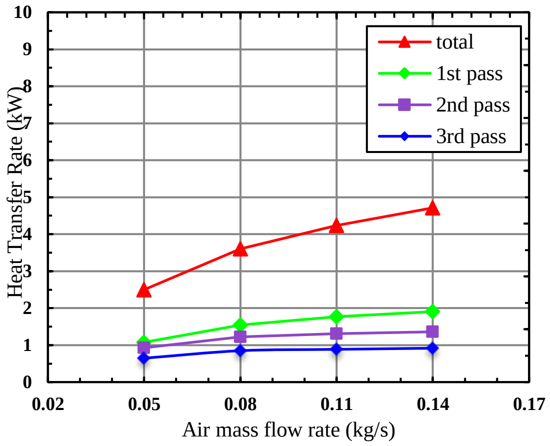

Figure 4.38 – Heat transfer rate for different flow rates at 150°C air inlet temperature (case 3).

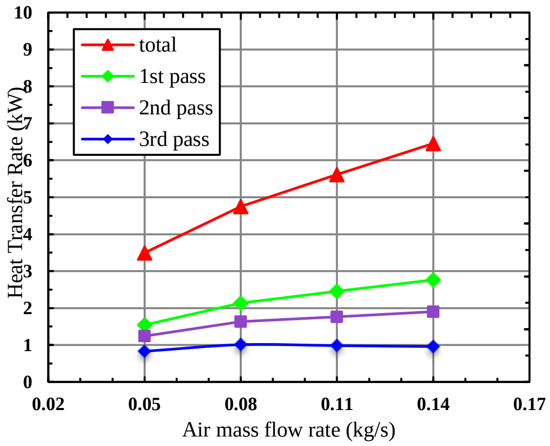

Figure 4.39 – Heat transfer rate for different flow rates at 200°C air inlet temperature (case 3).

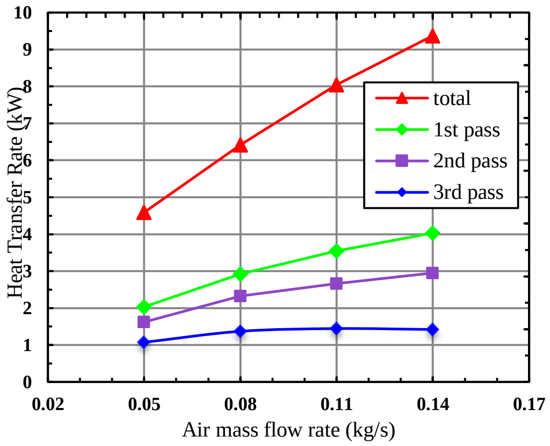

Figure 4.40 – Heat transfer rate for different flow rates at 250°C air inlet temperature (case 3).

Figure 4.41 to Figure 4.46 compare experimental results for the three cases at two different evaporator inlet temperatures, 150°C and 250°C. The figures show the rate of heat transfer for each pass, where their sum represents the overall heat transfer. An increase in the air inlet temperature resulted in increases in the temperature differences across the evaporator and the condenser, and therefore an increase in the overall rate of heat transfer. The heat transfer also increased as the air mass flow rate was increased. For a constant air inlet temperature, the heat duty across the first pass (blue area) was approximately the same for the three cases where only pool boiling was taking place, and similarly when comparing the heat transfer across the second pass (red area) for the same evaporator inlet temperature. However, the heat transfer mode occurring in the second pass was nucleate film boiling.

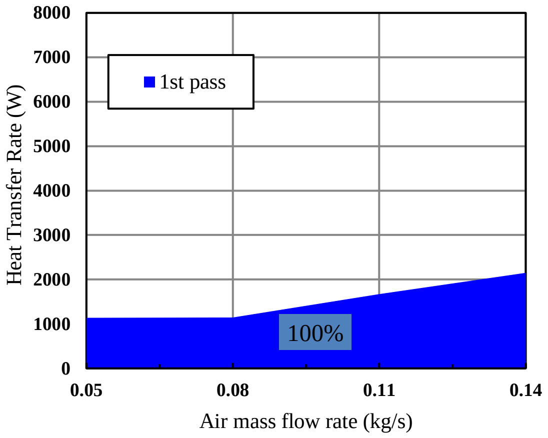

Figure 4.41 – Case 1 at 150°C.

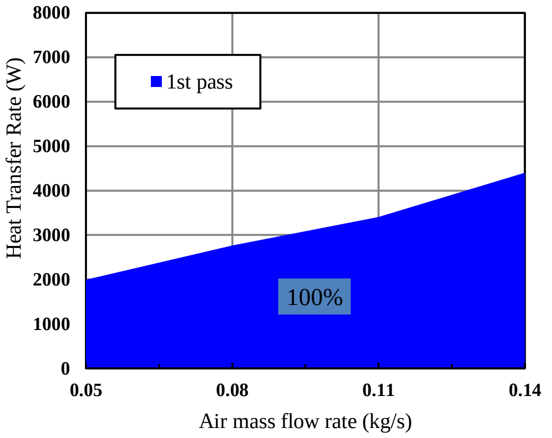

Figure 4.42 – Case 1 at 250°C.

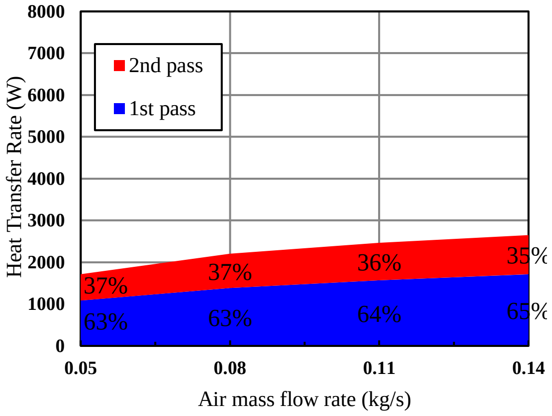

Figure 4.43 – Case 2 at 150°C.

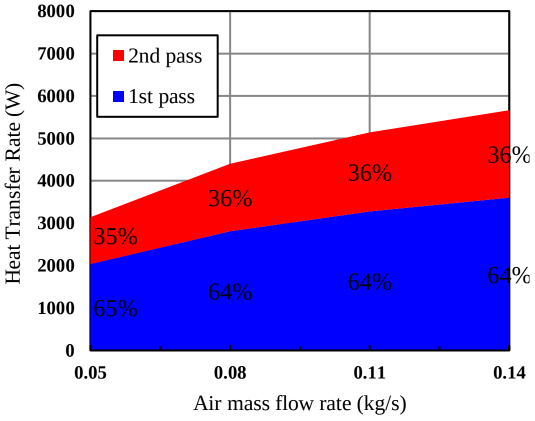

Figure 4.44 – Case 2 at 250°C.

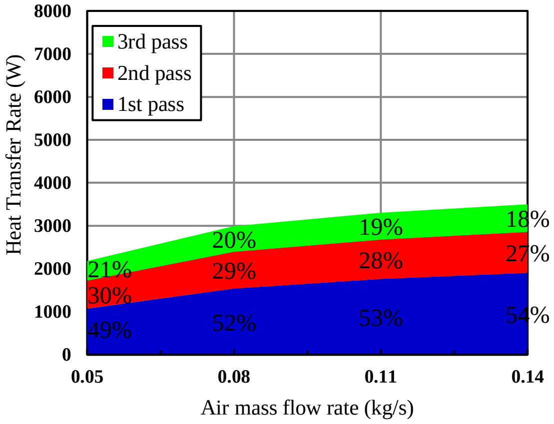

Figure 4.45 – Case 3 at 150°C.

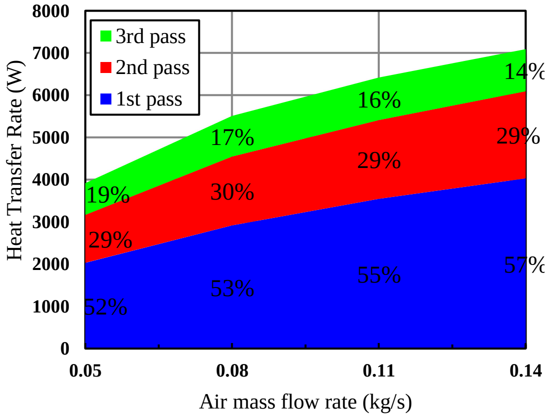

Figure 4.46 – Case 3 at 250°C.

According to the theoretical calculations shown in Figure 4.41 to Figure 4.46, pool boiling represented 100% of the evaporator heat input for case 1, 64% for case 2 and 53% for case 3 at a given inlet temperature (150 and 250°C). The same trend was also observed for the remaining air inlet temperatures (100 and 200°C). For a given air inlet temperature the addition of air passes led to more conductive paths in parallel, hence a lower overall resistance and higher overall heat transfer.

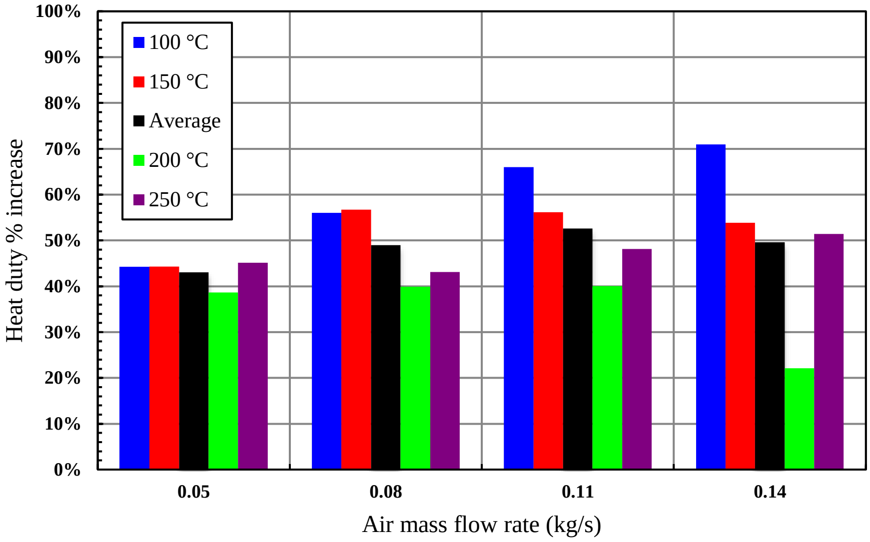

Figure 4.47 – Heat transfer rate % increase from case 2 to case 3.

The thermal performance improvement by increasing the number of passes on the evaporator is illustrated in Figure 4.47. The bar chart shows the percentage increase in the heat transfer rate calculated by the following equation:

$$Duty\ \%\ increase = \frac{Q_{case3} - Q_{case2}}{Q_{case2}} \times 100 \qquad (4.3)$$

An evident significant improvement in thermal performance is observed. The black bar in Figure 4.47 represents the average percentage increase for each four inlet temperatures at a specific mass flow rate. By adding a third pass, an average of about 50% increase in the heat duty is achieved.

4.2.3. CFD temperature distribution

Contours of the temperature distribution in the evaporator section are displayed in Figure 4.48. All cases were run at an air inlet temperature of 150°C and a mass flow rate of 0.14 kg/s. It can be clearly seen how the air temperature gradually decreases as the air flows towards the evaporator outlet, with the drop in temperature and hence the rate of heat transfer increasing as more passes are added. It can also be seen that the air temperature distribution within connecting ducts is essentially uniform due to the imposed adiabatic wall boundary condition.

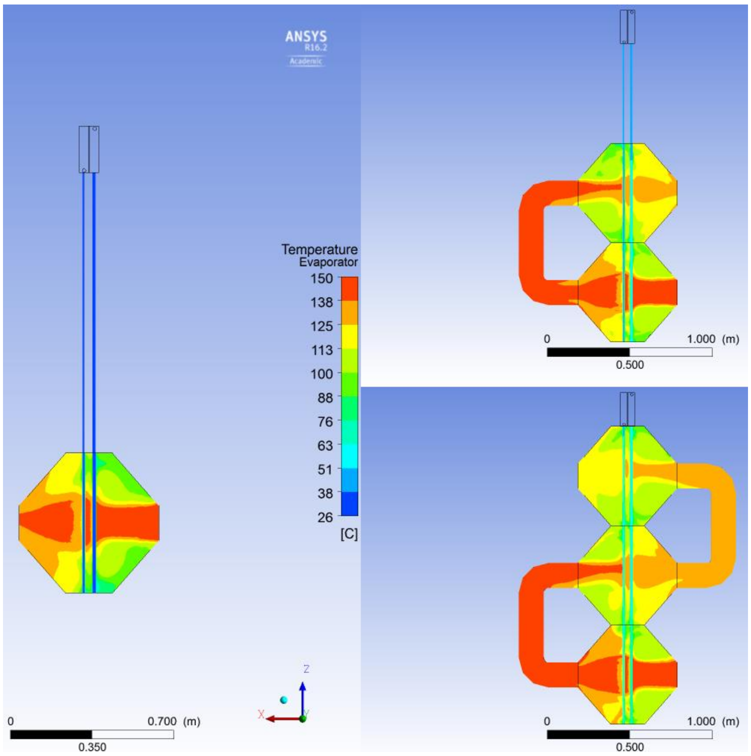

Figure 4.48 – Temperature contours across the evaporator for the three cases at 150°C, 0.14 kg/s.

Figure 4.49 shows the magnitude of the velocity vectors in the evaporator section for the three cases at 150°C air inlet temperature and 0.14 kg/s mass flow rate. The velocity profile in the three cases is similar. The blue colour refers to a zero mean velocity where the air flow is trapped in a recirculation zone outside the flow main stream, mainly at the top and bottom sections of each pass. The red colour corresponds to the highest velocity the air flow has reached; it can be seen that this occurs only in specific sections of the heat exchanger (HX), more specifically at the bends of the elbows where the air flow gains more speed due to the change in direction. This plot is helpful in identifying the wake regions within the heat exchanger, which can help in the optimisation of the heat exchanger design. A velocity distribution of the entire case 3 clearly showing the location of the circulation zones is available in Appendix E.

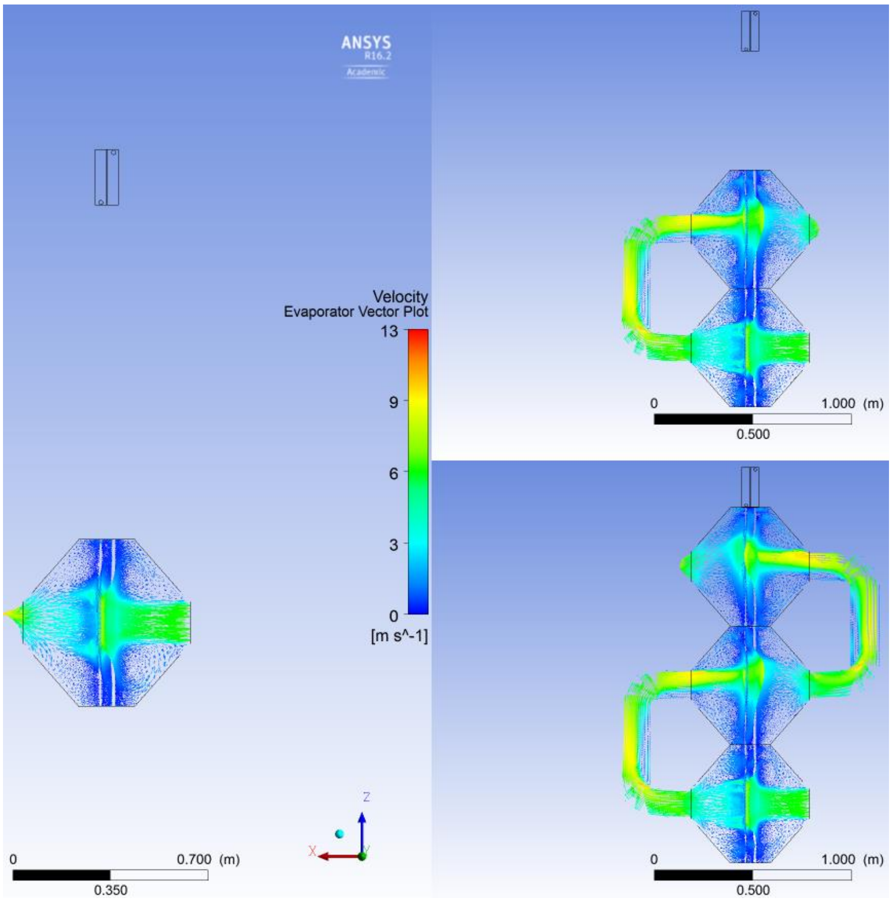

Figure 4.49 Velocity vector plot across the evaporator for the three cases at (150°C, 0.14 kg/s).

A section of the condenser is illustrated in Figure 4.50 where the temperature variation is shown across the heat pipes and water. The cross-section has been taken in the middle of the condenser, therefore at a height of 1.9 m from the bottom of the evaporator. The simulation was run at a water inlet temperature of 15°C, the cross-section was higher than the water inlet, which explains the minimum value of 17°C in the scale. The figure clearly shows how the water absorbs heat from the pipes as it flows around them in a U-shaped duct as the temperature of the pipes gradually increases. The pipe at the water inlet has the lowest temperature, indicating the highest convective heat transfer since the temperature difference between the pipe and water is the highest there. The water reaches the pipe at the outlet with the smallest temperature difference, therefore the convective heat transfer is least there. Comparing the pipe temperatures for the three cases, it is obvious that the three pass configuration has the highest temperature difference for water between inlet and outlet, and hence the highest heat transfer rate.

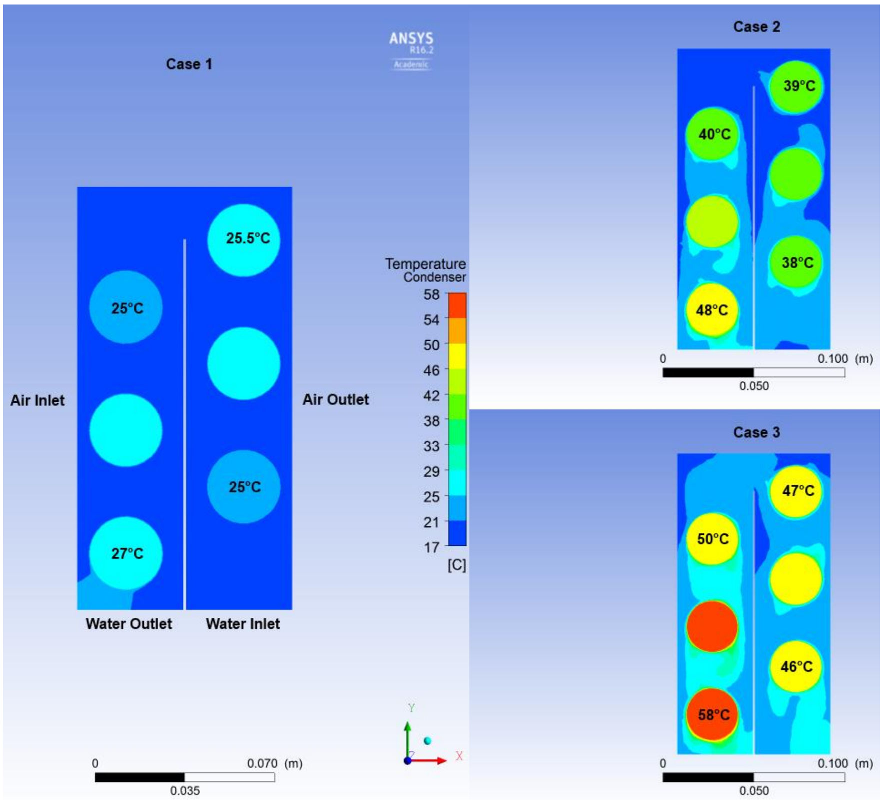

Figure 4.50 – Top view of condenser temperature contour for the three cases at (150°C, 0.14kg/s) and z=1.9m.

4.2.4. Thermal resistance, R and conductivity, k

Thermal resistance

As previously mentioned, the theoretical modelling was based on the resistance network analogy approach. This method was followed as it computes the total resistance of the TSHX which is needed to calculate the thermal conductivity of a single thermosyphon. Thus, it was necessary to calculate the thermal resistance across each component within the TSHX, such resistances include:

- External forced convection (air-to-pipes and water-to-pipes)
- Conduction across the thermosyphon wall thickness
- Boiling heat transfer (pool and film)
- Film condensation heat transfer

The thermal resistance was calculated at each stage of the TSHX, starting from where the air enters the HX system towards the air exit, similarly on the condenser side. Figure 4.51 and Figure 4.52 show the distribution of the thermal resistance in each pass on the evaporator and condenser side for cases 2 and 3 at the inlet temperature of 150°C for both cases. It is clear from the figures that the majority of the heat transfer resistances are located across the external forced convection region shown by the large areas (purple, blue and red colour). In addition, an increase in the mass flow rate results in an evident decrease in the resistance. The same trend was observed for the remaining air inlet temperatures.

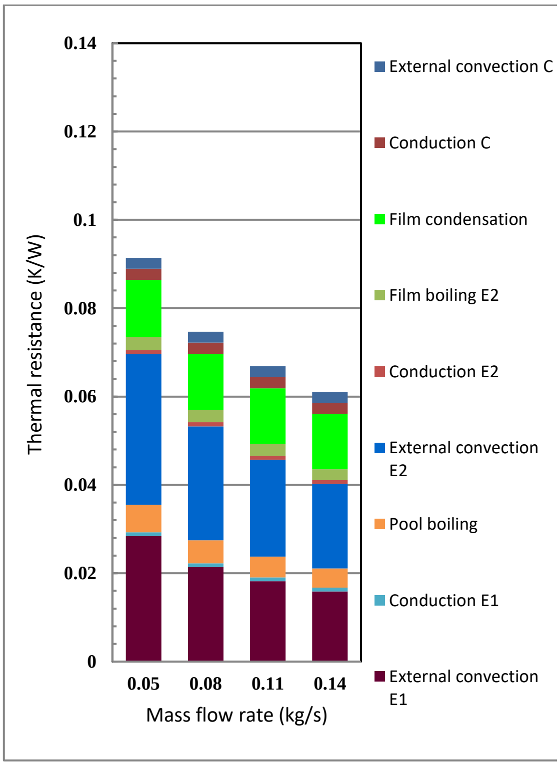

Figure 4.51 – Thermal resistance in each component of the TSHX (case 2) at 150°C, E-evaporator and C-condenser.

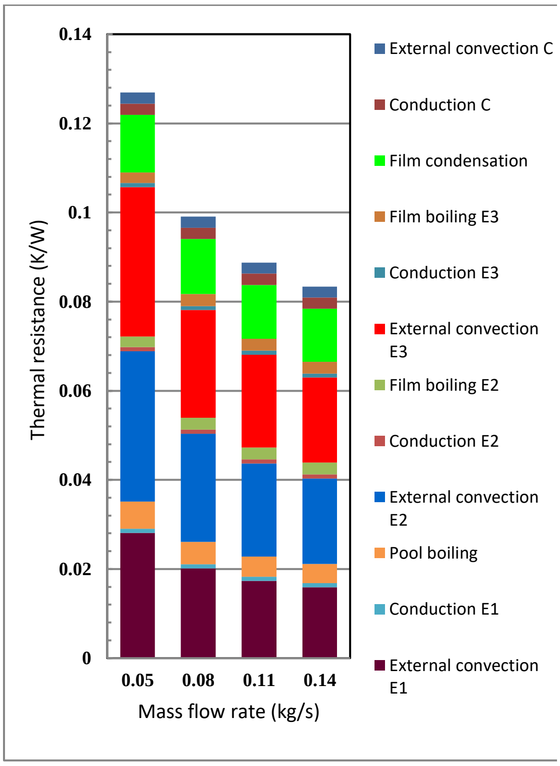

Figure 4.52 – Thermal resistance in each component of the TSHX (case 3) at 150°C, E-evaporator and C-condenser.

Figure 4.52 (case 3) has a higher number of resistances than Figure 4.51 (case 2), due to the higher number of passes which creates three extra resistances. However, it is how the resistances are arranged within the system that matters. In the TSHX under investigation, increasing the number of passes would increase the number of resistances, however this reduces the total resistance because the passes are arranged in a parallel configuration.

Figure 4.53 and Figure 4.54 show how the total resistance is affected by the change in the air inlet mass flow rate and temperature. Following the validation of the theoretical model, the total resistance in the above figures was calculated based on the experimental results for better accuracy. From the figures, a decrease in the total resistance is obvious when increasing the air inlet flow rate and temperature. A contradictory behaviour was previously observed when analysing the effect of mass flow rate and temperature on the thermal performance of the system (Figure 4.33 to Figure 4.40). This was expected as the thermal resistance acts in an inversely proportional way to the heat transfer rate.

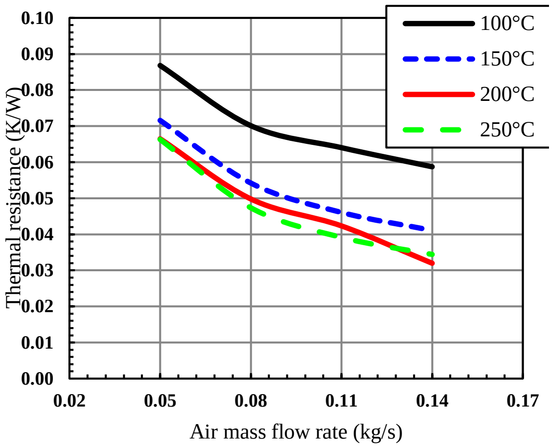

Figure 4.53 – Thermal resistance for different inlet conditions (case 2).

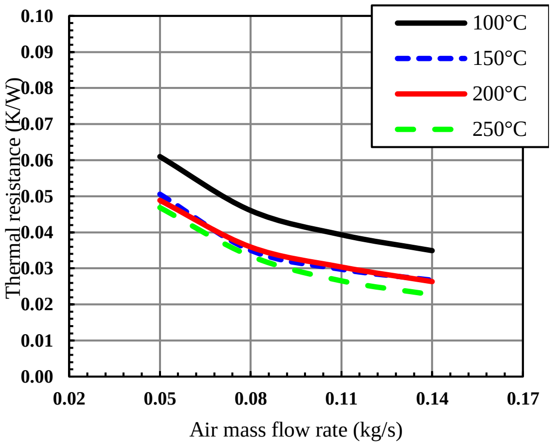

Figure 4.54 – Thermal resistance for different inlet conditions (case 3).

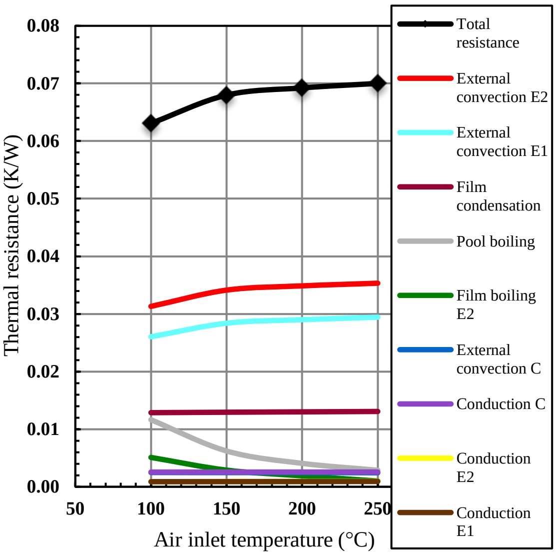

Figure 4.55 – Thermal resistance of each component for 0.05 kg/s and different inlet temperatures (case 2).

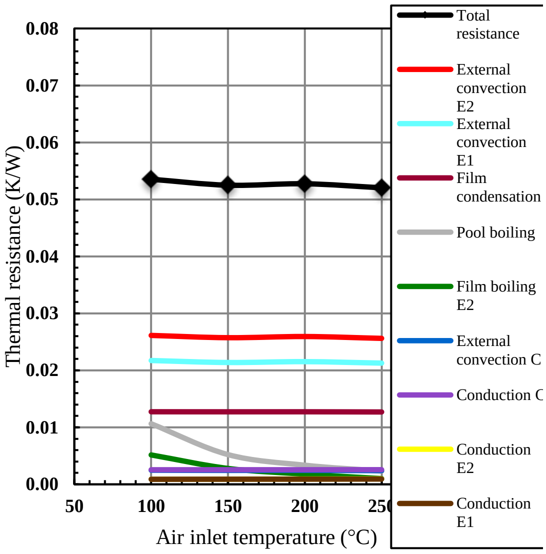

Figure 4.56 – Thermal resistance of each component for 0.08 kg/s and different inlet temperatures (case 2).

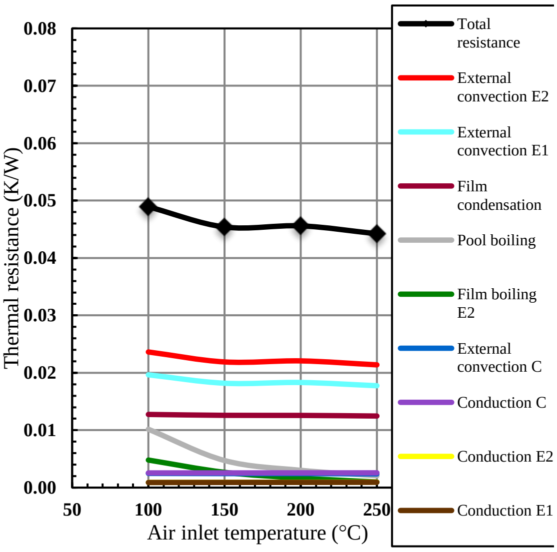

Figure 4.57 – Thermal resistance of each component for 0.11 kg/s and different inlet temperatures (case 2).

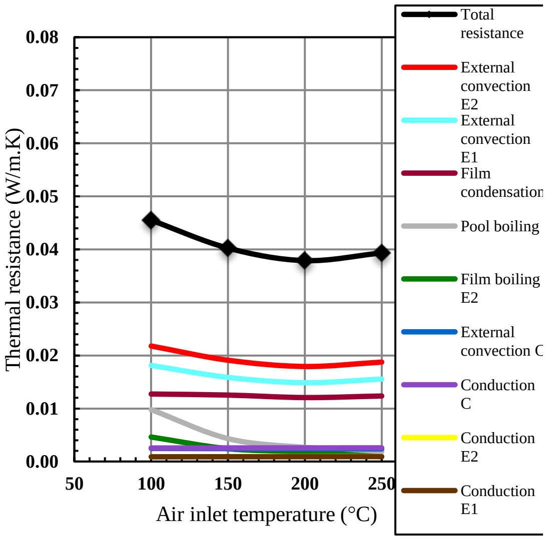

Figure 4.58 – Thermal resistance of each component for 0.14 kg/s and different inlet temperatures (case 2).

Using the theoretical model, the thermal resistance in each stage of the TSHX was plotted at different inlet temperatures for the multi-pass cases shown in Figure 4.55 to Figure 4.62. Each figure is plotted at a constant air mass flow rate. As already discussed before and as clearly shown in Figure 4.55 to Figure 4.62, an increase in the inlet temperature and mass flow rate have a positive effect on the performance of the heat exchanger as the resistance decreases. However, uncertainty exists in the theoretical results as shown in Figure 4.55 where the total resistance trend should be decreasing with increasing air inlet temperatures. The uncertainty in Figure 4.55 is about 35% and the experimental thermal resistance should be 0.087 K/W as shown in Figure 4.53 for a combination of 100°C and 0.05 kg/s.

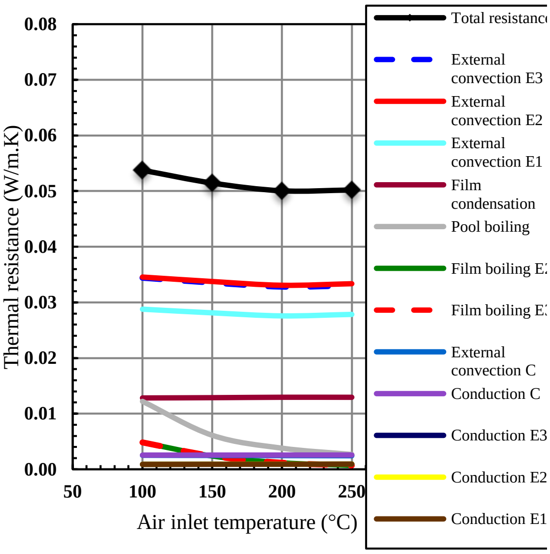

Figure 4.59 – Thermal resistance of each component for 0.05 kg/s and different inlet temperatures (case 3).

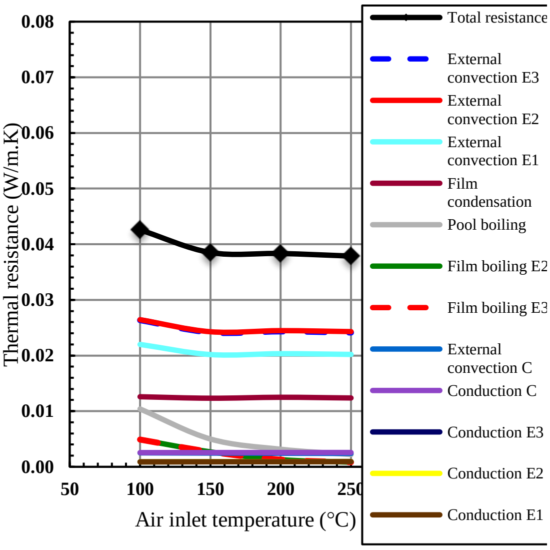

Figure 4.60 – Thermal resistance of each component for 0.08 kg/s and different inlet temperatures (case 3).

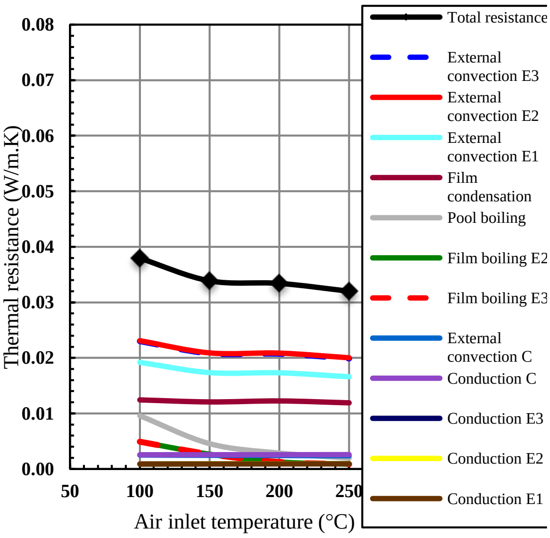

Figure 4.61 – Thermal resistance of each component for 0.11 kg/s and different inlet temperatures (case 3).

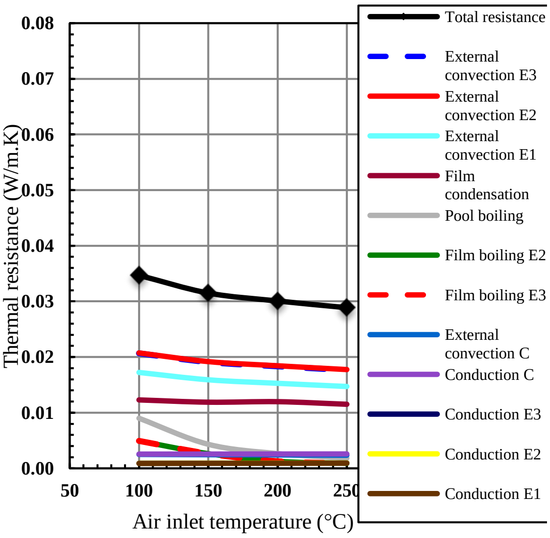

Figure 4.62 – Thermal resistance of each component for 0.14 kg/s and different inlet temperatures (case 3).

Looking at the same figures (Figure 4.55 to Figure 4.62), with the increase of the inlet temperatures, a steep decrease in the resistance is observed for pool and film boiling regimes mainly between 100 and 150°C. This could be due to the instability of the boiling regime at the lower air inlet temperature, creating higher thermal resistance and uncertainty. Consequently, the thermosyphons were not well performing. A steep drop in the resistance occurred when increasing the air inlet temperature where the boiling regime is more stable. The steep drop in the resistance between 100 and 150 °C is also shown in Figure 4.53 and Figure 4.54.

Thermal conductivity

Using ANSYS Fluent as a numerical tool, only two modes of heat transfer existed within the TSHX, external forced convection (air-pipes, water-pipes) and conduction through the pipes. The thermal conductivity was calculated through the theoretical modelling of the system and implemented in the numerical modelling as a material property of the solid rods.

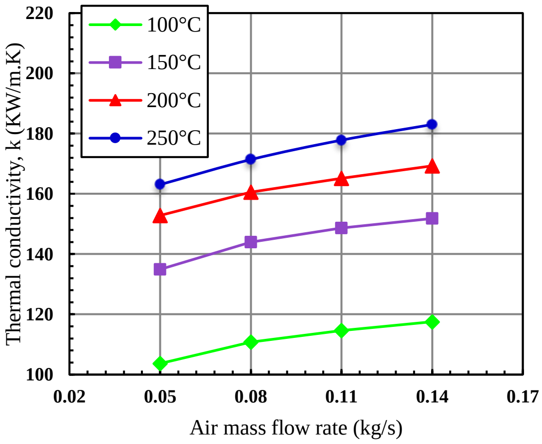

Figure 4.63 – Thermal conductivity at different inlet conditions (case 2).

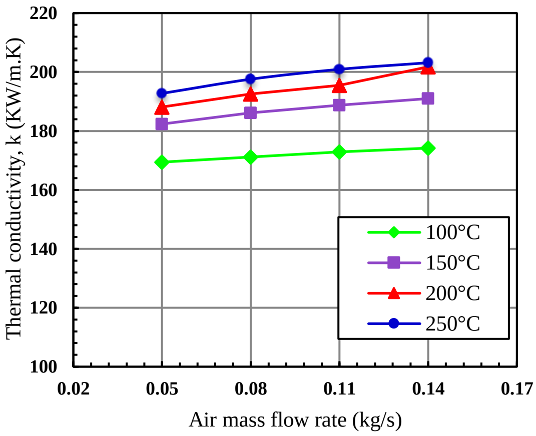

Figure 4.64 – Thermal conductivity at different inlet conditions (case 3).

The thermal conductivity k is plotted in Figure 4.63 and Figure 4.64 for both multi-pass cases. The plot is for different air mass flow rates and temperatures. As it can be seen from equation (21) in chapter 3, the thermal conductivity is inversely proportional to the thermal resistance, hence directly proportional to the heat transfer rate. The above two figures show an increase in the thermal conductivity while increasing the air inlet mass flow rates and temperatures. Alternatively, a higher heat transfer rate is achieved with a higher thermal conductivity. This can also be seen by comparing both cases in Figure 4.63 and Figure 4.64, where higher thermal conductivity is achieved in case 3 at all tested conditions compared to the same tested conditions from case 2. The reason is due to the higher heat transfer in case 3 than case 2.

From the vertical scale, which ranges between 10^5 to $22 \times 10^4\ W/m.K$, it can be clearly stated that the transfer of heat through phase change mechanisms inside a thermosyphon is very efficient compared to pure conduction in a same size rod. This is justified by the thermal conductivity values obtained and shown in Figure 4.63 and Figure 4.64. The values are several orders of magnitude higher compared to a pure carbon steel solid rod which has a thermal conductivity of about 54 $W/m.K$ at 25°C [115].

Based on Fourier's law, the rate of heat transfer by conduction is proportional to the negative temperature gradient and the area where the heat flows through the material at a right angle to that gradient (equation (4.4)),

$$Q_{conduction} = -k \times A \times \frac{\Delta T}{\Delta x} \tag{4.4}$$

where A is the cross sectional area of the pipe (the circular area of the pipe) and ΔT is the temperature difference between the bottom and the top of the adiabatic section. Figure 4.65 shows a schematic of the conduction heat transfer through a material with a thermal conduction k, where heat is flowing from a temperature T_1 to a lower temperature T_2. The material is laterally insulated and Δx represents the length of the material which the heat is covering.

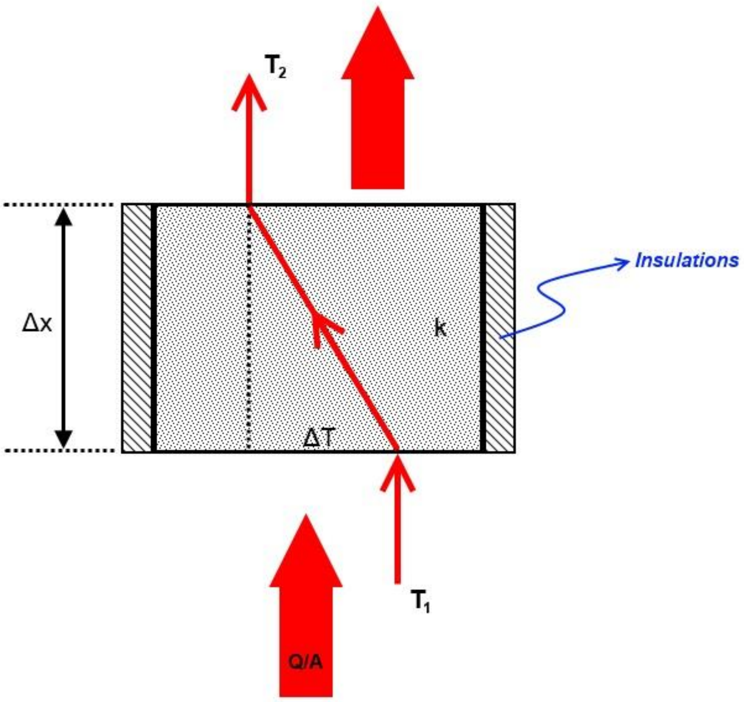

Figure 4.65 – Conduction heat transfer schematic diagram.

A random pipe was chosen to study the heat transfer by conduction inside the solid rod. An interesting behaviour of the temperature within the pipe was observed. As mentioned before, the thermosyphons in Fluent were treated as solid rods with a constant thermal conductivity calculated from existing correlations adopted from the literature. Figure 4.66 shows a comparison of the temperature behaviour of a random selected pipe within the heat exchanger. Pipe number 4 was selected for the analysis (Figure 4.28). As it can be seen from Figure 4.66 and for all the cases, the temperature of the pipe decreases gradually starting from the evaporator (bottom) to the condenser section (top).

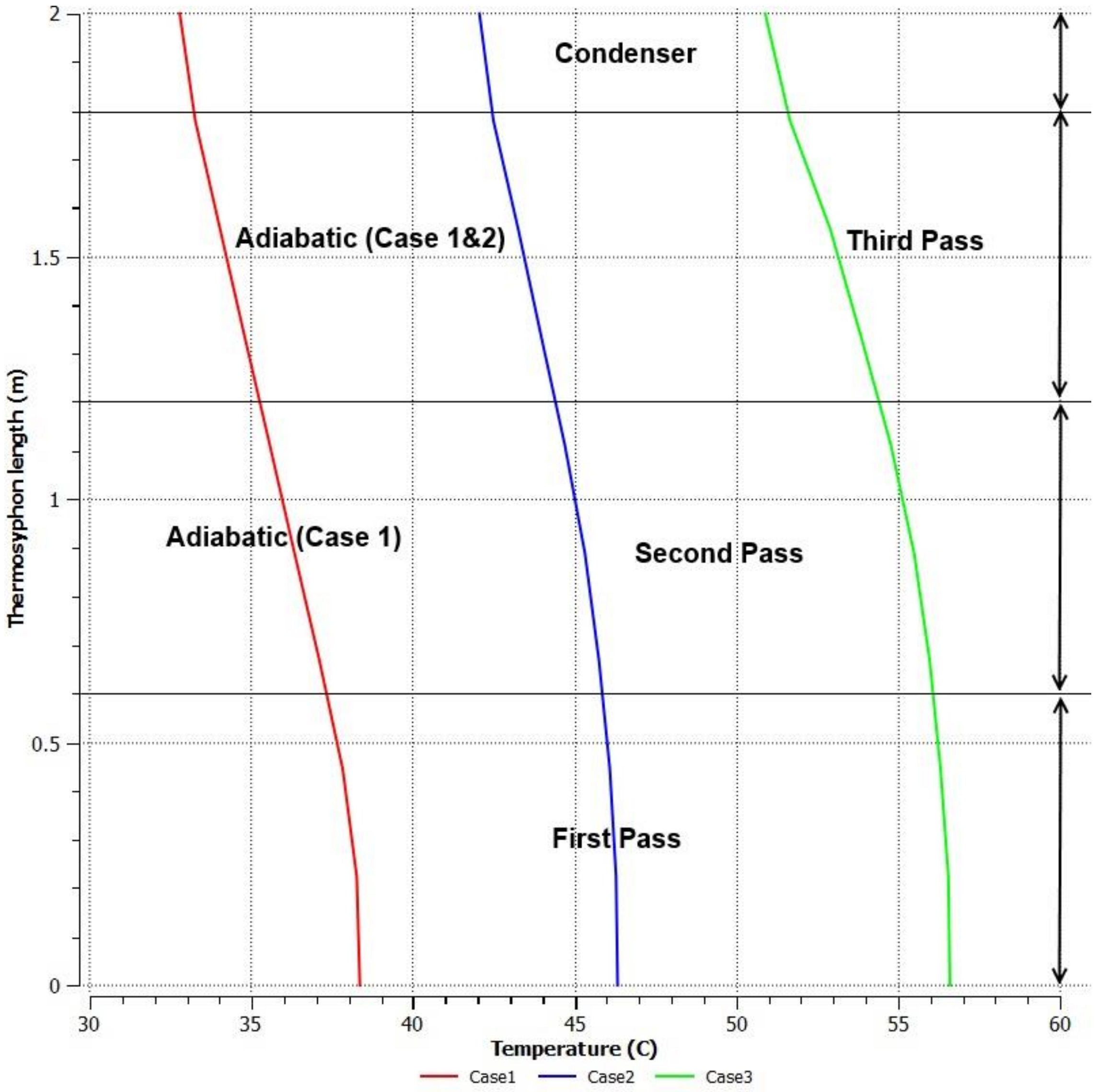

Figure 4.66 – CFD Temperature distribution along pipe 4 for all three cases at (150°C, 0.14 kg/s).

Experimentally, the temperature in the adiabatic section is approximately uniform. However, in Fluent, the temperature varies in every cell in order to keep the heat flowing through the material. In other words, the temperature difference is a driven force to transfer heat by conduction along the length of the whole solid pipes. As it can be seen from Figure 4.66, and more specifically in the adiabatic section, the temperature is decreasing linearly. This can be seen by a straight line of negative gradient in case 1 and 2. However, the relation is nonlinear within the air passes as the conduction heat transfer is affected by the convection around the pipes.

4.2.5. Effectiveness

A numerical effectiveness-number of transfer units $(\epsilon - NTU)$ model was developed on the whole heat exchanger in order to analyse the effect of different inlet conditions and air passes on the rate of heat transfer. Jouhara and Merchant [80] and Ramos et al. [84] developed a similar model where the heat exchanger was treated as two separate heat exchangers consisting of the evaporator and condenser coupled by the thermosyphons as a mode of heat transfer.

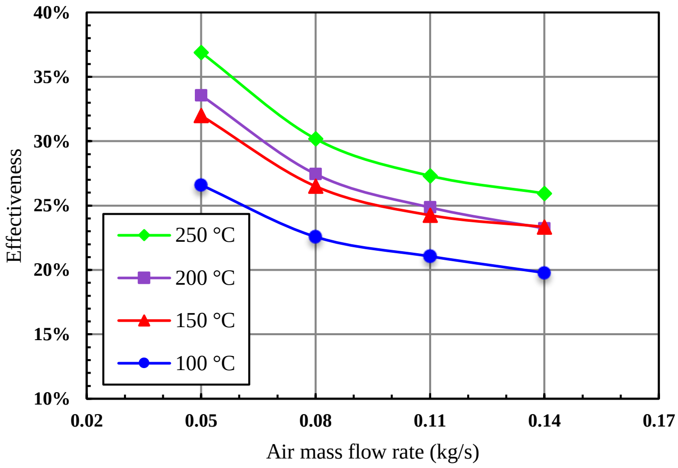

Figure 4.67 – Effectiveness at different air inlet temperature and mass flow rates (Case 3).

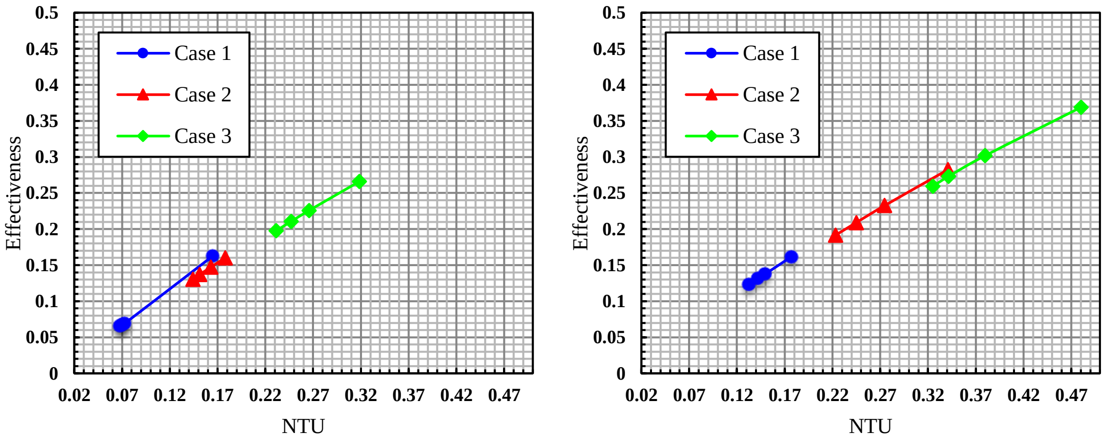

Figure 4.68 – Effectiveness vs NTU at different inlet conditions (100°C).

Figure 4.69 – Effectiveness vs NTU at different inlet conditions (250°C).

Figure 4.67 shows the variation of the overall effectiveness for the different inlet conditions for Case 3. A consistent downward trend can be observed for the different inlet conditions, this trend being in good agreement with Jouhara and Merchant [15] and Ramos et al. [84] where a higher effectiveness is achieved by increasing the evaporator inlet temperature while reducing its mass flow rate.

Figure 4.68 and Figure 4.69 show the change of the effectiveness with the NTU at different inlet conditions for the three test cases, for air inlet temperatures of 100°C and 250°C, respectively. Each case is plotted at four different air inlet flow rates (0.05, 0.08, 0.11 and 0.14 kg/s). It can be clearly seen that more air passes installed at the evaporator result in a higher effectiveness of the heat exchanger, although the impact on pressure drop should always be taken into account. Both figures show a linear increase in effectiveness with NTU, which agrees with the effectiveness-NTU graphs plotted by Incropera and DeWitt [116] over these ranges of effectiveness and NTU (shown in appendix D).

4.2.6. Error Analysis

Uncertainty analysis is an essential technique to assess how accurate the test results are. Figure 4.70 shows how the percentage error of the effectiveness varies with the change in the inlet air mass flow rate for different inlet temperatures. It is obvious from the graph that the propagated error associated with the calculated effectiveness is inversely proportional to both mass flow rate and the inlet temperature. In other words, an increase in the air mass flow rate and inlet temperature reduces the percentage error of the effectiveness. The largest error came from the reading of the thermocouples at lower temperatures, more specifically at 10 Hz. Figure 4.70 shows an inversely proportional relationship between the uncertainty for the effectiveness and temperature change, which explains why the maximum uncertainties were achieved at low inlet temperature because the temperature change is very small. For most engineering applications, a 10% error is often considered an acceptable range [117].

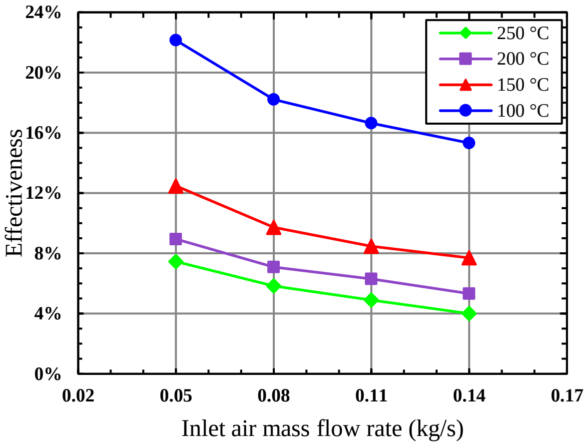

Figure 4.70 – The uncertainty of the effectiveness at different inlet conditions.

The uncertainty in the rate of heat transfer is presented in Figure 4.71 and Figure 4.72. The lowest uncertainty occurs at the highest inlet temperature of 250°C and the highest flow rate of 0.14 kg/s, most specifically in case 3. Considering the equations in 3.3.3, the smaller the temperature difference across the condenser, the higher the uncertainty. The figures also show that the uncertainty of the heat transfer in case 1 is the highest, when considering the lowest temperature difference across the condenser.

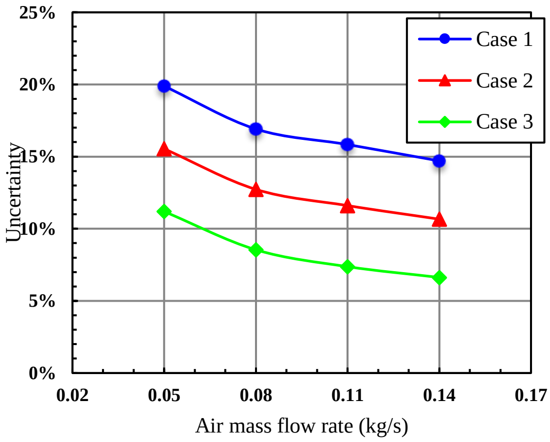

Figure 4.71 – Uncertainty of the three cases at 100°C air inlet temperature.

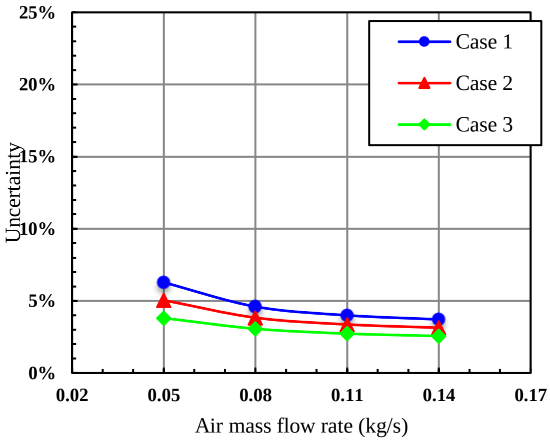

Figure 4.72 – Uncertainty of the three cases at 250°C air inlet temperature.

Chapter 5. SUMMARY, CONCLUSION AND RECOMMENDATIONS

The investigation reported in this thesis was successfully carried out while modelling a new type of heat exchangers that uses the thermosyphon technology to transport thermal energy within the system.

The validation was carried out on a different number of shell passes on the evaporator section for various air inlet conditions. Inlet conditions include an alteration in the air inlet flow rate and temperature. The condenser inlet conditions were kept constant at 0.08 kg/s and 15°C for both water mass flow rate and temperature, respectively.

5.1. Theoretical model

A detailed theoretical model was built for the entire system by applying various heat transfer correlations at specific locations within the heat exchanger. The resistance analogy approach was applied to model the entire TSHX system in order to calculate the overall thermal resistance. To carry out a successful theoretical model, it was important to choose the right correlations for various heat transfer modes within the heat exchanger. The various modes of heat transfer were identified outside and inside the thermosyphons: External forced convection on both evaporator and condenser and boiling and condensation heat transfer mechanisms inside the thermosyphons.

The first step was to perform experimental tests of a single thermosyphon in order to understand the thermal behaviour at various working fluids, evaporator and condenser inlet conditions. Also, to assess the compatibility of the different working fluids with carbon-steel as a material used for thermosyphon shell. The boiling heat transfer regime was modelled both theoretically and experimentally. It was found that water as a working fluid outperformed the other working fluids namely, acetone, ethanol and toluene. Concerning the boiling regime, the heat transfer coefficient was measured and predicted using a few well-known pool boiling correlations. The heat transfer coefficient predicted from the Rohsenow correlation was found to be comparable with the measured value and consistent over the entire tested range with adequate accuracy of about 30%. A new value was correlated for the surface-fluid combination constant (C_{sf}). Following a trial and error method, a value of 0.05 was proposed for Rohsenow's constant, which can be used for future modelling of thermosyphons made out of carbon steel and containing water as the working fluid.

Following the single thermosyphon tests, and based on an extensive literature research; a list of correlations was prepared to use in the theoretical model for the whole heat exchanger unit.

Two separate theoretical models were developed based on 2 multi-pass configurations. Excluding the external forced convective heat transfer on both evaporator and condenser, in case 2, it was found that the thermal resistance in the first pass, which is associated with the conduction across the thermosyphon wall and pool boiling resistances, are acting in a parallel mode along the thermal resistance in the second pass, associated with conduction and nucleate film boiling resistance. This is due to the filling ratio (1/2) of the thermosyphon in this case, where the second pass is exposed to the liquid film. The resistance of one thermosyphon was found by adding the resistances of both passes acting in parallel, and together, acting in a serial mode with the film condensation resistance.

For case 3, an extra air pass resulted in extra heat transfer modes; similar to those existed in the second pass. In this case, the filling ratio is 1/3, where the second and the third pass are exposed to the liquid film. The three passes acted in a parallel arrangement between each other, all together, in a serial mode with the film condensation resistance. In order to calculate the total thermal resistance of the whole system, the external forced convection resistances were added in series to the resistance of the total of six thermosyphons.

A higher number of passes has added more resistances within the heat exchanger, though providing a lower overall thermal resistance. The number of resistances does not imply a higher overall resistance, though, it is the way how these resistances are arranged within the system. Due to the parallel arrangement of the thermosyphons, the thermal resistance of one thermosyphon is a multiple of the number of thermosyphons installed within the system ($i.e. R_{1TS} = 6 \times R_{6TSs}$), hence providing a lower overall resistance.

One last conclusion that can be drawn from the theoretical analysis concerns the amount of heat transfer at each stage within the heat exchanger starting from the inlet towards the outlet. From the analysis, it was found that the highest thermal resistances occurred in the entire systems were the external convective ones. This is important as it shows the areas where the model can be improved.

5.2. Numerical Model

Before starting the numerical modelling, it was necessary to calculate the thermal conductivity at each evaporator inlet condition for both cases. This was important in order to simplify the two-phase mechanisms inside the thermosyphons in ANSYS Fluent. This approach was followed as the multiphase behaviour inside the thermosyphons was not a point of interest during the numerical modelling. Instead, the numerical tool is used to simulate the shell-side heat transfer. Therefore, for the sake of simplicity and reducing the computational cost and time, the thermosyphons were treated as solid rods with thermal conductivity values calculated from the thermal resistance model. Each inlet condition corresponded to a different value of thermal conductivity where it was implemented in ANSYS Fluent by modifying the material property. The thermal conductivity calculated was ranged from 100 to $220\, kW/m.K$. Using this approach, the effect of the boiling and condensation heat transfer mechanisms was successfully simulated through the pure conduction heat transfer.

The single phase flow around the solid rods was modelled using the Realizable $K-\varepsilon$ turbulence model. This model was shown to be reliable in simulating the fluid behaviour and thermal performance of this type of heat exchanger system. In addition, the scalable wall function was used as a near-wall treatment model. This was found to be more reliable than the standard wall function for the simulated cases based on the value of y^+ which showed to be below 15, giving the choice of scalable an advantage over the standard wall function. Moreover, the energy balance of the whole system was observed to be worse in the case of standard than scalable wall function.

5.3. Validation and comparison

The experimental validation was successfully carried out with the same range of inlet conditions. Results were mainly focused on the heat transfer rate across the evaporator and condenser. The experimental results were found to be within a range of $\pm 15\%$ of the numerical and theoretical results. The optimum performance of the TSHX was observed at the highest mass flow rate and inlet temperature (0.14kg/s, 250°C) for each case, 4403, 6191 and 9375 Watts for case 1, case 2 and case 3 respectively. Where, the performance of each thermosyphon is 734, 1032, 1563 Watts respectively for case 1, 2 and 3. This clearly shows the heat transfer enhancement achieved when going from a cross-flow to multi-pass configuration.

The validated CFD model could be used as a tool to investigate shell-side weaknesses which experimental tests cannot achieve. Such weaknesses include fouling which is a major problem in various heat exchanger designs. The current validated model provides a clear visualisation of the shell side fluid and thermal behaviour, more specifically the weak areas or recirculation zones where improvements can be made.

5.4. Future work recommendations

Recommendations can be made for various modifications in order to investigate their effects on the current model and for future heat exchanger modelling:

- The surface-fluid combination constant should be tested for a wider thermosyphon range of inlet conditions
- Different filling ratios may be tested for an optimum performance of the heat exchanger
- Increasing the number of fluid passes on the condenser side to investigate its effect on the thermal performance
- Investigating the thermal performance by changing the inlet flow rate and temperature of the condenser fluid flow
- Fins could be installed on both evaporator and condenser side of the thermosyphons to reduce the external forced convection thermal resistance

- Using this model to simulate the entire TSHX system including the two-phase change inside the thermosyphons
- Linking the two-phase flow inside thermosyphons to the single phase outside
- Investigating different turbulence intensities at both evaporator and condenser inlets
- Creating a fully validated numerical model of the single thermosyphon
- Simulating one thermosyphon integrated inside the multipass in Fluent, including the multi-phase mechanisms.

REFERENCES

[1] A. Al Makky, A. Alaswad, D. Gibson, A.G. Olabi, Prediction of the gas emission from porous media with the concern of energy and environment, Renew. Sustain. Energy Rev. 68 (2016) 1–13. doi:10.1016/j.rser.2016.08.001.

[2] Climate Change Act 2008, (2008). http://www.legislation.gov.uk/ukpga/2008/27/contents.

[3] European Environment Agency, (2016). http://www.eea.europa.eu/themes/climate/intro.

[4] T. Sivasakthivel, M. Philippe, K. Murugesan, V. Verma, P. Hu, Experimental thermal performance analysis of ground heat exchangers for space heating and cooling applications, Renew. Energy. 113 (2017) 1168–1181. doi:10.1016/j.renene.2017.06.098.

[5] A.G. Olabi, Developments in sustainable energy and environmental protection, Energy. 39 (2012) 2–5. doi:10.1016/j.energy.2011.12.037.

[6] J. Danielewicz, M.A. Sayegh, B. Śniechowska, M. Szulgowska-Zgrzywa, H. Jouhara, Experimental and analytical performance investigation of air to air two phase closed thermosyphon based heat exchangers, Energy. 77 (2014) 82–87. doi:10.1016/j.energy.2014.04.107.

[7] H. Shabgard, M.J. Allen, N. Sharifi, S.P. Benn, A. Faghri, T.L. Bergman, Heat pipe heat exchangers and heat sinks: Opportunities, challenges, applications, analysis, and state of the art, Int. J. Heat Mass Transf. 89 (2015) 138–158. doi:10.1016/j.ijheatmasstransfer.2015.05.020.

[8] C. Haddad, C. Périlhon, A. Danlos, M.-X. François, G. Descombes, Some efficient solutions to recover low and medium waste heat: Competitiveness of the thermoacoustic technology, Energy Procedia. 50 (2014) 1056–1069. doi:10.1016/j.egypro.2014.06.125.

[9] Econotherm (UK) Ltd. Waste heat recycling technology, (2007). http://www.econotherm.eu/.

[10] H. Jouhara, Heat pipe based systems for industrial and renewable energy management, (2015) 40. http://www.hexag.org/news/32/hussam_jouhara.pdf.

[11] O. Labbadlia, B. Laribi, B. Chetti, P. Hendrick, Numerical study of the influence of tube arrangement on the flow distribution in the header of shell and tube heat exchangers, Appl. Therm. Eng. 126 (2017) 315–321. doi:10.1016/j.applthermaleng.2017.07.184.

[12] S. Jin, P. Hrnjak, Effect of end plates on heat transfer of plate heat exchanger, Int. J. Heat Mass Transf. 108 (2017) 740–748. doi:10.1016/j.ijheatmasstransfer.2016.11.106.

[13] B. Kumar, A. Soni, S.N. Singh, Effect of geometrical parameters on the performance of chevron type plate heat exchanger, Exp. Therm. Fluid Sci. 91 (2018) 126–133. doi:10.1016/j.expthermflusci.2017.09.023.

[14] B. Sunden, High temperature heat exchangers (HTHE), Enhanc. Compact Ultra-Compact Heat Exch. Sci. Eng. Technol. (2005) 226–238. http://www.google.com/patents/US5362454%255Cnhttp://dc.engconfintl.org/cgi/viewcontent.cgi?article=1024&context=heatexchangerfall2005.

[15] Types of Heat Exchanger, Parallel flow, Cross flow, Counter flow, (n.d.). http://marinenotes.blogspot.co.uk/2012/10/types-of-heat-exchangersparallel.html.

[16] K. Ramesh, Applications of heat-exchangers in food industry, (n.d.). http://www.wonderwhizkids.com/popups/App_Food_Industry.html.

[17] B.I. Master, K.S. Chunangad, V. Pushpanathan, Heat exchanger fouling and cleaning : Fundamentals and applications fouling mitigation using helixchanger heat exchangers, Heat Exch. Fouling Clean. Fundam. Appl. (2003) 1–6.

[18] J.-F. Zhang, B. Li, W.-J. Huang, Y.-G. Lei, Y.-L. He, W.-Q. Tao, Experimental performance comparison of shell-side heat transfer for shell-and-tube heat exchangers with middle-overlapped helical baffles and segmental baffles, Chem. Eng. Sci. 64 (2009) 1643–1653. doi:10.1016/j.ces.2008.12.018.

[19] R.K. Shah, K. Ramesh, D.P. Sekulić, Fundamentals of heat exchanger design, (2003) 941.

[20] K.J. Bell, Delaware method for shell-side design, 3 (1988) 45. doi:10.2307/302397.

[21] F.G. Llc, Process Heat Transfer, (2003).

[22] D.Q. Kern, Process Heat Transfer, McGraw-Hill, 1950. https://books.google.co.uk/books?id=OgNRAAAAMAAJ.

[23] G.F. Hewitt, G.L. Shires, T.R. Bott, Process heat transfer, CRC Press, 1994. https://books.google.co.uk/books?id=tNhSAAAAMAAJ.

[24] E. Ozden, I. Tari, Shell side CFD analysis of a small shell-and-tube heat exchanger, Energy Convers. Manag. 51 (2010) 1004–1014. doi:10.1016/j.enconman.2009.12.003.

[25] R. Boro, Heat Exchangers Design and Construction, Eng. Technol. Bus. (2012). http://www.slideshare.net/rijumoniboro/heat-exchangers-12606868?next_slideshow=1.

[26] M. Zhang, F. Meng, Z. Geng, CFD simulation on shell-and-tube heat exchangers with small-angle helical baffles, Front. Chem. Sci. Eng. 9 (2015) 183–193. doi:10.1007/s11705-015-1510-x.

[27] J. Lutcha, J. Nemcansky, Performance improvement of tubular heat exchangers by helical baffles, Chem. Eng. Res. Des. 68 (1990) 263–270. http://www.scopus.com/inward/record.url?eid=2-s2.0-0025431432&partnerID=tZOtx3y1.

[28] T. Pekdemir, T.W. Davies, L.E. Haseler, A.D. Diaper, Pressure drop measurements on the shell side of a cylindrical shell-and-tube heat exchanger, Heat Transf. Eng. 15 (1994) 42–56. doi:10.1080/01457639408939830.

[29] H. Halle, J.M. Chenoweth, M.W. Wambsganss, Shellside waterflow pressure drop distribution measurements in an industrial-sized test heat exchanger, J. Heat Transfer. 110 (1988) 60–67. http://dx.doi.org/10.1115/1.3250474.

[30] B. Gay, N.V. Mackley, J.D. Jenkins, Shell-side heat transfer in baffled cylindrical shell- and tube exchangers—an electrochemical mass-transfer modelling technique, Int. J. Heat Mass Transf. 19 (1976) 995–1002. doi:10.1016/0017-9310(76)90181-2.

[31] H. Li, V. Kottke, Visualization and determination of local heat transfer coefficients in shell-and-tube heat exchangers for staggered tube arrangement by mass transfer measurements, Exp. Therm. Fluid Sci. 17 (1998) 210–216. doi:10.1016/S0894-1777(97)10064-4.

[32] H.D. Li, V. Kottke, Visualization and determination of local heat transfer coefficients in shell-and-tube heat exchangers for in-line tube arrangement by mass transfer measurements, Heat Mass Transf. 33 (1998) 371–376. doi:10.1007/s002310050203.

[33] A. Karno, S. Ajib, Effect of tube pitch on heat transfer in shell-and-tube heat exchangers-new simulation software, Heat Mass Transf. Und Stoffuebertragung. 42 (2006) 263–270. doi:10.1007/s00231-005-0002-9.

[34] D. Eryener, Thermoeconomic optimization of baffle spacing for shell and tube heat exchangers, Energy Convers. Manag. 47 (2006) 1478–1489. doi:10.1016/j.enconman.2005.08.001.

[35] E.M. Sparrow, L.G. Reifschneider, Effect of interbaffle spacing on heat

transfer and pressure drop in a shell-and-tube heat exchanger, Int. J. Heat Mass Transf. 29 (1986) 1617–1628. doi:10.1016/0017-9310(86)90103-1.

[36] B. Peng, Q.W. Wang, C. Zhang, G.N. Xie, L.Q. Luo, Q.Y. Chen, M. Zeng, An experimental study of shell-and-tube heat exchangers with continuous helical baffles, J. Heat Transfer. 129 (2007) 1425. doi:10.1115/1.2754878.

[37] M.M. Aslam Bhutta, N. Hayat, M.H. Bashir, A.R. Khan, K.N. Ahmad, S. Khan, CFD applications in various heat exchangers design: A review, Appl. Therm. Eng. 32 (2012) 1–12. doi:10.1016/j.applthermaleng.2011.09.001.

[38] M. Prithiviraj, M.J. Andrews, Three-dimensional numerical simulation of shell-and-tube heat exchangers. Part II: Heat Transfer, Numer. Heat Transf. Part A Appl. 33 (1998) 817–828. doi:10.1080/10407789808913968.

[39] M. Prithiviraj, M.J. Andrews, Three-dimensional numerical simulation of shell-and-tube heat exchangers. Part I: Heat Transfer, Numer. Heat Transf. Part A Appl. 33 (1998) 817–828. doi:10.1080/10407789808913968.

[40] M.J.A. Manikandan Prithiviraj, Comparison of a three-dimensional numerical model with existing methods for prediction of flow in shell-and-tube heat exchangers, Heat Transf. Eng. 20 (1999) 15–19. doi:10.1080/014576399271538.

[41] Y. You, A. Fan, S. Huang, W. Liu, Numerical modeling and experimental validation of heat transfer and flow resistance on the shell side of a shell-and-tube heat exchanger with flower baffles, Int. J. Heat Mass Transf. 55 (2012) 7561–7569. doi:10.1016/j.ijheatmasstransfer.2012.07.058.

[42] B. Sunden, Computational Heat Transfer in Heat Exchanger Analysis and Design (Invited), (2005) 649–660. http://dx.doi.org/10.1115/DETC2005-84746.

[43] Ž. Stevanović, G. Ilić, N. Radojković, M. Vukić, V. Stefanović, G. Vučković, Design of Shell-and-Tube Heat Exchangers By Using Cfd Technique – Part One: Thermo-Hydraulic Calculation, Mech. Eng. 1 (2001) 1091–1105.

[44] E. Pal, I. Kumar, J.B. Joshi, N.K. Maheshwari, CFD simulations of shell-side flow in a shell-and-tube type heat exchanger with and without baffles, Chem. Eng. Sci. 143 (2016) 314–340. doi:10.1016/j.ces.2016.01.011.

[45] A. Bell, K., Mueller, Wolverine Heat Transfer Data Book II, 2001.

[46] F. Nemati Taher, S. Zeyninejad Movassag, K. Razmi, R. Tasouji Azar, Baffle space impact on the performance of helical baffle shell and tube heat exchangers, Appl. Therm. Eng. 44 (2012) 143–149. doi:10.1016/j.applthermaleng.2012.03.042.

[47] ANSYS Inc, ANSYS Fluent Theory Guide, 2015. doi:10.1016/0140-3664(87)90311-2.

[48] ANSYS Inc., ANSYS Fluent User's Guide, 2015.

[49] S.-E. Kim, D. Choudhury, B. Patel., Computations of complex turbulent flows using commercial code ANSYS Fluent, in: ICASE/LaRC/AFOSR Symp. Model. Complex Turbul. Flows, Hampton, Virginia, 1997.

[50] B.E. Short, Heat Transfer and Pressure in Heat Exchangers, Publication No. 4324, University of Texas, Austin, TX, 1943.

[51] W. Roetzel, P.J. Heggs, D. Butterworth, Design and Operation of Heat Exchangers, Springer Berlin Heidelberg, 2012. https://books.google.co.uk/books?id=38buCAAAQBAJ.

[52] Q. Wang, Y. Chen, B. Sundén, Emerging Topics in Heat Transfer: Enhancement and Heat Exchangers, WIT Press, 2013. https://books.google.co.uk/books?id=NNAtAgAAQBAJ.

[53] M.A. Founti, C. Vafidis, J.H. Whitelaw, Shell-side distribution and the influence of inlet conditions in a model of a disc-and-doughnut heat exchanger, Exp. Fluids. 3 (1985) 293–300.

[54] T. Kuppan, Heat exchanger design handbook, CRC, 2000.

[55] Daniel A. Donohue, Heat transfer and Pressure Drop in Heat Exchangers, Ind. Eng. Chem. 41 (1969) 2499–2511.

[56] B. Slipcevic, Designing Heat Exchangers with Disk and Ring Baffles, Sulzer Tech. Rev. 58 (1976) 114–120.

[57] B. Slipcevic, Shell-side pressure drop in shell-and-tube heat exchangers with disk and ring baffles, Sulzer Tech. Rev. 60 (1978) 28–30.

[58] K.P. Goyal, B.K. Gupta, An experimental performance evaluation of a disk and doughnut type heat exchanger, J. Heat Transfer. 106 (1984) 759–765. http://dx.doi.org/10.1115/1.3246749.

[59] H. Li, V. Kottke, Analysis of local shellside heat and mass transfer in the shell-and-tube heat exchanger with disc-and-doughnut baffles, Int. J. Heat Mass Transf. 42 (1999) 3509–3521. doi:10.1016/S0017-9310(98)00368-8.

[60] K. Thulukkanam, Heat Exchanger Design Handbook, in: Second Edi, CRC Press, 2013: pp. 323–326.

[61] H. Hausen, Warmeubertragung im Gegenstrom, Gleichstrom und Kreuzstrom, Springer Berlin Heidelberg, 2013.

[62] W.H. McAdams, Heat Transmission, 3rd ed., McGraw-Hill, New York, 1954.

[63] H. Jouhara, T.K. Nannou, L. Anguilano, H. Ghazal, N. Spencer, Heat pipe based municipal waste treatment unit for home energy recovery, Energy. (2017). doi:10.1016/j.energy.2017.02.044.

[64] C. Tecchio, J.L.G. Oliveira, K.V. Paiva, M.B.H. Mantelli, R. Gandolfi, L.G.S. Ribeiro, Thermal performance of thermosyphons in series connected by thermal plugs, Exp. Therm. Fluid Sci. 88 (2017) 409–422. doi:10.1016/j.expthermflusci.2017.06.021.

[65] H. Jouhara, A. Chauhan, T. Nannou, S. Almahmoud, B. Delpech, L.C. Wrobel, Heat pipe based systems - Advances and applications, Energy. 128 (2017) 729–754. doi:10.1016/j.energy.2017.04.028.

[66] A.G. Olabi, Renewable energy and energy storage systems, Energy. (2017). doi:10.1016/j.energy.2017.07.054.

[67] Y. Naresh, C. Balaji, Experimental investigations of heat transfer from an internally finned two phase closed thermosyphon, Appl. Therm. Eng. 112 (2017) 1658–1666. doi:10.1016/j.applthermaleng.2016.10.084.

[68] T. Wadowski, A. Akbarzadeh, P. Johnson, Characteristics of a gravity-assisted heat pipe-based heat exchanger, Heat Recover. Syst. CHP. 11 (1991) 69–77. doi:10.1016/0890-4332(91)90189-B.

[69] S.H. Noie-Baghban, G.R. Majideian, Waste heat recovery using heat pipe heat exchanger (HPHE) for surgery rooms in hospitals, Appl. Therm. Eng. 20 (2000) 1271–1282. doi:10.1016/S1359-4311(99)00092-7.

[70] H. Jouhara, A.J. Robinson, Experimental investigation of small diameter two-phase closed thermosyphons charged with water, FC-84, FC-77 and FC-3283, Appl. Therm. Eng. 30 (2010) 201–211. doi:10.1016/j.applthermaleng.2009.08.007.

[71] G. Rice, Heat Pipes, (n.d.). http://www.thermopedia.com/content/835/ (accessed April 17, 2016).

[72] G.P. Peterson, An introduction to heat pipes: Modeling, testing, and applications, John Wiley & Sons Inc., 1994. https://books.google.co.uk/books?id=-dVSAAAAMAAJ.

[73] L.L. Vasiliev, Heat pipes in modern heat exchangers, Appl. Therm. Eng. 25 (2005) 1–19. doi:10.1016/j.applthermaleng.2003.12.004.

[74] H. Ma, N. Du, Z. Zhang, F. Lyu, N. Deng, C. Li, S. Yu, Assessment of the optimum operation conditions on a heat pipe heat exchanger for waste heat

recovery in steel industry, Renew. Sustain. Energy Rev. 79 (2017) 50–60. doi:10.1016/j.rser.2017.04.122.

[75] A. Faghri, Heat pipes: review, opportunities and challenges, Front. Heat Pipes. 5 (2014). doi:10.5098/fhp.5.1.

[76] H. Ma, L. Yin, X. Shen, W. Lu, Y. Sun, Y. Zhang, N. Deng, Experimental study on heat pipe assisted heat exchanger used for industrial waste heat recovery, Appl. Energy. 169 (2016) 177–186. doi:10.1016/j.apenergy.2016.02.012.

[77] H. Jouhara, Z. Ajji, Y. Koudsi, H. Ezzuddin, N. Mousa, Experimental investigation of an inclined-condenser wickless heat pipe charged with water and an ethanol–water azeotropic mixture, Energy. 61 (2013) 139–147. doi:10.1016/j.energy.2012.09.033.

[78] H. Hagens, F.L.A. Ganzevles, C.W.M. van der Geld, M.H.M. Grooten, Air heat exchangers with long heat pipes: Experiments and predictions, Appl. Therm. Eng. 27 (2007) 2426–2434. doi:10.1016/j.applthermaleng.2007.03.004.

[79] A.R. Lukitobudi, A. Akbarzadeh, P.W. Johnson, P. Hendy, Design, construction and testing of a thermosyphon heat exchanger for medium temperature heat recovery in bakeries, Heat Recover. Syst. CHP. 15 (1995) 481–491. doi:10.1016/0890-4332(95)90057-8.

[80] H. Jouhara, H. Merchant, Experimental investigation of a thermosyphon based heat exchanger used in energy efficient air handling units, Energy. 39 (2012) 82–89. doi:10.1016/j.energy.2011.08.054.

[81] H.N. Chaudhry, B.R. Hughes, S.A. Ghani, A review of heat pipe systems for heat recovery and renewable energy applications, Renew. Sustain. Energy Rev. 16 (2012) 2249–2259. doi:10.1016/j.rser.2012.01.038.

[82] D.A. Reay, A review of gas-gas heat recovery systems, J. Heat Recover. Syst. 1 (1981) 3–41. doi:10.1016/0198-7593(81)90003-5.

[83] H. Shabgard, T.L. Bergman, N. Sharifi, A. Faghri, High temperature latent heat thermal energy storage using heat pipes, Int. J. Heat Mass Transf. 53 (2010) 2979–2988. doi:10.1016/j.ijheatmasstransfer.2010.03.035.

[84] J. Ramos, A. Chong, H. Jouhara, Experimental and numerical investigation of a cross flow air-to-water heat pipe-based heat exchanger used in waste heat recovery, Int. J. Heat Mass Transf. 102 (2016) 1267–1281. doi:10.1016/j.ijheatmasstransfer.2016.06.100.

[85] H. Mroue, J.B. Ramos, L.C. Wrobel, H. Jouhara, Experimental and numerical investigation of an air-to-water heat pipe-based heat exchanger,

Appl. Therm. Eng. 78 (2015) 339–350. doi:10.1016/j.applthermaleng.2015.01.005.

[86] A. Žukauskas, Heat transfer from tubes in crossflow, Adv. Heat Transf. 8 (1972) 93–160.

[87] P.A. Kew, K. Cornwell, Correlations for the prediction of boiling heat transfer in small-diameter channels, Appl. Therm. Eng. 17 (1997) 705–715. doi:10.1016/S1359-4311(96)00071-3.

[88] S.H. Noie, Heat transfer characteristics of a two-phase closed thermosyphon, Appl. Therm. Eng. 25 (2005) 495–506. doi:10.1016/j.applthermaleng.2004.06.019.

[89] R.I. Vachon, G.H. Nix, G.E. Tanger, Evaluation of constants for the Rohsenow pool-boiling correlation, J. Heat Transfer. 90 (1968) 239–246. http://dx.doi.org/10.1115/1.3597489.

[90] M.G. Cooper, Heat flow rates in saturated nucleate pool boiling-A wide-ranging examination using reduced properties, in: 1984: pp. 157–239. doi:10.1016/S0065-2717(08)70205-3.

[91] W.A. Khan, R.J. Culham, M.M. Yovanovich, Analytical model for convection heat transfer from tube banks, J. Thermophys. Heat Transf. 20 (2006) 720–727. doi:10.2514/1.15453.

[92] Y.A. Cengel, Heat & Mass Transfer: A Practical Approach, Third, McGraw-Hill Education (India) Pvt Limited, 2007. https://books.google.co.uk/books?id=nuQ7F81pBFAC.

[93] W.M. Rohsenow, A method of correlating heat transfer data for surface boiling of liquids, Trans. ASME. 74 (1952) 969–976.

[94] M.S. El-Genk, H.H. Saber, Heat transfer correlations for small, uniformly heated liquid pools, Int. J. Heat Mass Transf. 41 (1998) 261–274. doi:10.1016/S0017-9310(97)00143-9.

[95] U. Gross, Reflux condensation heat transfer inside a closed thermosyphon, Int. J. Heat Mass Transf. 35 (1992) 279–294. doi:10.1016/0017-9310(92)90267-V.

[96] W.M. Rohsenow, J. Hartnett, Y. Cho, Heat Transfer, 1998. doi:10.1016/0017-9310(75)90148-9.

[97] M. Shiraishi, K. Kikuchi, T. Yamanishi, Investigation of heat transfer characteristics of a two-phase closed thermosyphon, J. Heat Recover. Syst. 1 (1981) 287–297. doi:10.1016/0198-7593(81)90039-4.

[98] B. Fadhl, L.C. Wrobel, H. Jouhara, Numerical modelling of the temperature distribution in a two-phase closed thermosyphon, Appl. Therm. Eng. 60 (2013) 122–131. doi:10.1016/j.applthermaleng.2013.06.044.

[99] ANSYS Inc., ANSYS Meshing User â€™ s Guide, 2015.

[100] Lecture 6 Turbulence Modeling, Introduction to ANSYS FLUENT, ANSYS, Inc., Release 13.0, (2010). http://imechanica.org/files/fluent_13.0_lecture06-turbulence.pdf.

[101] J.-F. Yang, M. Zeng, Q.-W. Wang, Numerical investigation on combined single shell-pass shell-and-tube heat exchanger with two-layer continuous helical baffles, Int. J. Heat Mass Transf. 84 (2015) 103–113. doi:10.1016/j.ijheatmasstransfer.2014.12.042.

[102] Y.-C. Tsai, F.-B. Liu, P.-T. Shen, Investigations of the pressure drop and flow distribution in a chevron-type plate heat exchanger, Int. Commun. Heat Mass Transf. 36 (2009) 574–578. doi:10.1016/j.icheatmasstransfer.2009.03.013.

[103] Lecture 7: Turbulence Modeling ANSYS Inc 16.0 Release, (2015). https://www.scribd.com/document/302199566/Fluent-Intro-16-0-L07-Turbulence.

[104] D. Jafari, S. Filippeschi, A. Franco, P. Di Marco, Unsteady experimental and numerical analysis of a two-phase closed thermosyphon at different filling ratios, Exp. Therm. Fluid Sci. 81 (2017) 164–174. doi:10.1016/j.expthermflusci.2016.10.022.

[105] K. Negishi, T. Sawada, Heat transfer performance of an inclined two-phase closed thermosyphon, Int. J. Heat Mass Transf. 26 (1983) 1207–1213. doi:10.1016/S0017-9310(83)80175-6.

[106] T. Paramatthanuwat, S. Boothaisong, S. Rittidech, K. Booddachan, Heat transfer characteristics of a two-phase closed thermosyphon using de ionized water mixed with silver nano, Heat Mass Transf. Und Stoffuebertragung. 46 (2010) 281–285. doi:10.1007/s00231-009-0565-y.

[107] D. Reay, R. McGlen, P. Kew, Heat Pipes: Theory, Design and Applications, Elsevier Science, 2013. https://books.google.co.uk/books?id=_G2SIYmFLEAC.

[108] D.A. Reay, P.A. Kew, R.J. McGlen, Chapter 3 – Heat pipe components and materials, in: Heat Pipes, 2014: pp. 65–94. doi:10.1016/B978-0-08-098266-3.00003-0.

[109] L. Shang, D. Zhong, Z. Ji, Experimental performance of a two-phase closed thermosyphon charged with hydrocarbons and Freon refrigerants for

renewable Energy applications, in: Energy Procedia, 2017: pp. 2–7. doi:10.1016/j.egypro.2017.03.1044.

[110] D. Jafari, P. Di Marco, S. Filippeschi, A. Franco, An experimental investigation on the evaporation and condensation heat transfer of two-phase closed thermosyphons, Exp. Therm. Fluid Sci. 88 (2017) 111–123. doi:10.1016/j.expthermflusci.2017.05.019.

[111] J.M. Saiz Jabardo, E. Fockink da Silva, G. Ribatski, S.F. de Barros, Evaluation of the Rohsenow correlation through experimental pool boiling of halocarbon refrigerants on cylindrical surfaces, 26 (2004) 218–230.

[112] I. Tanasawa, N. Lior, Heat and mass transfer in materials processing, (1992).

[113] J.M. Saiz Jabardo, C.L. Silva, Modeling of the nucleate boiling of refrigerant-oil mixtures, in: 18th Int. Congr. Refrig., Montreal, Canada, 1991.

[114] I.L. Pioro, Experimental evaluation of constants for the Rohsenow pool boiling correlation, Int. J. Heat Mass Transf. 42 (1999) 2003–2013. doi:10.1016/S0017-9310(98)00294-4.

[115] Thermal conductivity of common materials and gases, (n.d.). http://www.engineeringtoolbox.com/thermal-conductivity-d_429.html (accessed July 8, 2017).

[116] F.P. Incropera, D.P. DeWitt, Introduction to Heat Transfer, 7th editio, Wiley, 2011. https://books.google.co.uk/books?id=kvawuAAACAAJ.

[117] J.R. Taylor, An introduction to error analysis: The study of uncertainties in physical measurements, Univ. Sci. Books. 1 (1997).

APPENDICES

Appendix A

```
/****************************************************************************/
/*                                                              */
/* User-Defined Functions for temperature-dependent air and water properties */
/* FLUENT 16.2                                                           */
/*                                                              */
/* Author: Hassan Mroue                                                      */
/*   Date: July 2016                                                     */
/*                                                              */
/****************************************************************************/



#include "udf.h"

/*Air Properties*/

DEFINE_PROPERTY(density_air,cell,thread)
{
real temp, rho_air;
temp = C_T(cell,thread);
rho_air = 0.16103 + 0.34473 * exp(-(temp-273.15) / 103.23714) + 0.78857 * exp(-(temp-273.15) /
512.29169);
return rho_air;
}


DEFINE_PROPERTY(viscos_air,cell,thread)
{
real temp, mu_air;
temp=C_T(cell,thread);
mu_air = 0.0000170899 + 0.000000046117 * (temp-273.15) - 2.07642E-11 *pow((temp-273.15), 2) +
5.40458E-15 * pow((temp-273.15),3);
return mu_air;
}


DEFINE_PROPERTY(cond_air,cell,thread)
{
real temp, k_air;
temp= C_T(cell,thread);
k_air= 0.02411 + 0.0000771055 * (temp-273.15) - 0.0000000281463 *pow((temp-273.15),2) +
6.36061E-12 * pow((temp-273.15),3);
return k_air;
}



/* Water Properties*/

DEFINE_PROPERTY(density_water,cell,thread)
{
real temp, rho_water;
temp=C_T(cell,thread);
rho_water =  exp(2.2467 * pow((1 - ((temp-273.15) / 647.25)),(1 / 3)) - 2.09405 * pow((1 - ((temp-
273.15) / 647.25)),(2 / 3)) + 2.737 * (1 - ((temp-273.15) / 647.25)) - 1.7475 * pow((1 - ((temp-273.15) /
647.25)), (4 / 3))) * 315.5;
return rho_water;
}
```

```
DEFINE_PROPERTY(viscos_water,cell,thread)
{
real temp, mu_water;
temp=C_T(cell,thread);
mu_water = exp(-10.1083 + 1.39621 * pow((1 / ((temp-273.15) / 647.25) - 1),(1 / 3)) + 0.48431 *
pow((1 / ((temp-273.15) / 647.25) - 1),(4 / 3)) + 0.71019 * pow((1 / ((temp-273.15) / 647.25) - 1),(7 /
3)));
return mu_water;
}
```

```
DEFINE_PROPERTY(cond_water,cell,thread)
{
		real temp, k_water;
		temp=C_T(cell,thread);
		k_water= -1.63975 + 11.1421 * (temp / 647.25) + -20.0805 * pow((temp / 647.25),2) +
16.7447 * pow((temp / 647.25),3) + -5.78763 * pow((temp / 647.25),4);
		return k_water;
}
```

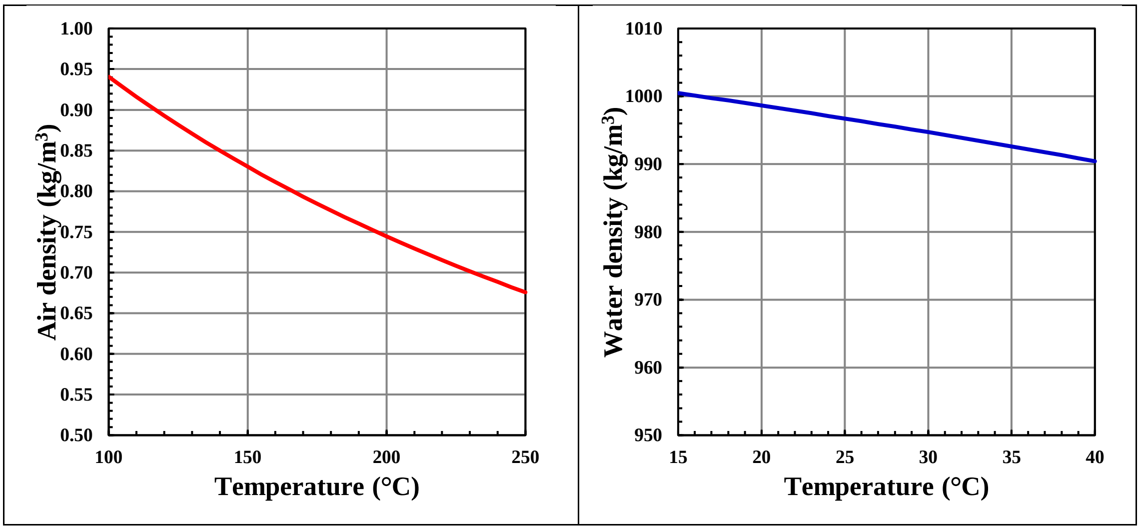

Air (left) and water (right) density-temperature relation.

Appendix B – Meshing

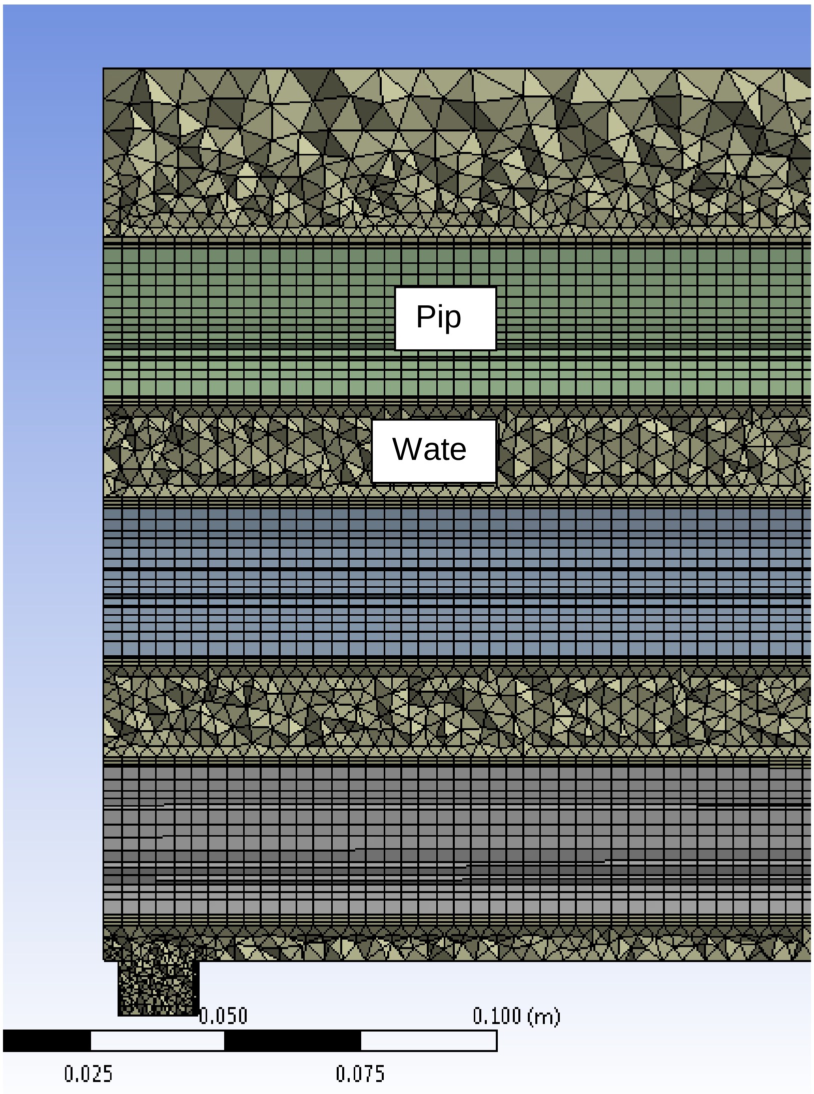

Close-up photo of the interface between the pipes outer fluid.

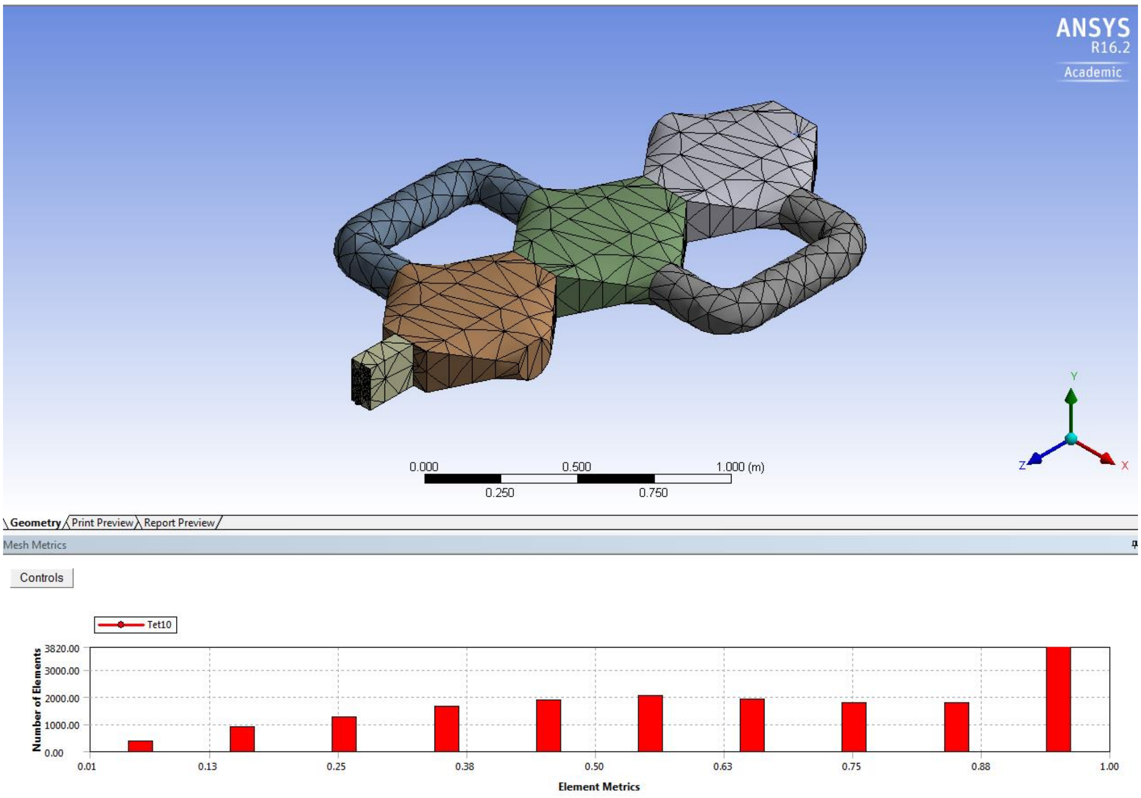

Automatic generated mesh for case 3, including the skewness.

Appendix C

Mathematical Operation	**Example**	**Associated Error**
Addition/ Subtraction	$x = a + b + c = \cdots$	$S_x = \sqrt{S_a^2 + S_b^2 + S_c^2 + \cdots}$
Multiplication/ Division	$x = a * b/c = \cdots$	$S_x = x\sqrt{\left(\frac{S_a}{a}\right)^2 + \left(\frac{S_b}{b}\right)^2 + \left(\frac{S_c}{c}\right)^2 + \cdots}$
Exponentiation	$x = a^b$	$S_x = x * b * \left(\frac{S_a}{a}\right)$
Logarithm	$10^x = \log_{10} a$ $e^x = \ln(a)$	$S_x = 0.434 \times \left(\frac{S_a}{a}\right)$ $S_x = \frac{S_a}{a}$
Antilog	$10^x = 10^a \times a$ $e^x = e^a$	$S_x = 2.303 * x * S_a$ $S_x = x * S_a$

x is the result of the calculation,

S_x is the associated with the result,

a, b and c are the individual numbers used for the calculation of the result,

S_a, S_b and S_c are the uncertainties associated with the individual numbers for the calculation of the result.

Readings and associated errors are listed below:

Variable	**Read from**	**Associated error**
T_{hot}	Dual input, high accuracy datalogger/ thermometer, Model HH506RA	**K/J/T/E Type:** $\pm(0.05\%\, rdg + 0.3°C\ on - 50\ to\ 1370°C$ $\pm(0.05\%\, rdg + 0.7°C\ on - 50\ to - 210°C$
T_{cold}	Dual input, high accuracy datalogger/	**K/J/T/E Type:** $\pm(0.05\%\, rdg + 0.3°C\ on - 50\ to\ 1370°C$

	thermometer, Model HH506RA	$\pm(0.05\%\ rdg + 0.7°C\ on - 50\ to - 210°C$
v	Liquid flow indicator, 0.07 – 0.55 l/min, Model 1859998	$\pm 2\%$ (Unspecified Scaling – Assumed Full Scale)
ρ	Tabulated value based on T_{in} and T_{out}	Ignore
c_p	Tabulated value based on T_{in} and T_{out}	Ignore
I	Meteix MX22 Multimeter	ac: $\pm 1.2\%$; dc: $\pm 1\%$ (Unspecified Scaling – Assumed Full Scale)
V	Meteix MX22 Multimeter	ac: $\pm 1.2\%$; dc: $\pm 1\%$ (Unspecified Scaling – Assumed Full Scale)

Appendix D

TABLE 11.4 Heat Exchanger NTU Relations

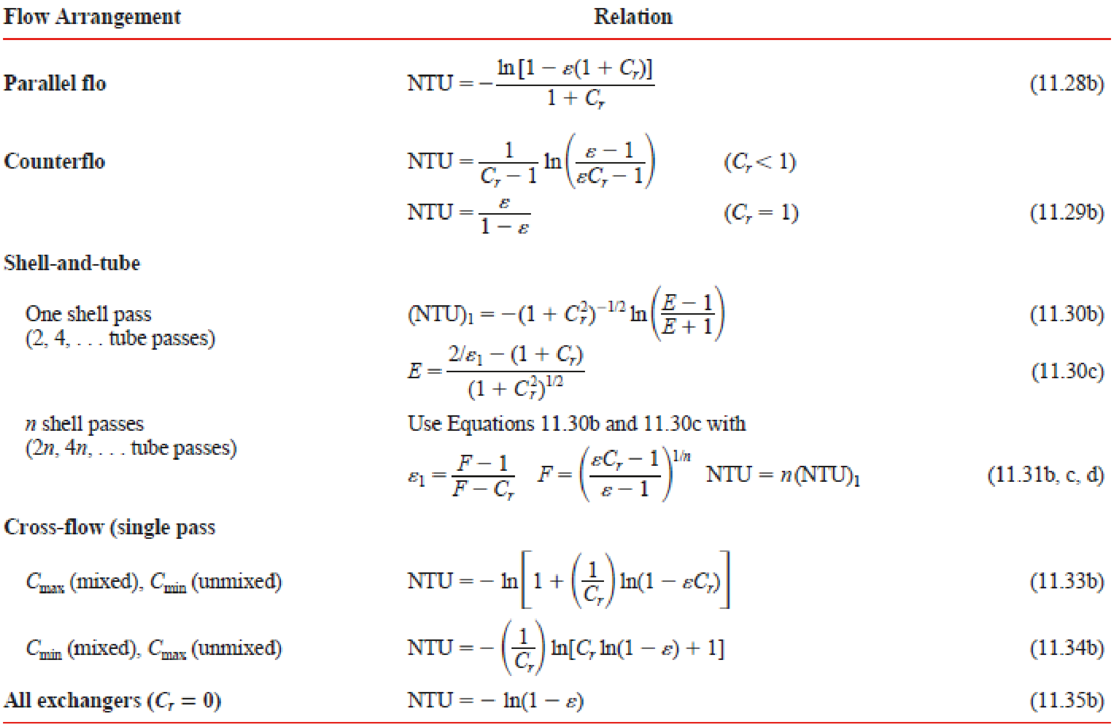

Flow Arrangement	Relation		
Parallel flo	$\mathrm{NTU} = -\dfrac{\ln[1 - \varepsilon(1 + C_r)]}{1 + C_r}$		(11.28b)
Counterflo	$\mathrm{NTU} = \dfrac{1}{C_r - 1} \ln\left(\dfrac{\varepsilon - 1}{\varepsilon C_r - 1}\right)$	$(C_r < 1)$	
	$\mathrm{NTU} = \dfrac{\varepsilon}{1 - \varepsilon}$	$(C_r = 1)$	(11.29b)
Shell-and-tube			
One shell pass (2, 4, . . . tube passes)	$(\mathrm{NTU})_1 = -(1 + C_r^2)^{-1/2} \ln\left(\dfrac{E - 1}{E + 1}\right)$		(11.30b)
	$E = \dfrac{2/\varepsilon_1 - (1 + C_r)}{(1 + C_r^2)^{1/2}}$		(11.30c)
n shell passes ($2n$, $4n$, . . . tube passes)	Use Equations 11.30b and 11.30c with $\varepsilon_1 = \dfrac{F - 1}{F - C_r} \quad F = \left(\dfrac{\varepsilon C_r - 1}{\varepsilon - 1}\right)^{1/n} \quad \mathrm{NTU} = n(\mathrm{NTU})_1$		(11.31b, c, d)
Cross-flow (single pass			
$C_{\max}$ (mixed), $C_{\min}$ (unmixed)	$\mathrm{NTU} = -\ln\left[1 + \left(\dfrac{1}{C_r}\right)\ln(1 - \varepsilon C_r)\right]$		(11.33b)
$C_{\min}$ (mixed), $C_{\max}$ (unmixed)	$\mathrm{NTU} = -\left(\dfrac{1}{C_r}\right)\ln[C_r \ln(1 - \varepsilon) + 1]$		(11.34b)
All exchangers ($C_r = 0$)	$\mathrm{NTU} = -\ln(1 - \varepsilon)$		(11.35b)

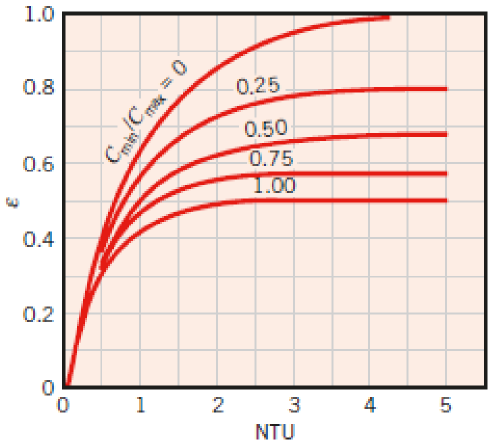

FIGURE 11.10 Effectiveness of a parallel-flow heat exchanger (Equation 11.28).

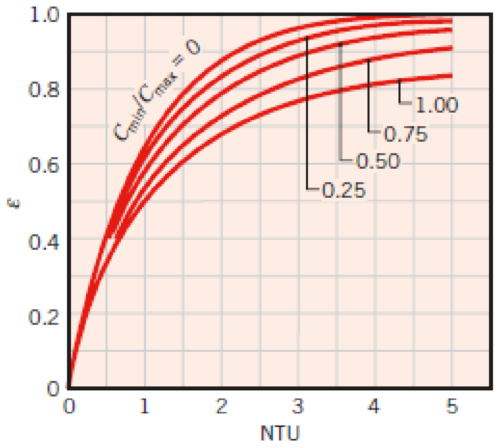

FIGURE 11.11 Effectiveness of a counterflow heat exchanger (Equation 11.29).

Appendix E

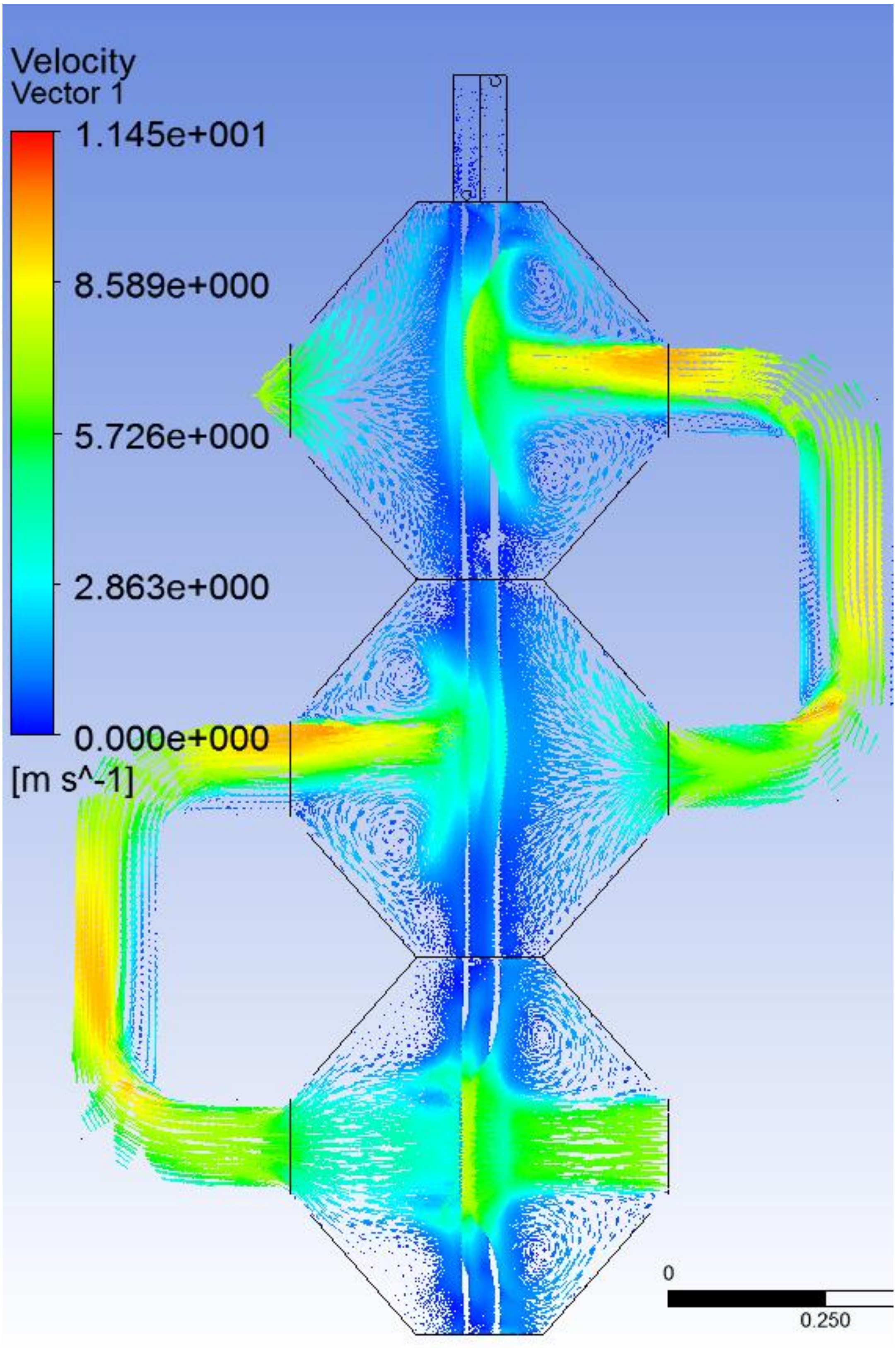

Case 3, velocity distribution at 0.14 kg/s and 150°C.